Wave Propagation in Liquid-Crystal Materials

Wellenausbreitung in Flüssigkristallmaterialien

Zur Erlangung des akademischen Grades Doktor-Ingenieur (Dr.-Ing.)
genehmigte Dissertation von M.Sc. Xiao Wang aus Rongcheng, China
Oktober 2014 — Darmstadt — D 17

TECHNISCHE
UNIVERSITÄT
DARMSTADT

Fachbereich Elektrotechnik und
Informationstechnik
Institut für Theorie
Elektromagnetischer Felder (TEMF)

Wave Propagation in Liquid-Crystal Materials
Wellenausbreitung in Flüssigkristallmaterialien

Genehmigte Dissertation von M.Sc. Xiao Wang aus Rongcheng, China

1. Gutachten: Prof. Dr.-Ing. Thomas Weiland
2. Gutachten: Prof. Dr.-Ing. Rolf Jakoby

Tag der Einreichung: 22.04.2014
Tag der Prüfung: 09.09.2014

Darmstadt — D 17

For my family

Kurzfassung

Die vorliegende Arbeit beschäftigt sich mit der numerischen Simulation von abstimmbaren Hochfrequenzbauelementen auf der Basis von Flüssigkristallen unter expliziter Berücksichtigung der zugrunde liegenden anisotropen dielektrischen Materialeigenschaften. Zur Bestimmung der vorab benötigten Ausrichtung der Flüssigkristallmoleküle in einem externen elektrostatischen Feld werden die bekannte Vektormethode sowie die modernere Q-Tensor Methode herangezogen. Die numerische Auswertung erfolgt mithilfe der Methode der Finiten Integration (FIT), die sowohl für die Berechnung der Direktorfelder als auch für die Simulation der Wellenausbreitung in Flüssigkristallen entsprechend erweitert wurde.

Flüssigkristalle wurden bereits erfolgreich als abstimmbare dielektrische Materialien zur Realisierung von steuerbaren Hochfrequenzbauelementen eingesetzt. Um solche Bauelemente auch numerisch mit hoher Genauigkeit untersuchen zu können, muss eine geeignete Modellierung gefunden werden, die neben der Ausrichtung der Kristalle in einem externen elektrischen Feld auch die gezielte Simulation der Wellenausbreitung elektromagnetischer Felder in Flüssigkristallmaterialien ermöglicht.

Die Berechnung der resultierenden Ausrichtung der Flüssigkristallmoleküle basiert auf dem Prinzip der minimalen freien Energie und muss sowohl die richtungsabhängigen Materialparameter als auch die Geometrie der eingesetzten Elektroden korrekt berücksichtigen. In Verbindung mit FIT für elektrostatische Anwendungen wurde neben der bekannten Vektordarstellung von Oseen-Frank auch die aufwändigere Q-Tensor Methode von Landau-de Gennes angewendet. Die Vektormethode hebt sich auf der einen Seite durch ihre geringe Sensitivität bezüglich der verwendeten Gitternetzdichte und dem geringen numerischen Aufwand hervor, sodass sie für die Simulation einer Vielzahl von praktischen Anwendungsfällen geeignet ist. Andererseits zeigt die Q-Tensor Methode dann ihre volle Stärke, wenn in den Flüssigkristallen vereinzelt Disklinationen oder topologische Übergänge zwischen verschiedenen Zuständen auftreten und sich diese nur mit einer biaxialen Anordnung der Moleküle beschreiben lassen. Für beide Ansätze wurden in der vorliegenden Arbeit dynamische Gleichgewichtszustände auf der Grundlage dispersiver Effekte formuliert.

Die Methode der Finiten Integration wurde um eine effektive Materialmittelung erweitert, um die Ausbreitung hochfrequenter elektromagnetischer Felder auch in solchen anisotropen dielektrischen Materialien simulieren zu können, wie sie bei-

spielsweise bei inhomogen ausgerichteten Flüssigkristallanordnungen auftreten. Für die Zeitbereichsimulationen mussten die traditionellen Aktualisierungsgleichungen deswegen leicht modifiziert werden, um die notwendigerweise verschwindenden Tangentialkomponenten der elektrischen Feldstärke auf der Grenzfläche zwischen ideal elektrisch leitfähigen Gebieten und den Flüssigkristallmaterialien unter allen Umständen einzuhalten.

Mithilfe des im Rahmen dieser Arbeit implementierten Simulationswerkzeugs wurden ein rekonfigurierbarer Wellenleiterpolarisator sowie ein abstimmbarer Phasenschieber durchgerechnet, die beide auf der Basis von Flüssigkristallmaterialien realisiert wurden. Die vorliegenden Simulationsergebnisse stimmen gut mit Messungen an Prototypaufbauten für den Polarisator überein, die am Institut für Mikrowellentechnik und Photonik durchgeführt wurden.

Abstract

In this dissertation, the numerical simulation of tunable liquid-crystal (LC) based radio-frequency (RF) devices is studied with specific emphasis on the anisotropic dielectric property of LC media. The well-known vector method as well as the more advanced Q-tensor method are both investigated in order to obtain the distribution of the LC director field orientation in static electric fields. The finite integration technique is applied with dedicated extensions to enable electrostatic field determination and high-frequency simulation based on LC media.

Liquid crystals have been successfully applied as tunable dielectrics in the realization of tunable RF components. In order to numerically investigate such devices with high accuracy, a proper modeling which involves the LC director field in a static electric field as well as the propagation of electromagnetic fields in LC media has been set up.

The determination of the resulting LC molecule orientation is based on the minimization of the total free energy and has to include the directional material parameters as well as the electrode geometry. In combination with electrostatic formulation of the finite integration technique, the Oseen-Frank vector-representation method and the Landau-de Gennes Q-tensor-representation method are both applied. On the one hand, the vector method is not sensitive to mesh density and has less computational cost so it is suitable for the simulation of a large variety of applications. On the other hand, when disclinations or topological transitions between distinct states are involved, the Q-tensor method is better suited because of its capability in describing biaxial arrangement of liquid crystal molecules. For both methods, the time dynamic equilibrium equations are formulated according to the dissipation principle.

The finite integration technique is combined with the effective dielectric method to simulate the propagation of high-frequency electromagnetic fields in anisotropic dielectric media caused by inhomogeneous orientation of liquid crystal molecules. A small alteration with respect to the traditional update scheme is necessary in order to guarantee vanishing tangential electric fields on the interface between perfect electric conductor and anisotropic material.

A reconfigurable waveguide polariser and a tunable phase shifter based on LC materials are simulated with the help of the implemented simulation tools. The simulation results are in good agreement with measurement data for the polarizer that have been obtained at the Institute of Microwave Engineering and Photonics.

Contents

1 Introduction **1**
- 1.1 Liquid Crystals . . . 1
- 1.2 Physics of Liquid Crystals . . . 2
- 1.3 Tunable Liquid-Crystal Based Radio-Frequency Devices . . . 3
- 1.4 Outline of the Thesis . . . 5

2 Finite Integration Technique **7**
- 2.1 Maxwell's Equations . . . 7
- 2.2 Maxwell's Grid Equations . . . 8
- 2.3 Electrostatic Problems . . . 13
- 2.4 High-frequency Problems . . . 13
  - 2.4.1 Space Stability . . . 13
  - 2.4.2 Update Scheme . . . 15

3 Liquid-Crystal Orientation in Static Electric Fields **17**
- 3.1 Mathematical Descriptions . . . 17
- 3.2 Electrostatic Problems . . . 18
  - 3.2.1 Formulation of Electrostatic Problems . . . 18
  - 3.2.2 Construction of Permittivity Matrix . . . 18
- 3.3 Vector Method . . . 23
  - 3.3.1 Frank Energy . . . 23
  - 3.3.2 Vector Statics . . . 25
  - 3.3.3 Vector Dynamics . . . 32
- 3.4 Q-tensor Method . . . 33
  - 3.4.1 Tensor Order Parameter . . . 33
  - 3.4.2 Landau-de Gennes Energy . . . 37
  - 3.4.3 Q-tensor Statics . . . 42
  - 3.4.4 Q-tensor Dynamics . . . 43
- 3.5 Comparisons of Vector and Q-tensor Method . . . 44
  - 3.5.1 π-cell . . . 44
  - 3.5.2 Simulation of π-cell . . . 45
  - 3.5.3 Disclinations . . . 49
  - 3.5.4 Modeling of Disclinations . . . 53

3.5.5 Conclusions 54

4 Propagation of Electromagnetic Fields in Liquid-Crystal Materials 57
4.1 Material Modeling 57
4.1.1 Effective Dielectric Method 59
4.1.2 Inverse Permittivity Matrix 63
4.2 Space Stability 67
4.2.1 Symmetry and Positive Definiteness of the Effective Permittivity 69
4.2.2 Symmetry and Positive Definiteness of the Inverse Permittivity Matrix 70
4.3 Stable Update Scheme 72
4.3.1 Drawback of the Traditional Update Scheme 72
4.3.2 Alternative Update Scheme 73
4.4 Error Analysis 75

5 Applications 79
5.1 Introduction to the Simulation Tools 79
5.2 Waveguide Polariser 80
5.2.1 Model Description 82
5.2.2 Simulation Results and Discussion 84
5.3 Phase Shifter 91
5.3.1 Model Description 91
5.3.2 Simulation Results and Discussion 92

6 Summary and Outlook 97

Acronyms and Symbols 101

1 Introduction

1.1 Liquid Crystals

Liquid crystals are an intermediate material between crystalline solid and isotropic liquids [1]. In this state, they may flow like a liquid, but its molecules retain orientational order of crystalline solid [2]. LC can be broadly classified as thermotropic, lyotropic and metallotropic [3]. Thermotropic and lyotropic LC are composed of organic molecules, while metallotropic LC are formed from both organic and inorganic molecules. Phase transition of thermotropic LC can be induced by changes of temperature [4]. For lyotropics LC, besides temperature, the solvent concentration could also cause phase transition [5]. Due to the constituent, phase transition of metallotropic LC depends not only on temperature and the solvent concentration, but also on the composition ratio of organic and inorganic molecules [3].

Typically, the molecules of thermotropic LC are rod-like (calamitic) or disk-like (discotic), and their size is usually several nanometers [6]. The phase transitions of calamitic LC have been illustrated in Fig. 1.1. The molecules are in isotropic phase when the temperature is high enough. In this phase, the molecules have neither positional nor orientational order. The material can flow like a liquid and the molecules are randomly headed.

If the temperature is decreased, the molecules will experience nematic phase where the molecules have orientational order but no positional order. The molecules can still move around. But the long axis of them tend to align with one another. Though the heading of molecules will whirl with time and differ between molecules, the time average of them has preferred direction and so does the spatial average of them at the macroscopic scale.

When the temperature falls further, the material may transform into smectic phase where the molecules have a degree of positional order besides the orientational order. This smectic order results in layered structure. In these layers, the molecules are ordered along one direction. Two typical smectic phases are smectic-A phase, in which the orientations of molecules are perpendicular to the layer, and smectic-C phase, where the molecules are oriented in an angle with the layer normal [7].

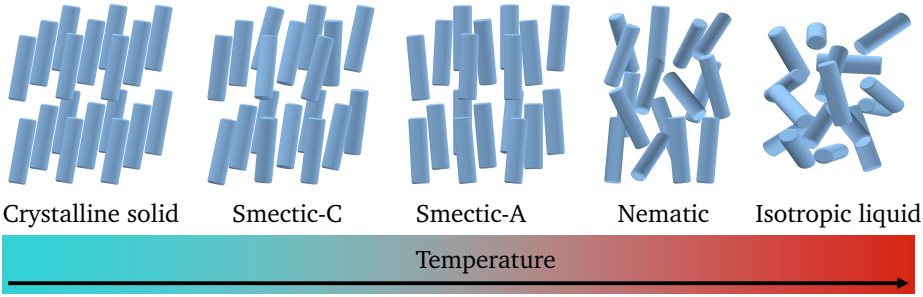

Figure 1.1: Phases of calamitic liquid crystals

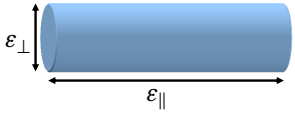

Figure 1.2: Schematic diagram of a rod-like molecule with the anisotropic dielectric axes

At low temperature, the molecules have both orientational and positional order therefore the material is in crystalline solid phase. The translational viscosity is infinitely strong and the molecules can hardly move.

Among those phases, the nematic phase is commercially used in liquid-crystal display, and it also shows a promising future in high-frequency devices. Thus, its physics properties will be discussed in more detail.

1.2 Physics of Liquid Crystals

Due to the rod-like molecules, calamitic LC show anisotropic dielectric properties. As illustrated in Fig. 1.2, $\varepsilon_\parallel$ denotes the permittivity of the long axis, while $\varepsilon_\perp$ denotes the permittivity of the direction perpendicular to the long axis. When a static electric field is applied, the induced dipole moments will result in the orientation of molecules along the direction of the electric field.

In most liquid-crystal devices, the LC container is coated with some alignment layers which constrain the orientation of molecules. A simple way to form homogeneous anchoring would be mechanically rubbing the surface of the substrate

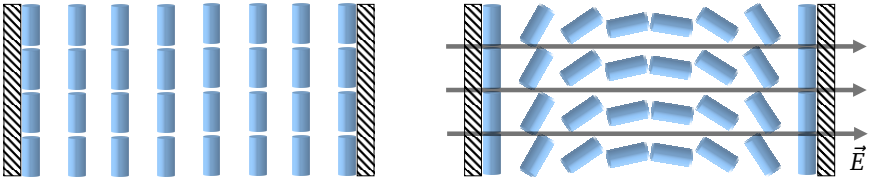

Figure 1.3: Schematic diagram of liquid crystals with strong homogeneous anchoring: (a) electric field off (b) electric field on

which contains the LC with a cotton ball or cloth [6]. The micro-grooves on the substrate will force the molecules to align along the same direction. In this way, the alignment layer has only a weak anchoring strength of about 10^{-5} J/m^2. The more common way in achieving homogeneous anchoring is to rub it with polyimides which has a high anchoring strength of about 10^{-3} J/m^2. The way to obtain homeotropic anchoring is using monolayer surfactants.

In Fig. 1.3 the case with homogeneous alignment layer is demonstrated. The molecules have the same direction with the alignment direction in the absence of electric field. When the electric field is available, the molecules inside the container can be oriented by this electric field, whereas the molecules on the surface will still be constrained by the alignment layer.

1.3 Tunable Liquid-Crystal Based Radio-Frequency Devices

The requirement for tunable or reconfigurable devices for RF applications has increased in the recent years [8]. For example, microwave devices such as tunable varactors, filters for mobile communications, and millimeter-wave devices like phase shifters for radar sensing [9] [10]. As tunable dielectrics, LC show promising performances in the realizations of these tunable RF components [11] [12] [13] [14] [15].

In order to investigate LC-based RF components, numerical simulations are used because they allow for cheaper and faster design or optimization than experiment. Furthermore, numerical simulations can provide additional information, such as the information about the spatial orientation of LC which is difficult to achieve in experiments.

In general, the simulation of LC-based RF components can be divided into two steps. The first step is to achieve the director field of LC in a static electric field.

The second step is to perform the high-frequency wave propagation simulation in LC media.

There are different ways in obtaining the director field of LC. One possible way is given by the molecular simulation which considers the interaction between LC molecules in the molecular scale [16] [17]. Yet the LC-based RF components usually have the size from micrometers to millimeters. Therefore, it will be memory and time consuming to apply molecular simulation. Indeed, the mesoscopic approaches where the orientation of LC can be considered as a spatial continuous field would be the appropriate choice. Two continuum theories that are mainly applied are the Oseen-Frank theory [18] [19] [20] and the Landau-de Gennes theory [1]. In the Oseen-Frank theory, the orientation of LC is represented in terms of a vector field. This scheme works well in disclination-free geometries. But in the presence of disclinations, which might be caused by large electric fields, specific combinations of alignment layers, etc., this scheme will fail because it can't handle the biaxial arrangement around the disclination core [21]. For such cases, the Q-tensor method based on the Landau-de Gennes theory is required. By considering variation in the orientational order parameter and biaxiality arrangement of molecules, this method is capable to model the disclinations.

Given the director field of LC, high-frequency electromagnetic wave propagation can be simulated to characterize the electrical properties of LC-based RF components, such as scattering parameters (S-parameters). There are several discretization techniques like the finite element method (FEM), the finite volume method (FVM), the finite difference in time domain (FDTD) and the finite integration technique (FIT), etc. available to perform field simulations. Among these techniques, the FIT is chosen here and has been extended to enable the simulation of tensor dielectric materials based on LC.

The FIT, presented by Weiland in 1977 [22], is a powerful scheme which can numerically solve electromagnetic problems in general. It performs the discretization of the continuous Maxwell's equations one by one to formulate the discrete Maxwell's grid equations without approximation. Important topological properties, like curl-free of gradient and divergence-free of curl, and principles of the continuous case, like the conservation of energy and charges, are both guaranteed in the discrete form. This scheme allows different formulations for the discrete problems, such as electrostatic problems and high-frequency problems, which have to be considered to properly simulate LC-based RF components.

Because of these attractive features of FIT, it is possible to extend its applicability to the time-domain simulation of tensor dielectric media in order to perform high-frequency electromagnetic simulation of LC materials.

1.4 Outline of the Thesis

After introducing the properties of LC and the motivation for the numerical simulation of tunable LC-based RF devices, Chapter 2 gives a brief introduction to FIT. The basic formulations of Maxwell's grid equations for electrostatic problems and high-frequency problems are introduced, respectively, since they are both involved in the numerical simulation of tunable LC-based RF devices.

The modeling of tunable LC-based RF devices is discussed in Chapter 3 and Chapter 4. In Chapter 3, it is introduced how to achieve LC director fields in static electric fields. The vector method based on the Oseen-Frank theory and the Q-tensor method based on the Landau-de Gennes theory are presented. Fundamental differences can be observed based on the modeling of a π-cell* and disclinations. The advantages and disadvantages of both methods are discussed according to the demonstrated comparisons.

Chapter 4 focuses on the time-domain simulation of tensor dielectric material since LC can be thought to be a continuously varying tensor dielectric material after being oriented by a static electric field. It will detail the construction of the inverse permittivity matrix and prove the symmetry and positive definiteness of this matrix which is necessary to guarantee the space stability. Afterwards, the drawback of the traditional update scheme is described and a modification is provided to solve this problem. Furthermore, an error analysis based on numerical simulation of a cavity is established.

The numerical simulation of a reconfigurable waveguide polariser and a tunable phase shifter as realistic applications is demonstrated in Chapter 5. The S-parameters are obtained for both components while the simulation results of the polariser are compared with measurements.

The work is concluded with a summary and an outlook in Chapter 6.

* The π-cell is a kind of LC geometry with a parallel alignment of substrates.

2 Finite Integration Technique

The finite integration technique (FIT) is used as a spatial discretization method for the numerical simulation of tunable LC-based RF components. Therefore, it will be presented in detail in this chapter. Maxwell's grid equations can be deduced from the integral form of Maxwell's equations if the fundamental relations are applied to finite-sized grid elements. They are formulated without approximations and can be used in order to solve electrostatic and high-frequency problems, respectively.

2.1 Maxwell's Equations

Maxwell's equations represent the fundamental equations to describe macroscopic electromagnetic phenomena in continuous space. They are shown below in integral form

$$\int_{\partial A} \vec{E}(\vec{r},t)\cdot \mathrm{d}\vec{s} = -\iint_{A} \frac{\partial}{\partial t}\vec{B}(\vec{r},t)\cdot \mathrm{d}\vec{A}, \tag{2.1}$$

$$\int_{\partial A} \vec{H}(\vec{r},t)\cdot \mathrm{d}\vec{s} = \iint_{A} \left(\frac{\partial}{\partial t}\vec{D}(\vec{r},t)+\vec{J}(\vec{r},t)\right)\cdot \mathrm{d}\vec{A}, \tag{2.2}$$

$$\iint_{\partial V} \vec{B}(\vec{r},t)\cdot \mathrm{d}\vec{A} = 0, \tag{2.3}$$

$$\iint_{\partial V} \vec{D}(\vec{r},t)\cdot \mathrm{d}\vec{A} = \iiint_{V} \rho(\vec{r},t)\mathrm{d}V \tag{2.4}$$

for any area A, volume V and their respective boundaries ∂A and ∂V. The vectors $\vec{E}$, $\vec{D}$ are the electric field strength and the electric flux density, the vectors $\vec{H}$, $\vec{B}$ refer to the magnetic field strength and the magnetic flux density while the symbols $\vec{J}$, ρ denote the electric current density and the electric charge density. The symbols $\vec{r}$ and t affiliated to them are the spatial variable and temporal variable, respectively. Equation (2.1) and equation (2.2) are called Faraday's law and Ampère's law, respectively. The third equation (2.3) states the sum of the magnetic flux through any closed, regular surface is zero and the fourth equation (2.4) is known as Gauss's law. The current density $\vec{J}$ in the equation (2.2) contains the current density $\vec{J}_q$ caused by the motion of free charges, the conduction current density

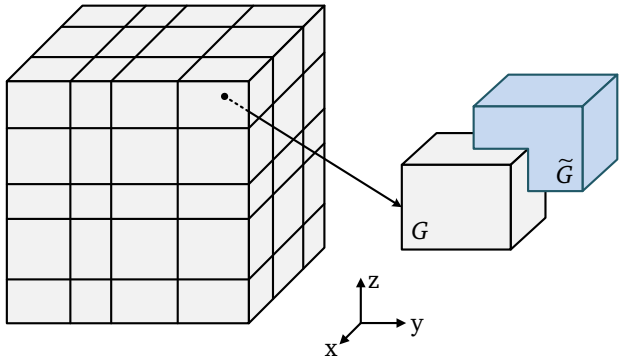

Figure 2.1: Example of a primary grid cell G and a dual grid cell $\widetilde{G}$ in Cartesian coordinates

$\vec{J}_\kappa$ which arises from the existing electric field strength in an electric conductor and the imposed current density $\vec{J}_i$ which expresses the excitation of the problem

$$\vec{J}(\vec{r},t) = \vec{J}_q(\vec{r},t) + \vec{J}_\kappa(\vec{r},t) + \vec{J}_i(\vec{r},t). \tag{2.5}$$

The material properties are described by two additional constitutive equations which relate the electric and magnetic field strengths $\vec{E}$, $\vec{H}$ to the electric and magnetic flux densities $\vec{D}$, $\vec{B}$. In the case of linear and non-dispersive materials, the constitutive equations can be written as

$$\vec{D}(\vec{r},t) = \boldsymbol{\varepsilon}(\vec{r})\vec{E}(\vec{r},t), \tag{2.6}$$

$$\vec{B}(\vec{r},t) = \boldsymbol{\mu}(\vec{r})\vec{H}(\vec{r},t). \tag{2.7}$$

Here, the symbols $\boldsymbol{\varepsilon}(\vec{r})$ and $\boldsymbol{\mu}(\vec{r})$ denote the permittivity and permeability tensors of the material, respectively. For isotropic materials, they reduce to scalars $\varepsilon(\vec{r})$, $\mu(\vec{r})$.

2.2 Maxwell's Grid Equations

In order to solve Maxwell's equations on a numerical basis, the three-dimensional computational domain $\Omega \in \mathbf{R}^3$, which contains the space of interest, is decomposed into a finite number of volume cells such as hexahedra or tetrahedra. In this disser-

tation, a three-dimensional Cartesian coordinate grid system denoted as primary grid G is applied (see Fig. 2.1). According to the FIT principles, the dual grid $\widetilde{G}$ is introduced by taking the centers of the grid cell G as grid nodes of $\widetilde{G}$.

In this grid system, the electric field strength $\vec{E}$ and magnetic flux density $\vec{B}$ are related to electric edge voltages $\widehat{e}_\upsilon(i,j,k)$ and magnetic facet fluxes $\widehat{\widehat{b}}_\upsilon(i,j,k)$ in the primary grid G. The electric flux density $\vec{D}$ and magnetic field strength $\vec{H}$ are transformed to electric facet fluxes $\widehat{\widehat{d}}_\upsilon(i,j,k)$ and magnetic edge voltages $\widehat{h}_\upsilon(i,j,k)$ in the dual grid $\widetilde{G}$:

$$\widehat{e}_\upsilon(i,j,k) = \int_{L_\upsilon(i,j,k)} \vec{E}\cdot \mathrm{d}\vec{s}, \tag{2.8}$$

$$\widehat{\widehat{b}}_\upsilon(i,j,k) = \int_{A_\upsilon(i,j,k)} \vec{B}\cdot \mathrm{d}\vec{A}, \tag{2.9}$$

$$\widehat{h}_\upsilon(i,j,k) = \int_{\widetilde{L}_\upsilon(i,j,k)} \vec{H}\cdot \mathrm{d}\vec{s}, \tag{2.10}$$

$$\widehat{\widehat{d}}_\upsilon(i,j,k) = \int_{\widetilde{A}_\upsilon(i,j,k)} \vec{D}\cdot \mathrm{d}\vec{A}, \tag{2.11}$$

where υ denotes the axis x, y or z. The geometrical entities $L_\upsilon(i,j,k)$, $\widetilde{L}_\upsilon(i,j,k)$, $A_\upsilon(i,j,k)$ and $\widetilde{A}_\upsilon(i,j,k)$ are the edges and facets of the primary grid G and dual grid $\widetilde{G}$, respectively.

Applying the Maxwell's equation (2.1) to the grid facet $A_x(i,j,k)$ in Fig. 2.2 and using the integrals (2.8) and (2.9), it can be seen that

$$\widehat{e}_y(i,j,k) + \widehat{e}_z\left(i,j+1,k\right) - \widehat{e}_y\left(i,j,k+1\right) - \widehat{e}_z(i,j,k) = -\frac{\mathrm{d}}{\mathrm{d}t}\widehat{\widehat{b}}_x(i,j,k), \tag{2.12}$$

where all the four electric edge voltages (e.g. $\widehat{e}_y(i,j,k)$) are allocated at the four edges of the grid facet $A_x(i,j,k)$, and $\widehat{\widehat{b}}_x(i,j,k)$ represents the magnetic flux through the facet $A_x(i,j,k)$.

Repeating the same procedure for all the electric edge voltages and magnetic facet fluxes in the primary grid G, the discrete form of the Maxwell's equation (2.1) can be achieved

$$\mathbf{C}\widehat{\mathbf{e}} = -\frac{\mathrm{d}}{\mathrm{d}t}\widehat{\widehat{\mathbf{b}}}, \tag{2.13}$$

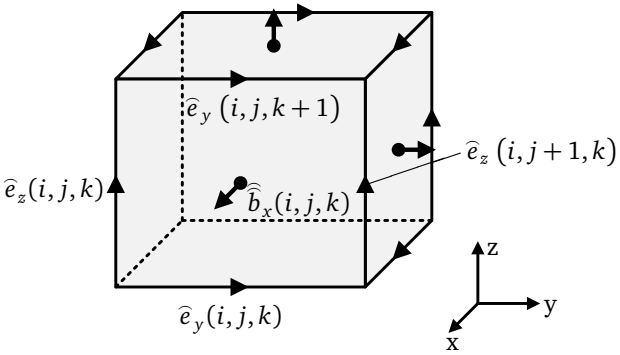

Figure 2.2: A grid cell G in Cartesian coordinates with the allocation of the electric voltages on the edges of the front facet of the grid cell and the magnetic flux through this facet

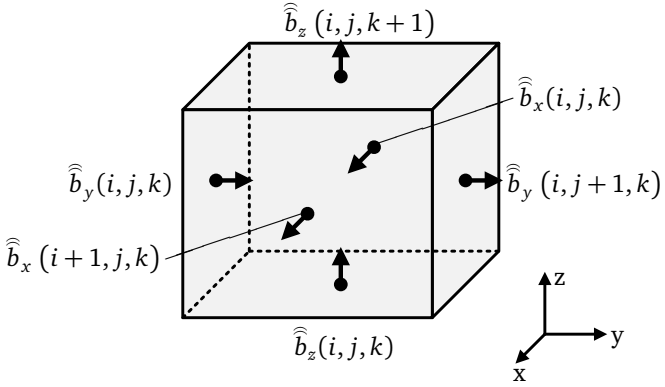

Figure 2.3: A grid cell G in Cartesian coordinates with the allocation of the magnetic facet fluxes on the facets of this grid cell

where $\widehat{\mathbf{e}}$ and $\widehat{\widehat{\mathbf{b}}}$ are the vectors of all the edge voltages and facet fluxes, respectively. The matrix $\mathbf{C}$ is the discrete curl operator of the primary grid G which selects the corresponding components out of vector to compose the individual equation such as (2.12). Thus, the set of all the elements in $\mathbf{C}$ is $\{-1,0,1\}$.

Another fundamental relation can be derived by applying the Maxwell's equation (2.3) to the volume $V(i,j,k)$ of primary grid G in Fig. 2.3. By adding up the six relevant fluxes, the closed surface integral can be obtained

$$\begin{aligned}\widehat{\widehat{b}}_x\left(i+1,j,k\right)+\widehat{\widehat{b}}_y\left(i,j+1,k\right)+\widehat{\widehat{b}}_z\left(i,j,k+1\right)\\ -\widehat{\widehat{b}}_x(i,j,k)-\widehat{\widehat{b}}_y(i,j,k)-\widehat{\widehat{b}}_z(i,j,k)=0.\end{aligned} \tag{2.14}$$

Applying this principle to the entire primary grid G, another discrete equation can be obtained as

$$\mathbf{S}\widehat{\widehat{\mathbf{b}}}=0, \tag{2.15}$$

where $\mathbf{S}$ is the divergence operator of the primary grid G.

Since the components of magnetic voltage and the electric flux are allocated at the edges and facets of the dual grid $\widetilde{G}$, the remaining Maxwell's equations which contains the curl operation of the magnetic field strength and the divergence operation of the electric flux density are discretized on the dual grid $\widetilde{G}$. After a similar deduction, the discrete forms of the remaining two Maxwell's equations can be derived. Thus, the complete set of discrete forms of Maxwell's equation for the grid pair $\{G,\widetilde{G}\}$, the so-called Maxwell's grid equations (MGE), are given by

$$\mathbf{C}\widehat{\mathbf{e}}=-\frac{\mathrm{d}}{\mathrm{d}t}\widehat{\widehat{\mathbf{b}}}, \tag{2.16}$$

$$\widetilde{\mathbf{C}}\widehat{\mathbf{h}}=\frac{\mathrm{d}}{\mathrm{d}t}\widehat{\widehat{\mathbf{d}}}+\widehat{\widehat{\mathbf{j}}}, \tag{2.17}$$

$$\mathbf{S}\widehat{\widehat{\mathbf{b}}}=0, \tag{2.18}$$

$$\widetilde{\mathbf{S}}\widehat{\widehat{\mathbf{d}}}=\mathbf{q}. \tag{2.19}$$

The matrices $\widetilde{\mathbf{C}}$ and $\widetilde{\mathbf{S}}$ are the dual discrete curl operator and dual discrete divergence operator, respectively, $\widehat{\widehat{\mathbf{j}}}$ is the vector of the integrated current densities through a dual facet, and $\mathbf{q}$ is the vector of charges inside a dual gird cell.

When dealing with electrostatics and magnetostatics problems, the electric field strength and magnetic field strength are usually represented as gradient-fields

based on scalar potentials. Within the context of FIT, the discrete forms of these relations are

$$\widehat{\mathbf{e}} = -\mathbf{G}\boldsymbol{\phi}, \tag{2.20}$$

$$\widehat{\mathbf{h}} = -\widetilde{\mathbf{G}}\boldsymbol{\psi}. \tag{2.21}$$

Here, the vectors $\boldsymbol{\phi}$ and $\boldsymbol{\psi}$ are composed of electric and magnetic scalar nodal potentials, respectively, the matrices $\mathbf{G}$ and $\widetilde{\mathbf{G}}$ are the discrete grad operators of primary grid and dual grid.

Due to the topological symmetry, the discrete grad operator $\mathbf{G}$ and $\widetilde{\mathbf{G}}$ are strongly connected to the discrete divergence operators $\mathbf{S}$ and $\widetilde{\mathbf{S}}$

$$\mathbf{G} = -\widetilde{\mathbf{S}}^T, \tag{2.22}$$

$$\widetilde{\mathbf{G}} = -\mathbf{S}^T. \tag{2.23}$$

Similarly, the primary grid curl operator $\mathbf{C}$ is related to the dual grid curl operator $\widetilde{\mathbf{C}}$ by [23]

$$\widetilde{\mathbf{C}} = \mathbf{C}^T. \tag{2.24}$$

Furthermore, an important feature of the discrete operators is that they retain fundamental properties of continuous space [23] [24] [25]

$$\nabla \cdot \nabla \times \vec{A} \equiv 0 \longleftrightarrow \mathbf{SC} = 0, \widetilde{\mathbf{S}}\widetilde{\mathbf{C}} = 0, \tag{2.25}$$

$$\nabla \times \nabla a \equiv 0 \longleftrightarrow \mathbf{CG} = 0, \widetilde{\mathbf{C}}\widetilde{\mathbf{G}} = 0. \tag{2.26}$$

So far, a disretization has been performed for Maxwell's equations and an exact representation of Maxwell's equations on the grid pair $\{G, \widetilde{G}\}$ has been derived. Yet, there has been no discussion of the material properties. In order to take into account the material properties, the discrete forms of the constitutive equations are derived

$$\widehat{\widetilde{\mathbf{d}}} = \mathbf{M}_\varepsilon \widehat{\mathbf{e}}, \tag{2.27}$$

$$\widehat{\widetilde{\mathbf{b}}} = \mathbf{M}_\mu \widehat{\mathbf{h}}, \tag{2.28}$$

$$\widehat{\widetilde{\mathbf{j}}} = \mathbf{M}_\kappa \widehat{\mathbf{e}} + \widehat{\widetilde{\mathbf{j}}}_i, \tag{2.29}$$

with the permittivity matrix $\mathbf{M}_\varepsilon$, the permeability matrix $\mathbf{M}_\mu$ and the conductivity matrix $\mathbf{M}_\kappa$. In this notation, $\widehat{\widetilde{\mathbf{j}}}_i$ is the vector of imposed currents.

2.3 Electrostatic Problems

When the MGE is applied to electrostatic problems, all the time derivatives vanish. Therefore, the equations related with electric edge voltages or electric facet fluxes can be rewritten as

$$\mathbf{C}\widehat{\mathbf{e}} = 0, \tag{2.30}$$

$$\widetilde{\mathbf{S}}\widehat{\widehat{\mathbf{d}}} = \mathbf{q}. \tag{2.31}$$

Equation (2.30) can be satisfied automatically by choosing an electric scalar nodal potential vector $\boldsymbol{\phi}$ according to equation (2.20). Substituting equation (2.20) and (2.27) into equation (2.31) will result in

$$-\widetilde{\mathbf{S}}\mathbf{M}_{\varepsilon}\mathbf{G}\boldsymbol{\phi} = \mathbf{q}, \tag{2.32}$$

which is actually the discrete form of Poisson's Equation.

2.4 High-frequency Problems

In order to deal with high-frequency problems, equation (2.27) and (2.28) are substituted into (2.16) and (2.17). Consequently, it can be obtained that

$$\mathbf{C}\widehat{\mathbf{e}} = -\frac{\mathrm{d}}{\mathrm{d}t}\mathbf{M}_{\mu}\widehat{\mathbf{h}}, \tag{2.33}$$

$$\widetilde{\mathbf{C}}\widehat{\mathbf{h}} = \frac{\mathrm{d}}{\mathrm{d}t}\mathbf{M}_{\varepsilon}\widehat{\mathbf{e}} + \widehat{\widehat{\mathbf{j}}} \tag{2.34}$$

2.4.1 Space Stability

For the situation without conductive materials and missing external current excitation, the integrated current densities $\widehat{\widehat{\mathbf{j}}}$ in equation (2.34) vanish. Combining equation (2.34) and (2.33), it leads to

$$\mathbf{M}_{\varepsilon}^{-1}\widetilde{\mathbf{C}}\mathbf{M}_{\mu}^{-1}\mathbf{C}\widehat{\mathbf{e}} = -\frac{\mathrm{d}^2}{\mathrm{d}t^2}\widehat{\mathbf{e}}. \tag{2.35}$$

Transformation to the frequency domain results in

$$\begin{aligned}\mathbf{M}_{\varepsilon}^{-1}\widetilde{\mathbf{C}}\mathbf{M}_{\mu}^{-1}\mathbf{C}\widehat{\mathbf{e}} &= -(j\omega)^2\widehat{\mathbf{e}} \\ &= \omega^2\widehat{\mathbf{e}}. \end{aligned} \tag{2.36}$$

This equation yields that all eigenvalues ω_i^2 are the eigenvalues of the system matrix $\mathbf{M}_{\varepsilon}^{-1}\widetilde{\mathbf{C}}\mathbf{M}_{\mu}^{-1}\mathbf{C}\widehat{\mathbf{e}}$. If this matrix has complex or negative eigenvalues, some frequencies ω_i will be complex, which results in growing oscillations, therefore leads to instability [26]. So the system matrix $\mathbf{M}_{\varepsilon}^{-1}\widetilde{\mathbf{C}}\mathbf{M}_{\mu}^{-1}\mathbf{C}\widehat{\mathbf{e}}$ must have only real and non-negative eigenvalues in order to guarantee the so-called space stability of the time-continuous formulation of the Maxwell's equations [27]. Additionally, temporal discretization can also lead to instability, and it will be discussed in the next section.

Assumed that the material matrices $\mathbf{M}_{\varepsilon}^{-1}$ and $\mathbf{M}_{\mu}^{-1}$ are both symmetric and positive definite (SPD), the matrices can be decomposed as follows:

$$\mathbf{M}_{\varepsilon}^{-1} = \mathbf{M}_{\varepsilon}^{-1/2}\mathbf{M}_{\varepsilon}^{-1/2}, \tag{2.37}$$

$$\mathbf{M}_{\mu}^{-1} = \mathbf{M}_{\mu}^{-1/2}\mathbf{M}_{\mu}^{-1/2}. \tag{2.38}$$

According to equation (2.24), (2.37) and (2.38), the system matrix of equation (2.35) can then be transformed into [27]

$$\mathbf{M}_{\varepsilon}^{-1}\widetilde{\mathbf{C}}\mathbf{M}_{\mu}^{-1}\mathbf{C} = \mathbf{M}_{\varepsilon}^{-1/2}(\mathbf{M}_{\mu}^{-1/2}\mathbf{C}\mathbf{M}_{\varepsilon}^{-1/2})^T(\mathbf{M}_{\mu}^{-1/2}\mathbf{C}\mathbf{M}_{\varepsilon}^{-1/2})\mathbf{M}_{\varepsilon}^{1/2}. \tag{2.39}$$

Since the term $(\mathbf{M}_{\mu}^{-1/2}\mathbf{C}\mathbf{M}_{\varepsilon}^{-1/2})^T(\mathbf{M}_{\mu}^{-1/2}\mathbf{C}\mathbf{M}_{\varepsilon}^{-1/2})$ is SPD, the system matrix has only real and non-negative eigenvalues. That means that equation (2.33) and (2.34) can be guaranteed to have space stability if the material matrices $\mathbf{M}_{\varepsilon}^{-1}$ and $\mathbf{M}_{\mu}^{-1}$ are SPD.

The LC materials studied in this dissertation are considered to be isotropic in permeability but full-tensor anisotropic in permittivity. Their material matrix $\mathbf{M}_{\mu}^{-1}$ is a diagonal matrix which can be proved to be SPD, while their material matrix $\mathbf{M}_{\varepsilon}^{-1}$ is usually a non-diagonal matrix due to their tensor dielectric property. Therefore, it will be discussed in Chapter 4 how to construct a material matrix $\mathbf{M}_{\varepsilon}^{-1}$ which can be guaranteed to be SPD.

2.4.2 Update Scheme

After the discussion of the space stability, the next step is to perform the time discretization of equation (2.33) and (2.34). An explicit time-stepping algorithm called leapfrog scheme is used here and it leads to

$$\widehat{\mathbf{h}}^{(m+1)} = \widehat{\mathbf{h}}^{(m)} - \Delta t \mathbf{M}_{\mu}^{-1} \mathbf{C} \widehat{\mathbf{e}}^{(m+1/2)}, \tag{2.40}$$

$$\widehat{\mathbf{e}}^{(m+3/2)} = \widehat{\mathbf{e}}^{(m+1/2)} + \Delta t \mathbf{M}_{\varepsilon}^{-1} (\widetilde{\mathbf{C}\mathbf{h}}^{(m+1)} - \widehat{\widehat{\mathbf{j}}}^{(m+1)}). \tag{2.41}$$

The electric and magnetic fields are sampled on a staggered time axis. They are evaluated in each timestep according to their values in the previous step. This update scheme works well in isotropic or diagonal anisotropic materials. When applied to tensor anisotropic materials such as LC, it will need a small modification which will be detailed in Chapter 4.

As an explicit algorithm, the leapfrog scheme is efficient but requires a properly chosen timestep to enable stability. Therefore, a condition in timestep is necessary to guarantee the stability in time. For inhomogeneous materials or non-equidistant mesh, the generalized Courant-criterion is stated [28]

$$\Delta t \leqslant \Delta t_{\max} = \frac{2}{\max\limits_{\forall i} \left| \omega_i \right|}, \tag{2.42}$$

where ω_i are the square root of the eigenvalues of the system matrix (2.39).

3 Liquid-Crystal Orientation in Static Electric Fields

This chapter focuses on the numerical simulation of LC director field orientation in static electric fields, where the mathematical descriptions will be discussed firstly. Since an electrostatic problem is involved in achieving the LC director field orientation, it will be detailed about the construction of permittivity matrix in dealing with this problem by the use of FIT. Based on the Oseen-Frank theory and the Landau-de Gennes theory, respectively, the vector method and the Q-tensor method will be introduced for the numerical simulation of LC orientation. Then, the advantages and disadvantages of these two methods will be discussed by comparisons of several test examples.

3.1 Mathematical Descriptions

The mathematical descriptions of achieving LC director field orientation are based on the free energy which contains the elastic energy, surface energy, electric interaction energy and thermotropic energy which is only available in the Q-tensor method:

$$E_{\text{free}} = E_{\text{elastic}} + E_{\text{surface}} + E_{\text{electric}} \underbrace{+E_{\text{thermotropic}}}_{\text{only available in the Q-tesnor method}} . \tag{3.1}$$

All the energy terms are functions of the orientation vector $\vec{n}$ or the tensor $\mathbf{Q}$ depending on the applied method. Additionally, the electric interaction energy is also a function of the electric scalar potential ϕ.

In the following, we use E_{sum} to represent the summation of the elastic energy, surface energy and thermotropic energy which is only available in the Q-tensor method, and χ to denote all the elements in the representation of the vector $\vec{n}$ or the tensor $\mathbf{Q}$. Take the vector $\vec{n}$ for example, the symbol χ represents the polar angle and the azimuthal angle in the spherical coordinate vector description, or its three scalar components in the Cartesian coordinate vector description. Then, the free energy in the vector or the Q-tensor representation can be rewritten as

$$E_{\text{free}}(\chi, \phi) = E_{\text{sum}}(\chi) + E_{\text{electric}}(\chi, \phi). \tag{3.2}$$

The LC director field orientation can be determined mathematically when the following conditions are fulfilled:

$$\begin{aligned} &E_{\text{free}}(\chi) = E_{\text{sum}}(\chi) + E_{\text{electric}}(\chi) \to \min, \\ &E_{\text{free}}(\phi) \to \max \Leftrightarrow E_{\text{electric}}(\phi) \to \max. \end{aligned} \tag{3.3}$$

The minimization and maximization problems included here can be solved by transforming them into differential equations as shown below

$$\begin{aligned} &\frac{\partial}{\partial \chi} E_{\text{free}}(\chi) = \frac{\partial}{\partial \chi} \left(E_{\text{sum}}(\chi) + E_{\text{electric}}(\chi) \right) = 0, \\ &\frac{\partial}{\partial \phi} E_{\text{free}}(\phi) = \frac{\partial}{\partial \phi} E_{\text{electric}}(\phi) = 0. \end{aligned} \tag{3.4}$$

There are generally two numerical ways to calculate χ and ϕ. The direct way is to solve the two equations simultaneously. An alternative way would be to solve the two equations individually and perform a global iteration till finally both χ and ϕ converge. Both variants are used in this dissertation and will be discussed in the following sections.

3.2 Electrostatic Problems

3.2.1 Formulation of Electrostatic Problems

Denoting $\boldsymbol{\varepsilon}$ the tensor permittivity of LC, the electric interaction energy density can be written as

$$f_{\text{electric}} = -\frac{1}{2} \boldsymbol{\varepsilon} \vec{E} \cdot \vec{E} = -\frac{1}{2} \boldsymbol{\varepsilon} \nabla \phi \cdot \nabla \phi. \tag{3.5}$$

Substituting this into the second equation of (3.4) and applying the Euler-Lagrange principle, we obtain

$$\nabla (\boldsymbol{\varepsilon} \nabla \phi) = 0. \tag{3.6}$$

Its discrete form is shown in equation (2.32) with the assignment $\mathbf{q} = 0$.

3.2.2 Construction of Permittivity Matrix

The discrete operators in equation (2.32) have already been discussed in the last chapter. Thus, the construction of the permittivity matrix will be introduced in this

section. In order to transfer the material properties from the continuous space to the discrete variant, it is necessary to apply several approximations. We start with the approximation of the material distribution. Each cell in the primary grid G is considered to be filled homogeneously except the cells in the LC region where a special treatment is applied. Since it is common for the electric field to induce spatial varying orientation to LC, it would be more reasonable to sample the orientation of LC at each point of primary grid G. Though it is generally possible to allocate the orientations of LC to the points of dual grid $\widetilde{G}$, we suggest the former way because of its convenience to calculate the surface energy or to apply boundary conditions. In this way, the spatial distribution of tensor permittivity in LC is discretized to the corresponding values on each grid point of LC region.

There are different methods applied in constructing the permittivity matrix for anisotropic inhomogeneous media. For example, the derivations in [29] [30] [31] are based on Taylor's series expansions. They introduce a transition layer to assist the deduction and finally obtain the permittivity matrix by reducing the thickness of the transition layer to zero. There are several cases of anisotropic inhomogeneous media discussed in these references, but the LC configurations are not covered in their discussions. Yet the authors in [32] deduce the inverse permittivity matrix by the use of FEM. Because this way is more general, it is also used in the following work.

The deduction starts with the constitutive equation

$$\vec{D} = \boldsymbol{\varepsilon}\vec{E}. \tag{3.7}$$

The fields $\vec{D}$ and $\vec{E}$ in the constitutive equation can be expressed as Whitney edge elements [32]

$$\vec{E} = \sum_j e_j \vec{w}_{ej}, \tag{3.8}$$

$$\vec{D} = \sum_j d_j \vec{w}_{ej}. \tag{3.9}$$

Substitute (3.8) and (3.9) into (3.7) and multiply it by one of the edge functions $\vec{w}_{ei}$. After integration on the spatial domain, the fundamental relation

$$\sum_j d_j \int_V \vec{w}_{ei} \cdot \vec{w}_{ej} \mathrm{d}V = \sum_j e_j \int_V \boldsymbol{\varepsilon}\vec{w}_{ei} \cdot \vec{w}_{ej} \mathrm{d}V \tag{3.10}$$

can be obtained.

Notice that the tensor elements in $\boldsymbol{\varepsilon}$ are represented with Whitney nodal elements in the region of LC:

$$\boldsymbol{\varepsilon} = \sum_{j \in LC} \boldsymbol{\varepsilon}_j w_{pj} = \sum_{j \in LC} \begin{bmatrix} (\varepsilon_{xx})_j w_{pj} & (\varepsilon_{xy})_j w_{pj} & (\varepsilon_{xz})_j w_{pj} \\ (\varepsilon_{xy})_j w_{pj} & (\varepsilon_{yy})_j w_{pj} & (\varepsilon_{yz})_j w_{pj} \\ (\varepsilon_{xz})_j w_{pj} & (\varepsilon_{yz})_j w_{pj} & (\varepsilon_{zz})_j w_{pj} \end{bmatrix} \tag{3.11}$$

and Whitney volume elements in the rest of computational domain which is occupied by isotropic material:

$$\boldsymbol{\varepsilon} = \sum_{j \notin LC} \boldsymbol{\varepsilon}_j V_j w_{vj} = \sum_{j \notin LC} \begin{bmatrix} \varepsilon_j V_j w_{vj} & 0 & 0 \\ 0 & \varepsilon_j V_j w_{vj} & 0 \\ 0 & 0 & \varepsilon_j V_j w_{vj} \end{bmatrix}, \tag{3.12}$$

where V_j is the volume of the cell filled with the material ε_j. Thus, $\boldsymbol{\varepsilon}$ can be formulated as the summation of

$$\boldsymbol{\varepsilon} = \sum_{j \in LC} \boldsymbol{\varepsilon}_j w_{pj} + \sum_{j \notin LC} \boldsymbol{\varepsilon}_j V_j w_{vj}. \tag{3.13}$$

Collecting all the values of e_j and d_j in the vectors $\widehat{\mathbf{e}}$ and $\mathbf{d}_{\mathrm{FEM}}$, respectively, and constructing two matrices $\mathbf{M}_e$ and $\mathbf{T}_\varepsilon$ with the element in i^{th} row and j^{th} column defined as below

$$\left(\mathbf{M}_e\right)_{ij} = \int_V \vec{w}_{ei} \cdot \vec{w}_{ej} \mathrm{d}V, \tag{3.14}$$

$$\left(\mathbf{T}_\varepsilon\right)_{ij} = \int_V \boldsymbol{\varepsilon} \vec{w}_{ei} \cdot \vec{w}_{ej} \mathrm{d}V, \tag{3.15}$$

equation (3.10) can be rewritten as

$$\mathbf{M}_e \mathbf{d}_{\mathrm{FEM}} = \mathbf{T}_\varepsilon \widehat{\mathbf{e}} \tag{3.16}$$

Since the electric flux density $\vec{D}$ is defined with the help of edge elements in these deductions, the vector $\mathbf{d}_{\mathrm{FEM}}$ in equation (3.16) can be related to the electric facet fluxes $\widehat{\widehat{\mathbf{d}}}$ by

$$\mathbf{d}_{\mathrm{FEM}} = \mathbf{M}_L \widehat{\widehat{\mathbf{d}}}, \tag{3.17}$$

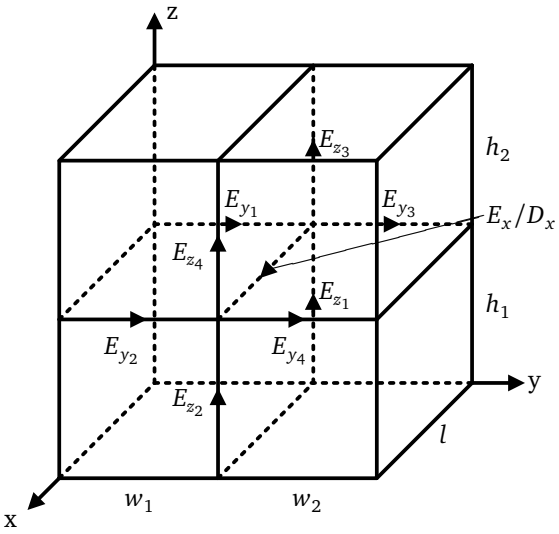

Figure 3.1: Field components in a 4-cell system

where $\left(\mathbf{M}_L\right)_{ij} = \delta_{ij}\mathbf{L}(i)/\widetilde{\mathbf{A}}(i)$. In this expression, vector $\mathbf{L}$ and $\widetilde{\mathbf{A}}$ are allocated with the lengths of edges in primary grid G and the areas of facets in dual grid $\widetilde{G}$, respectively. Substituting equation (3.17) into equation (3.16) results in

$$\widehat{\widetilde{\mathbf{d}}} = \mathbf{M}_L^{-1}\mathbf{M}_e^{-1}\mathbf{T}_\varepsilon\widehat{\mathbf{e}} = \mathbf{M}_\varepsilon\widehat{\mathbf{e}}. \tag{3.18}$$

By applying trapezoidal integration [33], $\mathbf{M}_e$ is simplified to a diagonal matrix which is easy to invert, while $\mathbf{T}_\varepsilon$ stays as a non-diagonal matrix due to anisotropic permittivity of LC. Then, the permittivity matrix can be obtained according to equation (3.18).

In order to demonstrate the performance of this method, several examples will be examined. All given examples are based on the representative 4-cell system shown in Fig. 3.1, which is a section of the whole computational domain. In this figure, the electric field strength $\vec{E}$ and the electric flux density $\vec{D}$ are discretized to field components associated with edges of the primary grid G. For convenience of the expression, the relations between the field components of $\vec{E}$ and $\vec{D}$ will be revealed rather than those between $\widehat{\mathbf{e}}$ and $\widehat{\widetilde{\mathbf{d}}}$.

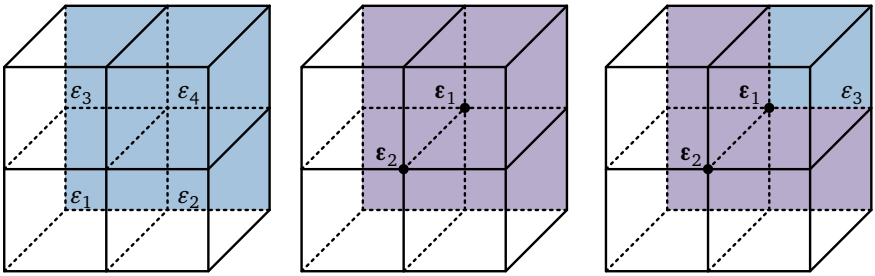

Figure 3.2: Material assignment in the representative 4-cell system. (a) Isotropic case where all cells are filled with isotropic material. (b) Anisotropic case where all cells are assigned to LC. (c) Interface case with three cells filled with LC and one cell filled with isotropic material

Isotropic Case

The first example is given by isotropic case. All cells are assigned to materials with different permittivities as shown in Fig. 3.2(a). It can be deduced from equation (3.18) that

$$D_x = \frac{w_1 h_1 \varepsilon_1 + w_2 h_1 \varepsilon_2 + w_1 h_2 \varepsilon_3 + w_2 h_2 \varepsilon_4}{(w_1 + w_2)(h_1 + h_2)} E_x \tag{3.19}$$

Anisotropic Case

In this case, all cells are located in the region of LC which are modeled with continuously varying tensor permittivities. Assumed that the tensor permittivity of the two points marked in Fig. 3.2(b) are $\boldsymbol{\varepsilon}_1$ and $\boldsymbol{\varepsilon}_2$, respectively, it can be derived that

$$\begin{aligned} D_x = & \frac{1}{2}\frac{w_1}{w_1 + w_2}(\varepsilon_{xy_1} E_{y_1} + \varepsilon_{xy_2} E_{y_2}) + \frac{1}{2}\frac{w_2}{w_1 + w_2}(\varepsilon_{xy_1} E_{y_3} + \varepsilon_{xy_2} E_{y_4}) \\ & + \frac{1}{2}\frac{h_1}{h_1 + h_2}(\varepsilon_{xz_1} E_{z_1} + \varepsilon_{xz_2} E_{z_2}) + \frac{1}{2}\frac{h_2}{h_1 + h_2}(\varepsilon_{xz_1} E_{z_3} + \varepsilon_{xz_2} E_{z_4}) \\ & + \frac{\varepsilon_{xx_1} + \varepsilon_{xx_2}}{2} E_x \end{aligned} \tag{3.20}$$

according to equation (3.18).

Interface Case

The case shown in Fig. 3.2(c) represents an interface with three cells filled with LC while one is occupied by the isotropic material ε_3. Applying equation (3.18) to this case, it leads to

$$\begin{aligned} D_x =& \frac{1}{2}\frac{w_1}{w_1+w_2}(\varepsilon_{xy_1}E_{y_1}+\varepsilon_{xy_2}E_{y_2})+\frac{1}{2}\frac{w_2h_1}{(w_1+w_2)(h_1+h_2)}(\varepsilon_{xy_1}E_{y_3}+\varepsilon_{xy_2}E_{y_4}) \\ &+\frac{1}{2}\frac{h_1}{h_1+h_2}(\varepsilon_{xz_1}E_{z_1}+\varepsilon_{xz_2}E_{z_2})+\frac{1}{2}\frac{w_1h_2}{(w_1+w_2)(h_1+h_2)}(\varepsilon_{xz_1}E_{z_3}+\varepsilon_{xz_2}E_{z_4}) \\ &+\frac{(\varepsilon_{xx_1}+\varepsilon_{xx_1})(w_1h_1+w_1h_2+w_2h_1)+2\varepsilon_3w_2h_2}{2(w_1+w_2)(h_1+h_2)}E_x \end{aligned} \tag{3.21}$$

All three cases are typical and might happen in any electrostatic simulation of LC. Yet this method is not restricted to these cases. It can be applied to more general cases in which the tangential components of electric field are guaranteed to be continuous at the boundary of each cell. It can also be used in the deduction of the inverse permittivity matrix which will be shown in the next chapter.

3.3 Vector Method

3.3.1 Frank Energy

In the vector method, the orientation of LC is represented by the descriptive vector $\vec{n}$. Thus, the elastic energy density can be expressed as [18] [20]

$$\begin{aligned} f_{\text{elastic}} =& \frac{1}{2}K_{11}(\nabla\cdot\vec{n})^2+\frac{1}{2}K_{22}\left[\vec{n}\cdot(\nabla\times\vec{n})+q_0\right]^2+\frac{1}{2}K_{33}\left|\vec{n}\times(\nabla\times\vec{n})\right|^2 \\ &+\frac{1}{2}(K_{22}+K_{24})\left[\operatorname{tr}(\nabla\vec{n})^2-(\nabla\cdot\vec{n})^2\right], \end{aligned} \tag{3.22}$$

which is also known as the Oseen-Frank energy. In this equation, the coefficients K_{11}, K_{22} and K_{33} are called Frank elastic constants which represent the fundamental splay, twist and bend distortions of LC. Their visualizations are depicted in Fig. 3.3. The coefficient K_{24} refers to saddle-splay which can be transformed into boundary conditions [34]. Therefore, it can be omitted in the case of strong anchoring. The chiral parameter q_0 is zero for ordinary nematic LC.

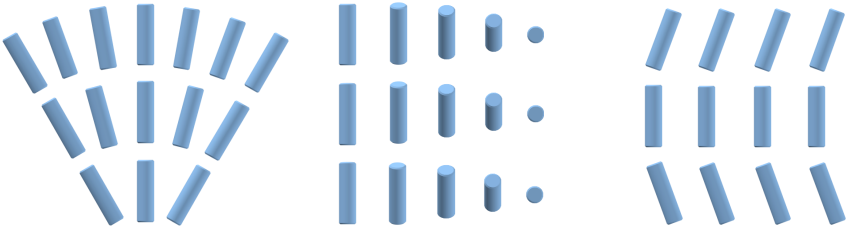

Figure 3.3: The three possible distortions of LC directors: (a) splay distortion, (b) twist distortion, (c) bend distortion

Neglecting K_{24}, q_0 and rearranging equation (3.22) results in [35]

$$f_{\text{elastic}} = \frac{1}{2}\left(K_{11} - K_{22}\right)\left(\nabla \cdot \vec{n}\right)^2 + \frac{1}{2}K_{22}\left\{\left[\vec{n} \cdot \left(\nabla \times \vec{n}\right)\right]^2 + \text{tr}\left(\nabla \vec{n}\right)^2\right\} + \frac{1}{2}K_{33}\left|\vec{n} \times \left(\nabla \times \vec{n}\right)\right|^2. \tag{3.23}$$

In order to simplify this equation, several identities will be introduced. It is known that

$$\text{tr}\left(\nabla \vec{n}\right)^2 = \text{tr}\left[\left(\nabla \vec{n}\right)^T \left(\nabla \vec{n}\right)\right] - \left|\nabla \times \vec{n}\right|^2. \tag{3.24}$$

Because $\vec{n}$ represents a unit vector with $\vec{n} \cdot \vec{n} = 1$, two additional identities can further be deduced

$$\vec{n} \times \left(\nabla \times \vec{n}\right) = -\left(\vec{n} \cdot \nabla\right)\vec{n}, \tag{3.25}$$

$$\left[\vec{n} \cdot \left(\nabla \times \vec{n}\right)\right]^2 = \left|\nabla \times \vec{n}\right|^2 - \left|\vec{n} \times \left(\nabla \times \vec{n}\right)\right|^2. \tag{3.26}$$

According to equation (3.24), (3.25) and (3.26), equation (3.23) can be simplified to [35]

$$f_{\text{elastic}} = \frac{1}{2}\left(K_{11} - K_{22}\right)\left(\nabla \cdot \vec{n}\right)^2 + \frac{1}{2}K_{22}\text{tr}\left[\left(\nabla \vec{n}\right)^T \left(\nabla \vec{n}\right)\right] + \frac{1}{2}\left(K_{33} - K_{22}\right)\left|\left(\vec{n} \cdot \nabla\right)\vec{n}\right|^2. \tag{3.27}$$

The second term of the free energy in equation (3.1) represents the surface energy. In the case of strong anchoring, the Dirichlet conditions

$$\vec{n} = \vec{n}_s \tag{3.28}$$

are applied on the respective boundaries of LC.

The electric energy which is given by the last term in equation (3.1) has already been discussed in the previous paragraphs. Additionally, the permittivity tensor $\boldsymbol{\varepsilon}$ can be defined as

$$\boldsymbol{\varepsilon} = \varepsilon_\perp \mathbf{I} + (\varepsilon_\parallel - \varepsilon_\perp)\vec{n} \otimes \vec{n}, \tag{3.29}$$

where $\mathbf{I}$ is identity matrix. Thus, the vector representation of the electric interaction energy density can be obtained by substituting it into equation (3.5):

$$f_{\text{electric}} = -\frac{1}{2}\left[\varepsilon_\perp \mathbf{I} + (\varepsilon_\parallel - \varepsilon_\perp)\vec{n} \otimes \vec{n}\right] \nabla\phi \cdot \nabla\phi. \tag{3.30}$$

Finally, all terms to specify the free energy are expressed in vector representation.

3.3.2 Vector Statics

In some LC devices, whenever the electric field is altered in time, the LC molecules are given enough time to relax to equilibrium state. Since the time evolution is not important in these devices, the simulation can be considered to be a static problem while the solution can be found by solving equation (3.4) numerically.

There are mainly two ways to represent the director vector $\vec{n}$. The first way is θ-φ approach which uses the polar angle θ and the azimuthal angle φ to describe the unit vector $\vec{n}$. Unfortunately, this approach has a shortcoming that φ could be any value when θ is close to zero [36]. So the Cartesian coordinate vector description $\vec{n} = (n_x, n_y, n_z)$ with constraint $\vec{n} \cdot \vec{n} = 1$ is chosen as the description of $\vec{n}$. A new term

$$f_{\text{constraint}} = \lambda(\vec{n} \cdot \vec{n} - 1) = \lambda(n_x^2 + n_y^2 + n_z^2 - 1) \tag{3.31}$$

is added to the free energy density to guarantee the unit length of $\vec{n}$, where λ is a Lagrange multiplier [37].

By the use of the Cartesian coordinate vector description, the elastic energy density (3.27) and the electric interaction energy (3.30) can be expanded to

$$f_{\text{elastic}} = \sum_{i,j=1,2,3} \left[\frac{1}{2} \left(K_{11} - K_{22} \right) \frac{\partial n_i}{\partial x_i} \frac{\partial n_j}{\partial x_j} + \frac{1}{2} K_{22} \left(\frac{\partial n_i}{\partial x_j} \right)^2 \right] + \sum_{i,j,k=1,2,3} \frac{1}{2} \left(K_{33} - K_{22} \right) n_i n_j \frac{\partial n_k}{\partial x_i} \frac{\partial n_k}{\partial x_j}, \tag{3.32}$$

$$f_{\text{electric}} = -\frac{1}{2} \sum_{i=1,2,3} \varepsilon_\perp \left(\frac{\partial \phi}{\partial x_i} \right)^2 - \frac{1}{2} \sum_{i,j=1,2,3} (\varepsilon_\parallel - \varepsilon_\perp) n_i n_j \frac{\partial \phi}{\partial x_i} \frac{\partial \phi}{\partial x_j}. \tag{3.33}$$

In these equations, the symbols n_1, n_2, n_3, x_1, x_2 and x_3 denote n_x, n_y, n_z, x, y and z, respectively.

The free energy can then be achieved by a volume integration using the sum of expression (3.31), (3.32) and (3.33). Due to the new variable λ introduced by the constraint term, equations (3.4) can be rewritten to

$$\frac{\partial E_{\text{free}}(n_\upsilon)}{\partial n_\upsilon} = 0, \frac{\partial E_{\text{free}}(\lambda)}{\partial \lambda} = 0, \frac{\partial E_{\text{free}}(\phi)}{\partial \phi} = 0, \tag{3.34}$$

where n_υ denotes n_x, n_y or n_z.

The usual way to discretize these equations is as follows: Firstly, apply Euler-Lagrange principle [38] to (3.34) in order to obtain a formulation which contains the variables n_υ, λ and ϕ, as well as the spatial derivatives of them. Secondly, discretize the derivatives by the use of finite difference method (FDM). This way works well for simple cases, but for some special cases, it would be difficult to define the derivatives by FDM.

To demonstrate the difficulties, we take a two-dimensional 4-cell system according to Fig. 3.4 for example. It would be easy to achieve

$$\frac{\partial^2 n_x}{\partial x^2} = 2 \frac{l_2 (n_{x_4} - n_{x_5}) + l_1 (n_{x_6} - n_{x_5})}{l_1 l_2 (l_1 + l_2)} \tag{3.35}$$

for the simple case shown in Fig. 3.4(a), in which all the cells are filled with LC. But for the special case shown in Fig. 3.4(b), where one of the cells is not occupied by LC, equation (3.35) will no longer fit, and it will be troublesome to find the proper formulation of $\partial^2 n_x / \partial x^2$ by FDM.

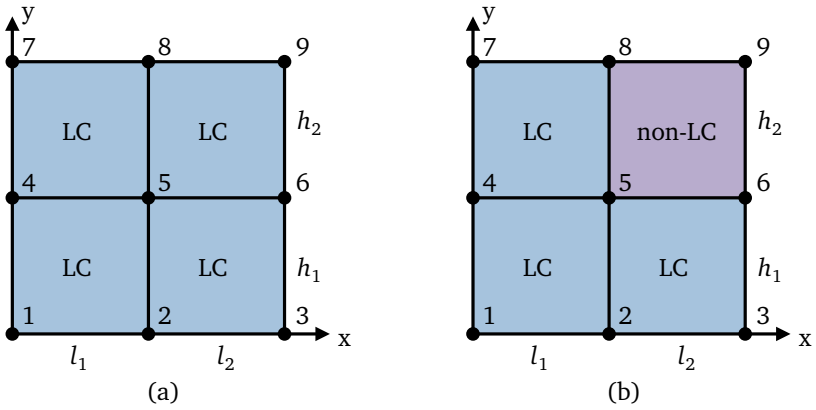

Figure 3.4: A 4-cell system in two dimensional, (a) simple case with all the cells occupied by LC, (b) special case with 3 cells of LC and 1 cell filled with non-LC material

There is also another shortcoming while applying FDM directly. Since this method discretizes the derivatives directly, the objective function is actually abandoned in the numerical calculation. It should be noticed that these derivatives are linear equations of potential ϕ, but nonlinear equations of vector $\vec{n}$. To solve nonlinear equations numerically, usually it would be more efficient when provided with the objective function.

In order to overcome these shortcomings, the simplified FEM scheme depicted in the previous paragraphs is used again. In this scheme, the director $\vec{n}$ as well as the electric potential ϕ and the Lagrange multiplier λ can be expanded by Whitney nodal elements

$$\vec{n} = \sum_{j \in LC} \vec{n}_j w_{pj} = \sum_{j \in LC} [(n_x)_j \vec{e}_x + (n_y)_j \vec{e}_y + (n_z)_j \vec{e}_z] w_{pj}, \tag{3.36}$$

$$\phi = \sum_j \phi_j w_{pj}, \tag{3.37}$$

$$\lambda = \sum_{j \in LC} \lambda_j w_{pj}. \tag{3.38}$$

Substituting these expressions into the free energy term and applying trapezoidal integration, it will lead to a function with variables $(n_x)_j$, $(n_y)_j$, $(n_z)_j$, ϕ_j and λ_j.

By arranging all the values of $(n_x)_j$, $(n_y)_j$, $(n_z)_j$ in the vector $\mathbf{n}$ and allocating all the values of ϕ_j and λ_j in the vector $\boldsymbol{\phi}$ and $\boldsymbol{\lambda}$, respectively, the free energy can be formulated in terms of a matrix function using $\mathbf{n}$, $\boldsymbol{\phi}$ and $\boldsymbol{\lambda}$. The derivatives and the Hessian matrix of this matrix function with respect to $\mathbf{n}$, $\boldsymbol{\phi}$ and $\boldsymbol{\lambda}$ can be obtained with the help of matrix calculus [39].

On the boundary S_D where the LC molecules are strongly confined by the alignment surface, Dirichlet boundary conditions must be enforced explicitly:

$$n_x = (n_x)_s, n_y = (n_y)_s, n_z = (n_z)_s \text{ on } S_D \tag{3.39}$$

On the boundary S_N without alignment layer, zero Neumann boundary conditions are applied, which are represented implicitly in the simplified FEM formulation. Since the LC devices investigated in this dissertation are considered to be finite in the computational domain, open boundary conditions will not be discussed here.

In order to depict the idea how to obtain the matrix form for the objective function, derivatives and Hessian matrix, we concentrate on the elastic energy part which is given by $(\nabla \cdot \vec{n})^2$. For the sake of simplicity, only two-dimensional domain will be considered in this example. Therefore, it can be formulated to

$$\int_V (\nabla \cdot \vec{n})^2 \, \mathrm{d}V = \int_V \left(\frac{\partial n_x}{\partial x} + \frac{\partial n_y}{\partial y} \right)^2 \mathrm{d}V. \tag{3.40}$$

Substituting (3.36) into this expression leads to

$$\int_V (\nabla \cdot \vec{n})^2 \, \mathrm{d}V = \int_V \left[\sum_j \left(n_{xj} \frac{\partial w_{pj}}{\partial x} + n_{yj} \frac{\partial w_{pj}}{\partial y} \right) \right]^2 \mathrm{d}V. \tag{3.41}$$

Independent on the coordinate system, the integration over the whole computational domain can be formulated as the summation of integration over each fundamental cell. In case of the applied Cartesian coordinate system, the trapezoidal integration rule is applied, so that the integration of any rectangular cell is equivalent to the average of the values in the four vertices multiplied by the area. Supposed that the computational domain is discretized with a mesh of m×n nodes, the rectangular cell denoted by nodes P(i, j), P(i+1, j), P(i, j+1) and P(i+1, j+1)

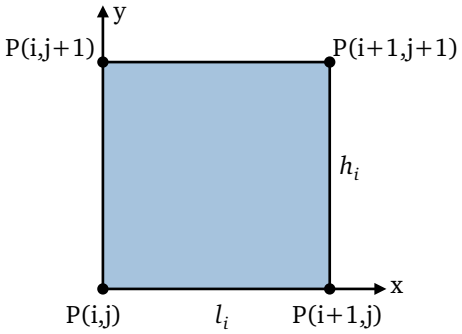

Figure 3.5: Schematic diagram of a rectangular cell with point allocations

is visualized for example in Fig. 3.5. For this representative rectangular cell, the trapezoidal integration over $(\nabla \cdot \vec{n})^2$ can be simplified to

$$\begin{aligned}
&\frac{l_i h_j}{4}\left\{\left[\frac{n_x(i+1,j)-n_x(i,j)}{l_i}+\frac{n_y(i,j+1)-n_y(i,j)}{h_j}\right]^2\right.\\
&+\left[\frac{n_x(i+1,j)-n_x(i,j)}{l_i}+\frac{n_y(i+1,j+1)-n_y(i+1,j)}{h_j}\right]^2\\
&+\left[\frac{n_x(i+1,j+1)-n_x(i,j+1)}{l_i}+\frac{n_y(i,j+1)-n_y(i,j)}{h_j}\right]^2\\
&\left.+\left[\frac{n_x(i+1,j+1)-n_x(i,j+1)}{l_i}+\frac{n_y(i+1,j+1)-n_y(i+1,j)}{h_j}\right]^2\right\}. \qquad (3.42)
\end{aligned}$$

Applying the same procedure to the remaining cells of the computational domain results in the discrete form of $\int_V (\nabla \cdot n)^2 \, \mathrm{d}V$ as a function of n_x and n_y which are allocated at each grid point. By defining the following matrices:

$$\mathbf{l} = [\underbrace{l_1, l_2, ..., l_{m-1}, 0}_{1^{\text{st}},\text{m elements}}, \underbrace{l_1, l_2, ..., l_{m-1}, 0}_{2^{\text{nd}},\text{m elements}}, ..., \underbrace{l_1, l_2, ..., l_{m-1}, 0}_{(n-1)^{\text{th}},\text{m elements}}, \underbrace{0, 0, ..., 0}_{n^{\text{th}},\text{m elements}}]^T, \qquad (3.43)$$

$$\mathbf{h} = [\underbrace{h_1, h_1, ..., h_1, 0}_{1^{\text{st}},\text{m elements}}, \underbrace{h_2, h_2, ..., h_2, 0}_{2^{\text{nd}},\text{m elements}}, ..., \underbrace{h_{n-1}, h_{n-1}, ..., h_{n-1}, 0}_{(n-1)^{\text{th}},\text{m elements}}, \underbrace{0, 0, ..., 0}_{n^{\text{th}},\text{m elements}}]^T, \qquad (3.44)$$

$$\mathbf{n}_x = [\underbrace{n_x(1,1), n_x(2,1), ..., n_x(m,1)}_{1^{\text{st}},\text{m elements}}, \underbrace{n_x(1,2), n_x(2,2), ..., n_x(m,2)}_{2^{\text{nd}},\text{m elements}},$$
$$..., \underbrace{n_x(1,n), n_x(2,n), ..., n_x(m,n)}_{n^{\text{th}},\text{m elements}}]^T, \tag{3.45}$$

$$\mathbf{n}_y = [\underbrace{n_y(1,1), n_y(2,1), ..., n_y(m,1)}_{1^{\text{st}},\text{m elements}}, \underbrace{n_y(1,2), n_y(2,2), ..., n_y(m,2)}_{2^{\text{nd}},\text{m elements}},$$
$$..., \underbrace{n_y(1,n), n_y(2,n), ..., n_y(m,n)}_{n^{\text{th}},\text{m elements}}]^T, \tag{3.46}$$

$$[\mathbf{V}]_{i,j} := \begin{cases} \mathbf{l}(i)\mathbf{h}(i) & : \quad j = i \\ 0 & : \quad \text{else} \end{cases}, \tag{3.47}$$

$$\left[\mathbf{M}_{x_1}\right]_{i,j} := \begin{cases} -1/\mathbf{l}(i) & : \quad j = i \wedge \mathbf{l}(i) \neq 0 \\ 1/\mathbf{l}(i) & : \quad j = i+1 \wedge \mathbf{l}(i) \neq 0 \\ 0 & : \quad \text{else} \end{cases}, \tag{3.48}$$

$$\left[\mathbf{M}_{x_2}\right]_{i,j} := \begin{cases} -1/\mathbf{l}(i) & : \quad j = i+m \wedge \mathbf{l}(i) \neq 0 \\ 1/\mathbf{l}(i) & : \quad j = i+m+1 \wedge \mathbf{l}(i) \neq 0 \\ 0 & : \quad \text{else} \end{cases}, \tag{3.49}$$

$$\left[\mathbf{M}_{y_1}\right]_{i,j} := \begin{cases} -1/\mathbf{h}(i) & : \quad j = i \wedge \mathbf{h}(i) \neq 0 \\ 1/\mathbf{h}(i) & : \quad j = i+m \wedge \mathbf{h}(i) \neq 0 \\ 0 & : \quad \text{else} \end{cases}, \tag{3.50}$$

$$\left[\mathbf{M}_{y_2}\right]_{i,j} := \begin{cases} -1/\mathbf{h}(i) & : \quad j = i+1 \wedge \mathbf{h}(i) \neq 0 \\ 1/\mathbf{h}(i) & : \quad j = i+m+1 \wedge \mathbf{h}(i) \neq 0 \\ 0 & : \quad \text{else} \end{cases}, \tag{3.51}$$

the matrix form (3.41), denoted as E_1, can be expressed as

$$\sum_{i,j=1,2} \frac{1}{4} \left[(\mathbf{M}_{x_i}\mathbf{n}_x + \mathbf{M}_{y_j}\mathbf{n}_y)^T \mathbf{V} (\mathbf{M}_{x_i}\mathbf{n}_x + \mathbf{M}_{y_j}\mathbf{n}_y) \right]. \tag{3.52}$$

Before deducing the derivatives and Hessian matrix for E_1, two formulations of matrix calculus are introduced below [39]:

$$\frac{\partial \mathbf{u}^{\mathrm{T}}\mathbf{A}\mathbf{v}}{\partial \mathbf{x}} = \mathbf{u}^{\mathrm{T}}\mathbf{A}\frac{\partial \mathbf{v}}{\partial \mathbf{x}} + \mathbf{v}^{\mathrm{T}}\mathbf{A}^{\mathrm{T}}\frac{\partial \mathbf{u}}{\partial \mathbf{x}}, \tag{3.53}$$

$$\frac{\partial \mathbf{x}^{\mathrm{T}}\mathbf{A}}{\partial \mathbf{x}} = \mathbf{A}^{\mathrm{T}}. \tag{3.54}$$

Here, the vectors $\mathbf{u}$ and $\mathbf{v}$ are both functions of the vector $\mathbf{x}$, while the matrix $\mathbf{A}$ is not.

According to (3.53), the derivative of E_1 with respect to $\mathbf{n}_x$ can be formulated

$$\begin{aligned}\frac{\partial E_1}{\partial \mathbf{n}_x} &= \sum_{i,j=1,2}\left[(\mathbf{M}_{x_i}\mathbf{n}_x + \mathbf{M}_{y_j}\mathbf{n}_y)^{\mathrm{T}}\mathbf{V}\mathbf{M}_{x_i} + (\mathbf{M}_{x_i}\mathbf{n}_x + \mathbf{M}_{y_j}\mathbf{n}_y)^{\mathrm{T}}\mathbf{V}^{\mathrm{T}}\mathbf{M}_{x_i}\right] \\ &= \sum_{i,j=1,2}\left[2(\mathbf{M}_{x_i}\mathbf{n}_x + \mathbf{M}_{y_j}\mathbf{n}_y)^{\mathrm{T}}\mathbf{V}\mathbf{M}_{x_i}\right]\end{aligned} \tag{3.55}$$

Following the same procedure, the second derivative of E_1 with respect to $\mathbf{n}_x$ can also be derived

$$\begin{aligned}\frac{\partial}{\partial \mathbf{n}_x}\frac{\partial E_1}{\partial \mathbf{n}_x} &= \frac{\partial}{\partial \mathbf{n}_x}\sum_{i,j=1,2}\left[2(\mathbf{n}_x^{\mathrm{T}}\mathbf{M}_{x_i}^{\mathrm{T}} + \mathbf{n}_y^{\mathrm{T}}\mathbf{M}_{y_j}^{\mathrm{T}})\mathbf{V}\mathbf{M}_{x_i}\right] \\ &= \sum_{i,j=1,2}\left(\mathbf{M}_{x_i}^{\mathrm{T}}\mathbf{V}\mathbf{M}_{x_i}\right)^{\mathrm{T}} \\ &= \sum_{i,j=1,2}\mathbf{M}_{x_i}^{\mathrm{T}}\mathbf{V}\mathbf{M}_{x_i}.\end{aligned} \tag{3.56}$$

The deductions of the derivative $\partial E_1/\partial \mathbf{n}_y$ and the second derivatives $\partial^2 E_1/\partial \mathbf{n}_y^2$, $\partial^2 E_1/(\partial \mathbf{n}_x \partial \mathbf{n}_y)$ are similar and therefore not detailed here.

In this way we can obtain the matrix form of the objective function, the derivatives and Hessian matrix for the free energy. Based on these matrices, the direct method as well as the iterative variant can be used to obtain the vectors $\mathbf{n}$ and $\boldsymbol{\phi}$. For the direct way, the objective function is not taken into consideration and the system of nonlinear equations in (3.34) is solved by the use of the trust-region-dogleg method [40] [41] [42]. For the iterative way, the interior-point method [43] [44] [45] is applied for the minimization of the free energy with respect to $\vec{n}$ in order to fully utilize the objective function. The maximization of the free energy with respect to $\boldsymbol{\phi}$ is considered as an electrostatic problem and solved by (2.32).

Additionally, for the 4-cell system shown in Fig. 3.4, though the simplified FEM scheme doesn't support to determine the discrete form of $\partial^2 n_x/\partial x^2$ directly, we can deduce it in the following way: According to the Euler-Lagrange principle, the derivative of $-(\partial n_x/\partial x)^2/2$ with respect to n_x can be derived

$$\frac{\delta}{\delta n_x}\left[-\frac{1}{2}\left(\frac{\partial n_x}{\partial x}\right)^2\right] = -\frac{1}{2}\left[\frac{\partial}{\partial n_x}\left(\frac{\partial n_x}{\partial x}\right)^2 - \frac{\partial}{\partial x}\frac{\partial}{\partial\left(\partial n_x/\partial x\right)}\left(\frac{\partial n_x}{\partial x}\right)^2\right] = \frac{\partial^2 n_x}{\partial x^2}. \tag{3.57}$$

Therefore, we can obtain the discrete form of $\partial^2 n_x/\partial x^2$ by deducing the derivative to the matrix form of $-(\partial n_x/\partial x)^2/2$ with respect to $\mathbf{n}_x$. For the case specified in Fig. 3.4(a), the simplified FEM scheme will obtain the same result as (3.35). Whereas for the case specified in Fig. 3.4(b), the discrete form is given as

$$\frac{\partial^2 n_x}{\partial x^2} = 2\left[\frac{n_{x_4} - n_{x_5}}{l_1(l_1+l_2)} + \frac{h_1(n_{x_6} - n_{x_5})}{l_2(l_1+l_2)(h_1+h_2)}\right] \tag{3.58}$$

3.3.3 Vector Dynamics

In order to investigate the dynamic orientation of LC, the energy dissipation has to be introduced. Neglecting the translational motion of LC molecules, the dissipation in vector representation reads

$$D = \int_V \frac{1}{2}\gamma_1\left(\dot{n}_x^2 + \dot{n}_y^2 + \dot{n}_z^2\right)\mathrm{d}V, \tag{3.59}$$

where γ_1 is the rotational viscosity, $\dot{n}_x$, $\dot{n}_y$ and $\dot{n}_z$ are the respective derivatives with respect to the temporal variable t. Thus, the dynamic equilibrium equation can be referred to as

$$\frac{\partial E_{\text{free}}}{\partial n_\upsilon} + \frac{\partial D}{\partial \dot{n}_\upsilon} = 0, \tag{3.60}$$

where n_υ denotes n_x, n_y or n_z.

For efficiency reasons and for convenience, explicit time integration is used to solve this equation. In each timestep, equation (3.6) has to be solved to obtain the electric scalar potential. Then, the LC director field $\vec{n}$ is achieved according to (3.60). Supposed that the timestep is small enough, the constraint term can be

omitted from the free energy and the unit length of $\vec{n}$ can be guaranteed simply by renormalisation in each timestep.

3.4 Q-tensor Method

The vector method is based on the assumption that the order parameter remains constant and it further ignores the inversion symmetry due to its vector representation. These assumptions are nearly fulfilled for the numerical simulation of most LC devices. But in some cases where disclinations are present, this method will show singularities of the free energy in these positions. Although this problem can be overcome by special treatment [46], the vector method generally ignores the biaxial arrangement in the vicinity of disclinations or large external fields. A more general method is given by the Q-tensor method based on the Laudau-de Gennes theory. In this method, the tensor order parameter **Q** is defined to describe the biaxial arrangement of LC molecules. Additionally, the thermotropic energy is added to the free energy to dictate the preferred phase of LC.

3.4.1 Tensor Order Parameter

A single LC molecule can be considered to represent a uniaxial system which shows an axis $\hat{a}$ of rotational symmetry as shown in Fig. 3.6(a) [6]. This LC molecule has inversion symmetry which means $\hat{a}$ and -$\hat{a}$ are indistinguishable [1]. Yet it is impossible to simulate each single LC molecule because the LC-based RF components usually have dimensions ranging from micrometers to millimeters, which contain too many molecules. Instead of individual molecular simulation, a macro model is introduced. Based on this, the whole LC device is dicretized into many groups of LC molecules allocated on the grid. For each group of LC molecules, the vector method describes the macro model by vector $\vec{n}$ which is the average of all molecules. This description is not sufficient because it is possible for a group of LC molecules to have biaxial arrangement. Such an arrangement can be depicted in the following way:

As shown in Fig. 3.6(b), denoting director $\hat{n}$ to be the average to all the directions of molecules, we project all the molecules on the plane perpendicular to the director $\hat{n}$. If the projected directions represent a random pattern as shown in Fig. 3.7(a), the overall arrangement is uniaxial. Otherwise, if the projections tends to the same direction denoted as director $\hat{m}$ in Fig. 3.7(b), it indicates a biaxial arrangement of uniaxial LC molecules. This kind of arrangement is usually induced by external forces such as electric fields, surface alignment layers and some topological constraints [47].

Figure 3.6: (a) A single LC molecule (b) A group of LC molecules

Figure 3.7: Projections on the plane perpendicular to $\hat{n}$, (a) uniaxial arrangement, (b) biaxial arrangement

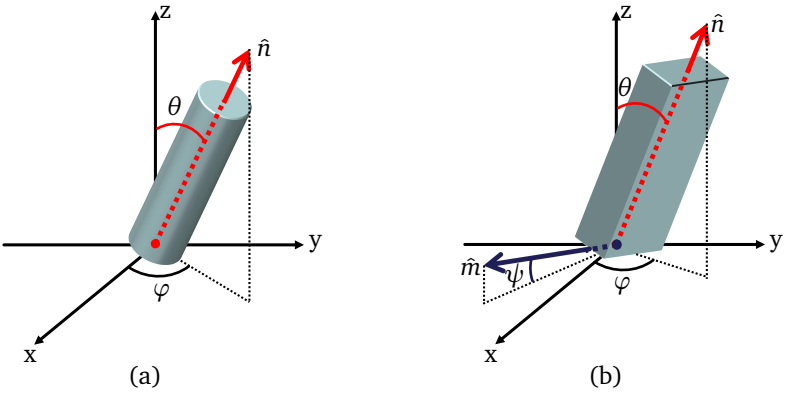

Figure 3.8: (a) Cylindrical representation of uniaxial arrangement (b) Brick representation of biaxial arrangement

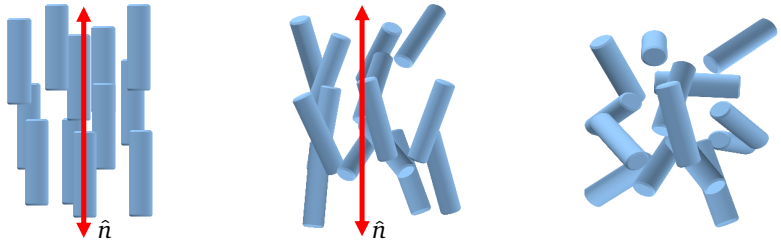

Figure 3.9: Schematic diagram showing different orientational order parameters, **(a)** $S = 1$, **(b)** $S \in (0, 1)$, **(c)** $S = 0$

As shown in Fig. 3.8, the proper geometries to present uniaxial and biaxial arrangements would be cylinder and brick, respectively. The only axis in cylinder stands for director $\hat{n}$. In the brick form, the direction of the longest edge and second longest edge denote $\hat{n}$ and $\hat{m}$, respectively while the shortest edge represents the direction $\hat{n} \times \hat{m}$. The director $\hat{n}$ for both uniaxial and biaxial arrangements can be written as θ-φ expression

$$\hat{n} = \left(\cos\varphi\sin\theta, \sin\varphi\sin\theta, \cos\theta\right). \tag{3.61}$$

Additional description for $\hat{m}$ in biaxial arrangement is [48]

$$\begin{aligned}\hat{m} =&(\sin\varphi\cos\psi - \cos\varphi\sin\psi\cos\theta,\\ &-\sin\varphi\sin\psi\cos\theta - \cos\varphi\cos\psi, \sin\psi\sin\theta),\end{aligned} \tag{3.62}$$

where ψ is the angle between $\hat{m}$ and the vector $(\sin\varphi, -\cos\varphi, 0)$, as shown in Fig. 3.8. It can be found from the expressions of $\hat{n}$ and $\hat{m}$ that the two directions have three degrees of freedom which are θ, ϕ and ψ.

Furthermore, the angle θ_n between $\hat{n}$ and every individual molecule can be obtained. According to the distribution of θ_n, the orientational order parameter S_1 can be defined to measure orientational order

$$S_1 = \frac{1}{2}\int_V \left(3\cos^2\theta_n - 1\right) f(\theta_n)\mathrm{d}V, \tag{3.63}$$

where $f(\theta_n)$ is the distribution function of θ_n. Actually, it is the average value of a second-order Legendre polynomial. The order parameter results in $S_1 = 1$ when the molecules are perfectly ordered as shown in Fig. 3.9(a). In the isotropic case as shown in Fig. 3.9(c), the molecules are randomly oriented so that $S_1 = 0$. For the mesophase between these states, S_1 represents a value between 0 and 1, as shown in Fig. 3.9(b).

The second orientational order parameter S_2 is related to the director $\hat{m}$ and can be obtained in a similar way. Therefore, the tensor order parameter $\mathbf{Q}$ can be composed of

$$\mathbf{Q} = S_1 \hat{n} \otimes \hat{n} + S_2 \hat{m} \otimes \hat{m} - \frac{1}{3}(S_1 + S_2)\mathbf{I}, \tag{3.64}$$

where $\mathbf{I}$ is the identity matrix. It can be derived from this matrix that the three eigenvalues of $\mathbf{Q}$ are

$$\lambda_1 = (2S_1 - S_2)/3, \tag{3.65}$$
$$\lambda_2 = (2S_2 - S_1)/3, \tag{3.66}$$
$$\lambda_3 = -(S_1 + S_2)/3. \tag{3.67}$$

When all eigenvalues are different, this group of LC molecules formulate a biaxial arrangement. If two of those eigenvalues are identical, it is in uniaxial arrangement. It is isotropic when all the eigenvalues are the same.

It can be observed from (3.61), (3.62) and (3.64) that the tensor order parameter $\mathbf{Q}$ can be constructed by five variables θ, ϕ, ψ, S_1 and S_2. Unfortunately, in simulation, it is inconvenient to apply this description directly. A substitutable way would be to formulate $\mathbf{Q}$ in a five dimensional subspace [49]

$$\mathbf{Q} = \sum_{i=1,2,\ldots,5} q_i \mathbf{T}_i, \tag{3.68}$$

where $\mathbf{T}_i$ are basis tensors of the form [49]

$$\mathbf{T}_1 = (3\hat{e}_z \otimes \hat{e}_z - \mathbf{I})/\sqrt{6}, \tag{3.69}$$
$$\mathbf{T}_2 = (\hat{e}_x \otimes \hat{e}_x - \hat{e}_y \otimes \hat{e}_y)/\sqrt{2}, \tag{3.70}$$
$$\mathbf{T}_3 = (\hat{e}_x \otimes \hat{e}_y + \hat{e}_y \otimes \hat{e}_x)/\sqrt{2}, \tag{3.71}$$
$$\mathbf{T}_4 = (\hat{e}_x \otimes \hat{e}_z + \hat{e}_z \otimes \hat{e}_x)/\sqrt{2}, \tag{3.72}$$
$$\mathbf{T}_5 = (\hat{e}_y \otimes \hat{e}_z + \hat{e}_z \otimes \hat{e}_y)/\sqrt{2}. \tag{3.73}$$

Here, the symbols $\hat{e}_x$, $\hat{e}_y$ and $\hat{e}_z$ are unit vectors along the x, y, z axes, respectively. Thus, the Q tensor can be rewritten as

$$\mathbf{Q} = \begin{pmatrix} \frac{q_2}{\sqrt{2}} - \frac{q_1}{\sqrt{6}} & \frac{q_3}{\sqrt{2}} & \frac{q_4}{\sqrt{2}} \\ \frac{q_3}{\sqrt{2}} & -\frac{q_2}{\sqrt{2}} - \frac{q_1}{\sqrt{6}} & \frac{q_5}{\sqrt{2}} \\ \frac{q_4}{\sqrt{2}} & \frac{q_5}{\sqrt{2}} & \frac{2q_1}{\sqrt{6}} \end{pmatrix} \tag{3.74}$$

It is obvious that the symmetric and traceless properties of Q tensor is guaranteed in this expression and that the five degrees of freedom q_1, q_2,..., q_5 are properly represented.

3.4.2 Landau-de Gennes Energy

Elastic Energy

Based on the tensor order parameter **Q**, the elastic energy in (3.23) can be rewritten as [50]

$$f_{\text{elastic}} = \sum_{i,j,k=1,2,3} \left[\frac{L_1}{2} \left(\frac{\partial Q_{ij}}{\partial x_k} \right)^2 + \frac{L_2}{2} \frac{\partial Q_{ij}}{\partial x_j} \frac{\partial Q_{ik}}{\partial x_k} \right] + \sum_{i,j,k,l=1,2,3} \frac{L_6}{2} Q_{lk} \frac{\partial Q_{ij}}{\partial x_l} \frac{\partial Q_{ij}}{\partial x_k}, \tag{3.75}$$

where x_1, x_2 and x_3 denote x, y and z in the Cartesian coordinate system, Q_{ij} represents the $(i,j)^{\text{th}}$ element of Q tensor, L_1, L_2 and L_6 are elastic parameters which are related to the Frank elastic constants by [50]

$$L_1 = \frac{1}{6S_0^2}(K_{33} - K_{11} + 3K_{22}), \tag{3.76}$$

$$L_2 = \frac{1}{S_0^2}(K_{11} - K_{22}), \tag{3.77}$$

$$L_6 = \frac{1}{2S_0^3}(K_{33} - K_{11}). \tag{3.78}$$

The variable S_0 represents the uniaxial order parameter which is evaluated at the same temperature with the Frank elastic constants.

Electric Interaction Energy

A similar substitution can be applied to the vector representation of the permittivity tensor $\boldsymbol{\varepsilon}$ in (3.29). Thus, we obtain the Q-tensor representation in the form

$$\boldsymbol{\varepsilon} = \frac{2\varepsilon_{\perp} + \varepsilon_{\parallel}}{3}\mathbf{I} + \frac{\varepsilon_{\parallel} - \varepsilon_{\perp}}{S_0}\mathbf{Q}. \tag{3.79}$$

By substituting (3.79) into (3.5), the tensor representation of the electric interaction energy can be obtained

$$f_{\text{electric}} = -\frac{1}{2}\sum_{i,j=1,2,3}\left[\frac{2\varepsilon_{\perp} + \varepsilon_{\parallel}}{3}\left(\frac{\partial\phi}{\partial x_i}\right)^2 + \frac{\varepsilon_{\parallel} - \varepsilon_{\perp}}{S_0}Q_{ij}\frac{\partial\phi}{\partial x_i}\frac{\partial\phi}{\partial x_j}\right]. \tag{3.80}$$

Thermotropic Energy

According to the Landau-de Gennes theory, the thermotropic energy term is also imposed in the tensor representation of the free energy. This energy term is used to dictate in which phase (isotropic, uniaxial or biaxial) the LC molecules would prefer to reside. The thermotropic energy density can be approximated using a Taylor expansion [51]

$$f_{\text{thermotropic}} = f_0 + \frac{1}{2}A(T)\text{tr}(\mathbf{Q}^2) + \frac{1}{3}B(T)\text{tr}(\mathbf{Q}^3) + \frac{1}{4}C(T)\left[\text{tr}(\mathbf{Q}^2)\right]^2. \tag{3.81}$$

Due to the traceless of $\mathbf{Q}$, there is no linear term in this equation. Therefore, this energy term will always have a local minimum in the isotropic state: $\mathbf{Q}$=0. In general, the coefficients $A(T)$, $B(T)$ and $C(T)$ are dependent on the temperature T. For simplicity, it can be assumed that $B(T)$ and $C(T)$ are temperature independent, and $A(T)$ depends linearly on the temperature. The linear expression is then given by $A(T) = \alpha(T - T^*)$, where T^* is supercooling temperature, below which the isotropic phase is unstable.

It is known that

$$\text{tr}\,(\mathbf{Q}^n) = \sum_i \lambda_i^n. \tag{3.82}$$

By substituting the eigenvalues in (3.65), (3.66) and (3.67) into (3.81), the thermotropic energy can be stated as a function of S_1 and S_2

$$f_{\text{thermotropic}} = f_0 + \frac{1}{3}A(T)(S_1^2 - S_1S_2 + S_2^2) + \frac{1}{27}B(2S_1^3 - 3S_1^2S_2 - 3S_1S_2^2 + 2S_2^3) + \frac{1}{9}C(S_1^2 - S_1S_2 + S_2^2)^2. \tag{3.83}$$

For the uniaxial phase ($S_2 = 0$), it can be rewritten as

$$f_{\text{thermotropic}} = f_0 + \frac{1}{3}A(T)S_1^2 + \frac{2}{27}BS_1^3 + \frac{1}{9}CS_1^4. \tag{3.84}$$

The stationary values of this equation can be obtained by solving $df_{\text{thermotropic}}/dS_1 = 0$ analytically. The three roots are given by

$$S_1 = 0, \tag{3.85}$$

$$S_1 = \frac{-B + \sqrt{B^2 - 24A(T)C}}{4C}, \tag{3.86}$$

$$S_1 = \frac{-B - \sqrt{B^2 - 24A(T)C}}{4C}. \tag{3.87}$$

The first and second root refer to the isotropic and nematic phase, respectively. The third one is metastable with a negative value in a specific temperature range and either unstable or not defined in another temperature range.

Substituting the three expressions into (3.84), we obtain three functions related to the temperature. In Fig. 3.10, the three temperature-dependent functions denoted as f_1, f_2 and f_3, are plotted for 5CB (4-cyano-4'-npentylbiphenyl), which has the following thermotropic parameters: $\alpha = 1.95 \times 10^5$ J/Km^3, $B = -7.2 \times 10^6$ J/m^3, $C = 8.775 \times 10^6$ J/m^3, $T^* = 34.1$°C [52]. In this figure, the bold line indicates the global minimum values of the thermotropic energy, the dotted line means either the local minimum values of the thermotropic energy with negative S_1 or the local maximum values of the thermtropic energy, and the thin line represents the local minimum values (but not the global minimum values) of the thermotropic energy. We can observe three critical temperature: $T^* = 34.1$°C, below which the isotropic phase is unstable but the nematic phase is stable, $T_c = 35.22$°C, the clearing point where both the isotropic phase and ne-

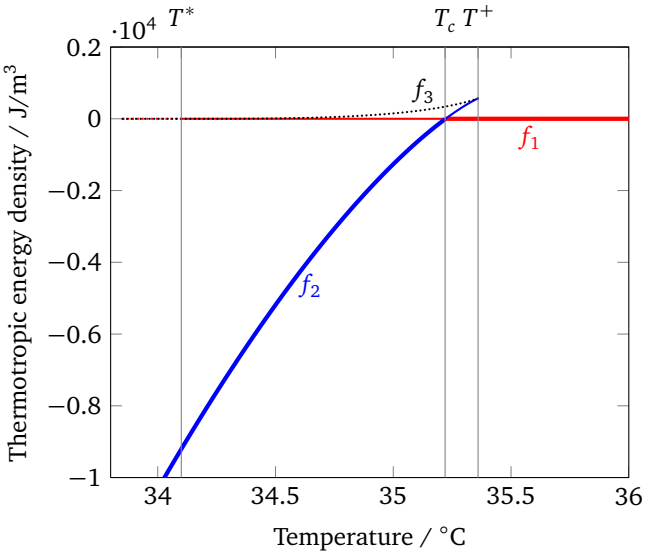

Figure 3.10: Thermotropic energy of three roots as a function of temperature

matic phase are stable, and $T^+ = 35.36°\text{C}$, above which only the isotropic phase is stable. The values T_c and T^+ can be formulated as

$$T^+ = T^* + \frac{B^2}{24\alpha C}, \tag{3.88}$$

$$T_c = T^* + \frac{B^2}{27\alpha C}. \tag{3.89}$$

Furthermore, we plot the thermotropic energy as a function of order parameter S_1 for different temperatures: $T_1 = 37.36°\text{C}$, $T^+ = 35.36°\text{C}$, $T_c = 35.22°\text{C}$, $T^* = 34.1°\text{C}$ and $T_5 = 32.1°\text{C}$. It can be seen that for the temperature T_1, the global minimum lies on $S_1 = 0$, which means only the isotropic phase is stable. If the temperature falls to $T_c < T < T^+$, the global minimum still lies on the isotropic phase, yet the nematic phase becomes metastable. At the critical temperature T_c, the free energies of the isotropic phase and nematic phase are the same so that both phases are stable. In the temperature range $T^* < T < T_c$, the nematic phase exhibits a global minimum, while the isotropic phase is metastable. When the temperature decreases to T_5, the nematic phase becomes the only stable phase.

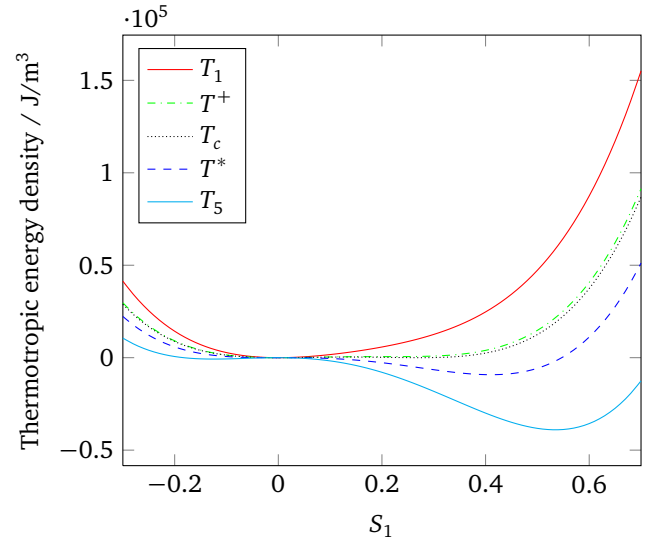

(a)

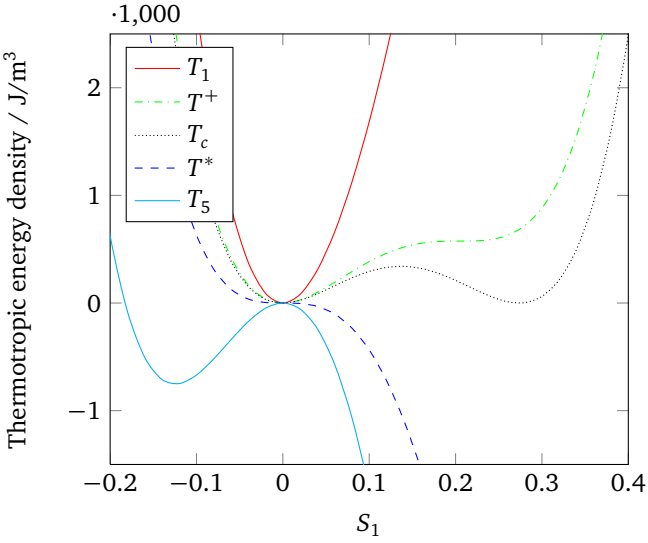

(b)

Figure 3.11: (a) Thermotropic energy density as a function of order parameter S_1 (b) Partial enlargement of (a)

Actually, the nematic-isotropic transition of LC is a weak first-order transition. If it is cooled down from a temperature higher than T^+ to the temperature T_c, the order parameter can't change discontinuously from the isotropic phase to nematic phase because there is an energy barrier between them. This energy barrier will disappear when the temperature decreases to T^*. It is at this temperature that the LC can transform to nematic phase. Therefore, this temperature is called supercooling temperature. The heating of the nematic LC results in a similar process and the temperature T^+ is called superheating temperature.

3.4.3 Q-tensor Statics

The equilibrium state of LC can be obtained by solving (3.4) in the Q-tensor representation. By the use of expression (3.74), equation (3.4) becomes

$$\frac{\partial E_{\text{free}}(q_\upsilon)}{\partial q_\upsilon} = 0, \frac{\partial E_{\text{free}}(\phi)}{\partial \phi} = 0, \tag{3.90}$$

where υ=1,2,...5. In order to apply the simplified FEM scheme, q_υ and ϕ are expanded by Whitney node elements

$$q_\upsilon = \sum_{j \in LC} q_{\upsilon j} w_{pj}, \tag{3.91}$$

$$\phi = \sum_j \phi_j w_{pj}. \tag{3.92}$$

Substituting them into the free energy formulation and applying trapezoidal integration, the resulting expression can be formulated as a function of $q_{\upsilon j}$ and ϕ_j. Collecting all the values of $q_{\upsilon j}$ and ϕ_j in the vectors $\mathbf{q}$ and $\boldsymbol{\phi}$, respectively, the free energy can be expressed as a matrix function of $\mathbf{q}$ and $\boldsymbol{\phi}$. According to the knowledge of matrix calculus, both the derivatives and the Hessian matrix can be deduced.

The obtained optimization problem based on the Q-tensor method can be solved with the direct and iterative methods already applied to the vector-method approach. In the direct way, the trust-region-dogleg method is applied for solving the system of nonlinear equations. Following the iterative variant, the first equation is solved by the trust-region method [53] [54] where the objective function is utilized, while the second equation is treated as an electrostatic problem.

3.4.4 Q-tensor Dynamics

In order to achieve the dynamic orientation of LC with the help of the Q-tensor method, the dissipation in (3.60) can be rewritten as

$$D = \int_V \frac{1}{2}\gamma \mathrm{tr}(\dot{\mathbf{Q}}^2)\mathrm{d}V, \tag{3.93}$$

where γ is related to the rotational viscosity γ_1 by $\gamma = \gamma_1/(2S_0^2)$ and $\dot{\mathbf{Q}}$ denotes the derivative of $\mathbf{Q}$ with respect to the temporal variable. If the five-element expression in (3.74) is applied, the dissipation becomes

$$D = \int_V \frac{1}{2}\gamma(\dot{q}_1^2 + \dot{q}_2^2 + \dot{q}_3^2 + \dot{q}_4^2 + \dot{q}_5^2)\mathrm{d}V. \tag{3.94}$$

The dynamic equilibrium can then be formulated as

$$\frac{\partial E_{\mathrm{free}}}{\partial q_v} + \frac{\partial D}{\partial \dot{q}_v} = 0. \tag{3.95}$$

In most applications, the derivative of the thermotropic energy with respect to the Q tensor is much bigger than the derivative of all other terms in the free energy. Even a small change in the Q tensor might cause a significant variation in this derivative. Within the explicit time integration, this derivative term usually leads to big oscillations in the numerical solution. In order to guarantee the stability of an explicit method, the timestep should be extremely small [55] because the dynamic equilibrium equation formulates a stiff problem. For this kind of problems, the implicit method is better suited. Here, we choose a 2-stage SDIRK scheme because it is L-stable and has a second-order convergence of discretization error [56]. Its Butcher-scheme is shown below

α_{rk}	α_{rk}	
1-α_{rk}	1-2α_{rk}	α_{rk}
	1/2	1/2

,

with $\alpha_{\mathrm{rk}} = (2-\sqrt{2})/2$. According to this scheme, two nonlinear system of equations are solved by the Trust-region-dogleg method in each timestep.

3.5 Comparisons of Vector and Q-tensor Method

In the previous paragraphs, the vector method based on the Oseen-Frank theory and the Q-tensor method based on the Landau-de Gennes theory are both introduced. They provide two different ways to determine the LC director field orientation from a given electrode setup and voltage excitation. This section aims to compare these two methods while highlighting their specific features for realistic applications.

The comparison of the vector method and the Q-tensor method has already been presented in [57]. However, we believe that their tensor approach is based on a constant order parameter model because the thermotropic energy is not included in their tensor approach. They perform a one-dimensional (1D) simulation of a π-cell with both methods and find that the Q-tensor method allows topological transitions between inequivalent states while the vector method doesn't. So they conclude that the vector method is superior to the Q-tensor method.

It is true that the Q-tensor method has such disadvantages when the applied voltage is low, no matter whether it is based on a constant order parameter model or a variable order parameter model. In order to verify this, a similar π-cell will be simulated with both the vector method and variable-order tensor implementations. The results will be discussed in the following paragraphs.

The reason for setting up a new comparison is that in [57] one situation has not been considered. It is that the topological transitions between inequivalent states can occur when the applied voltage is large enough [35] [52]. The Q-tensor method is suitable for such simulations because of its capability in describing biaxial arrangements. Dedicated simulations of disclinations and a detailed discussion will also be presented in this section.

3.5.1 π-cell

The π-cell texture [58] is used here for the comparisons of the vector and the Q-tensor method. In this texture, the molecules of both surfaces are aligned with a predifined angle in opposite directions, as shown in Fig. 3.12. This cell can switch between two topologically inequivalent states which are called the H-state and V-state. The former, shown in Fig. 3.12(a), yields a splay distortion. The latter is shown in Fig. 3.12(c) with the vertical or bend state. There is an energy barrier between these two states which prevents a spontaneous transition between them. But this energy barrier can be overcome by a large electric field with a threshold of 5-10 V/µm, which is temperature dependent [52]. When an electric field is applied to the H-state, the π-cell will transform to an intermediate state (I-state)

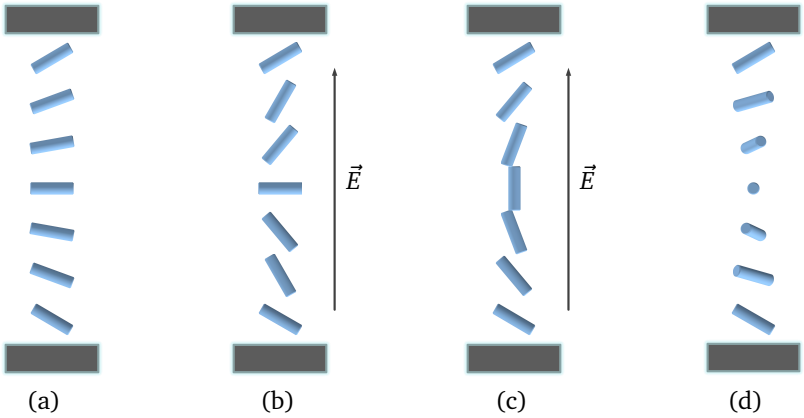

Figure 3.12: Four different states of π-cell: (a) H-state (b) I-state (c) V-state (d) T-state

in Fig. 3.12(b) which is topologically equivalent to the H-state. Assumed that the electric filed is large enough, the order reconstruction will happen in the tilted wall of the I-state and it will give rise to the V-state. In the absence of any electric field, the V-state will actually relax to the twisted state (T-state) shown in Fig. 3.12(d), which is topologically equivalent to the V-state, if the pre-tilted angle and the ratio between K_{22} and K_{33} is small enough [52].

3.5.2 Simulation of π-cell

We perform a one-dimensional simulation of the specified π-cell with a thickness of 2 μm and a pre-tilted angle of 10°. The 5CB compound is chosen as nematic material with the thermostropic coefficients mentioned before. The relative permittivity of the long axis is given by $\varepsilon_{r,\parallel} = 17$ and that of the perpendicular direction by $\varepsilon_{r,\perp} = 6.8$ for the order parameter $S_0 = 0.65$ [59]. The elastic constants are $K_{11} = 6.3 \times 10^{-12}$ N, $K_{22} = 3 \times 10^{-12}$ N, $K_{33} = 9 \times 10^{-12}$ N for $S_0 = 0.65$ [60]. According to equations (3.76) (3.77) (3.78), it can be derived that $L_1 = 4.6 \times 10^{-12}$ N, $L_2 = 7.8 \times 10^{-12}$ N, and $L_6 = 4.9 \times 10^{-12}$ N.

Vector and tensor simulation of π-cell in lower voltage

Firstly, we perform the vector and Q-tensor simulations of H-state with an applied voltage of 3 V at a temperature of 29.2°C. It should be noticed that the

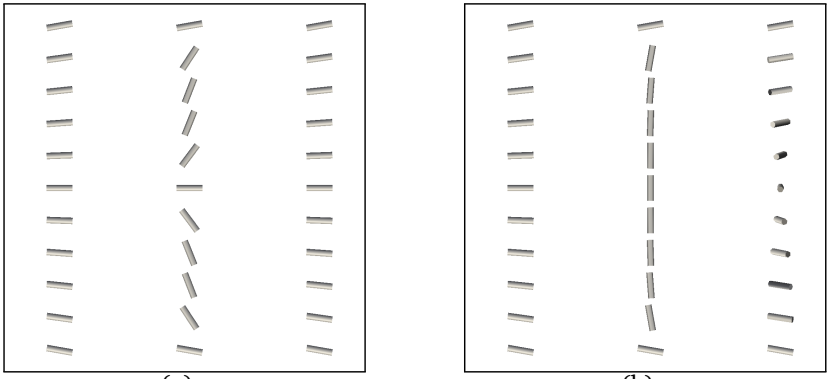

Figure 3.13: Director field of a π-cell in the initial state, in an applied voltage of 3 V and after removing the excitation, simulated by (a) the vector method, (b) the Q-tensor method. A 1D-mesh of 11 nodes is applied and displayed

electric field strength is about 1.5 V/μm which is not large enough to induce a topological transition between inequivalent states. We keep the voltage constant until the molecules orient to a steady state. Then the excitation is removed and the molecules are given enough time to relax.

Fig. 3.13 shows the simulation results of the π-cell in the initial state, in an excited state with an applied voltage of 3 V and after removing the excitation, based on both the vector method and the Q-tensor method in a 1D-mesh with 11 nodes. It can be clearly seen that the orientations of the central directors are continuously changed by nearly 180° in the vector method. Whereas for the Q-tensor method, due to inversion symmetry of $\vec{n}$, the neighbouring nodes in the center have nearly the same direction. Actually, the vector method reveals a H-I transformation while the Q-tensor method performs a H-V transformation for the applied voltage of 3 V. When the field is switched off, the π-cell relaxes back to H-state in the vector method while it transforms to T-state in the Q-tensor method. As mentioned before, H-state and V-state or T-state are topologically inequivalent states which shouldn't happen for the applied voltage of 3 V. Therefore, the Q-tensor method gives a physically incorrect result for the specified coarse mesh.

Moreover, we perform the same simulation with the Q-tensor method on a denser mesh with 51 nodes. As shown in Fig 3.14, we display the directors sampled

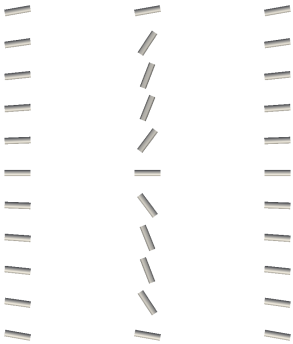

Figure 3.14: Director field of the π-cell in the initial state, at an applied voltage of 3 V and after removing the excitation, simulated by the Q-tensor method. A 1D-mesh of 51 nodes is applied while for visualization reasons only values at every 5 nodes are displayed

at every 5 nodes. In this dense mesh, the Q-tensor method provides the same H-I-I transformation as the vector method.

These simulations reveal one disadvantage of the Q-tensor method. It switches non-physically between topologically distinct states if the mesh is too coarse while the vector method doesn't have such problem [57]. Yet this situation can always be overcome by an appropriate fine mesh. It is further suggested by [61] that an adaptive meshing scheme is suitable for the Q-tensor method to avoid such behaviors.

Vector and tensor simulation of π-cell in higher voltage

We increase the applied voltage to 50 V and simulate the π-cell with both two methods again. At such high voltages, the electric field strength is about 25 V/μm which is higher than the threshold for H-V transformation.

A 1D-mesh with 501 nodes is applied and for visualization reasons, the directors are sampled at every 50 nodes. As shown in Fig. 3.15, the Q-tensor method depicts the H-V-T transformation correctly while the vector method fails.

The process of topological transformations of H-V can be illustrated by Fig. 3.16 as a series of temporal snapshots, where only 9 nodes in the center of the π-cell (0.98-1.02 μm) are selected for visualization. The background colour stands for the first orientational order parameter S_1. The cylinders represent the director $\hat{n}$ and are scaled by S_1. As shown in this figure, the molecules in the center of the π-cell start H-state and transform to I-state where the molecules show splay

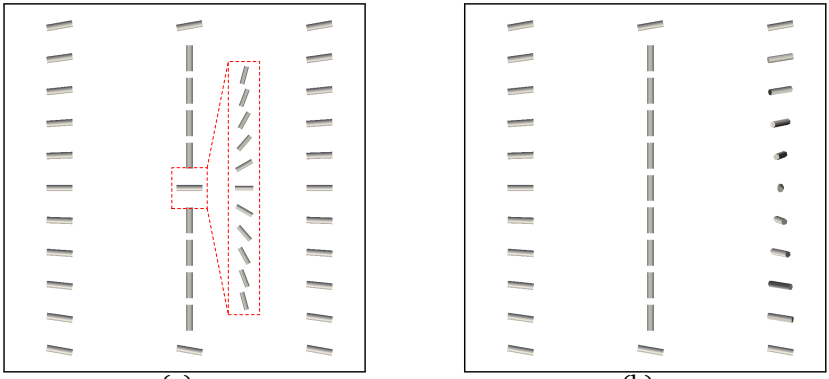

Figure 3.15: Director field of the π-cell in the initial state, at an applied voltage of 50 V and after removing the excitation, simulated by (a) the vector method (where the center region of 0.98-1.02 μm is zoomed in for the π-cell in an applied voltage of 50 V), (b) the Q-tensor method. A 1D-mesh of 501 nodes is applied and displayed every 50 nodes

distortion. Since the voltage applied is high enough, the electric field will continue to compress the molecules in this region so that S_1 decreases and S_2 increases until $S_1 = S_2$. After this time instant, the director $\hat{n}$ and $\hat{m}$ exchange and so do their corresponding orientational order parameter S_1 and S_2. Then gradually S_1 increases to the bulk equilibrium value and S_2 decreases to zero, which describes the V-state in the last timestep.

It is shown by these simulations that the Q-tensor method based on the Laudau-de Gennes theory can indeed simulate the topologically transitions between distinct states due to its capability in handling biaxial arrangements, whereas the vector method couldn't handle these transitions.

Further study of π-cell

Besides the simulations shown previously, we also perform tensor modeling of this π-cell with different applied voltages or with a T-state as an initial condition. Assumed that the temperature is fixed at 29.2°C and a 1D-mesh with 501 nodes is applied, we can obtain the free energy as a function of voltage for two topologically distinct states (T or V-state and H or I-state), which is shown in Fig. 3.17. As specified in Fig. 3.17(a), there is a critical voltage (approximately 1.25 V) where the two topologically distinct states result in the same free energy. Beyond this voltage,

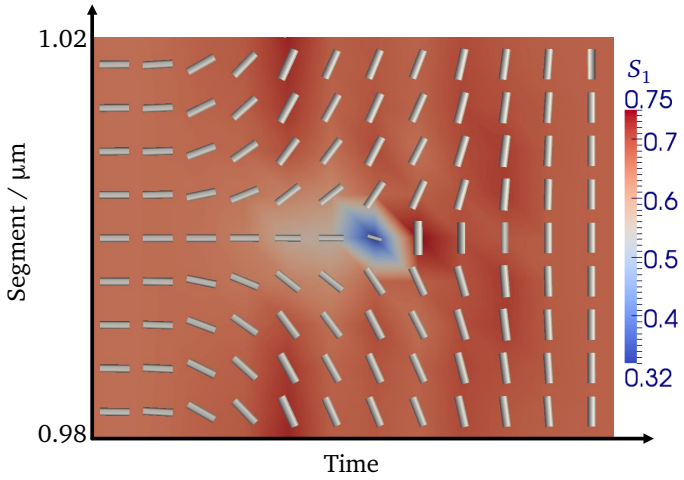

Figure 3.16: Topological transition of H-V versus non-equidistant timestep depicted by the Q-tensor method. The directors in the center region of 0.98-1.02 μm are selected for visualization.

the V-state becomes the global minimum energy state. Yet the π-cell starting with H-state couldn't transform into V-state because of the energy barrier between them. This energy barrier can't be overcome until the applied voltage is as high as 39 V, as shown in Fig. 3.17(b). Thus, an electric field strength of 19.5 V/μm formulates the threshold for the H-V transformation at a temperature of 29.2°C.

The threshold of the electric field strength at other temperatures can also be obtained so that we can plot the temperature dependence of the threshold achieved by the Q-tensor method in Fig. 3.18. The experimental data in [52] is also included for comparison. As shown in this figure, the Q-tensor method tends to overestimate the threshold value of the electric field strength. A possible reason is given by [52] that the theory used here may not be rigorous enough to describe the biaxial phase. Maybe it is necessary to employ four orientational order parameter [62].

3.5.3 Disclinations

Most of LC devices apply alignment layers to guarantee a uniform orientation of the director field. When the boundary conditions imposed by coated alignment layers are continuously degenerate (tangential or conical, without any preferred direction on the alignment layers), it would be usual to observe some dark and

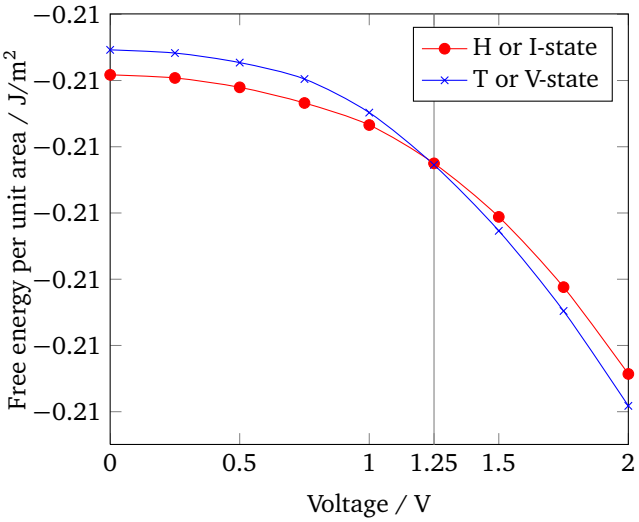

(a)

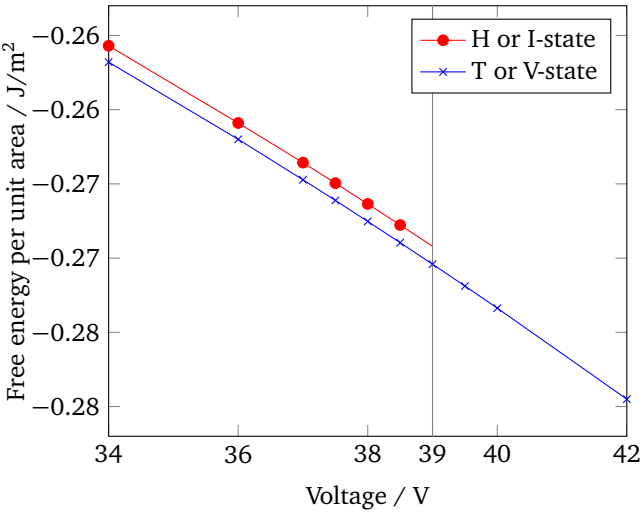

(b)

Figure 3.17: Thermotropic energy density versus applied voltage for different initial states. (a) Voltages range from 0 to 2 V, (b) Voltages range from 34 to 42 V

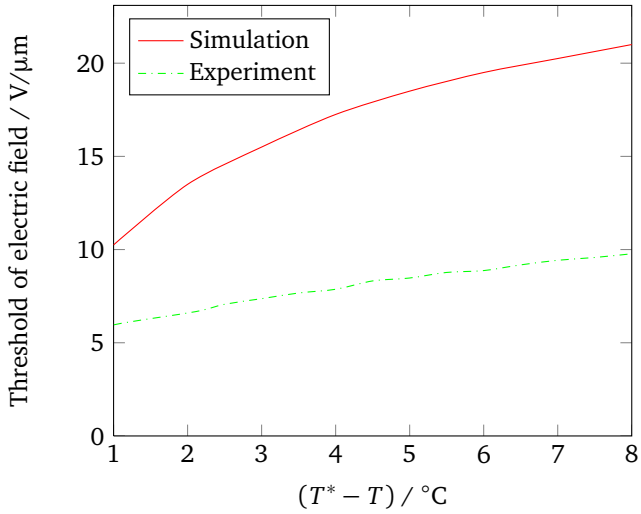

Figure 3.18: Comparison of threshold versus temperature obtained by simulation and experiment [52]

flexible filaments by a polarising microscope [1]. The analysis of such kind of texture by Grandjean and G. Friedel suggests that they are not caused by impurities, but corresponds to discontinuities in the director. They are called disclinations by Frank [1].

Several types of disclinations which are indexed with $m = +1$, -1, $+1/2$ and -1/2 are shown in Fig. 3.19. The index m is achieved in the following way: Take the $+1/2$ disclinations in Fig. 3.20 for example, we assume that it is located on a XY-plane with the singular point representing the origin. If we draw a closed circuit around the singular point and sample the molecules on this circuit, it can be seen that the angles of those molecules with the x axis have changed by π, which is $+1/2$ of 2π. Thus, this disclination is denoted with $m = +1/2$.

Among these types of disclinations, the ones with half-integral index are referred to as discontinuity located on lines while the ones with integral index are associated with either lines or points [35]. Disclinations with indexes larger that 1/2 tends to split into several 1/2 disclinations and move apart to reduce the free energy [63].

Besides alignment layers, external field could also be responsible for the formation of dislinations. It was explained in [1] for example that a large enough magnetic field could induce a transition from a tilted wall to a set of two disclinations with index -1/2 and $+1/2$. This process is called pincement and was first

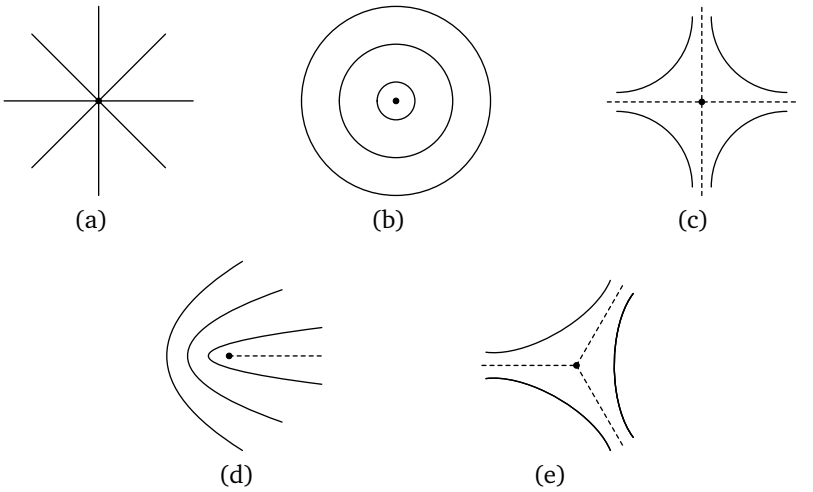

Figure 3.19: Four types of disclinations with the index of (a) m=+1, (b) m=+1, (c) m=-1, (d) m=$+\frac{1}{2}$, (e) m=-$\frac{1}{2}$

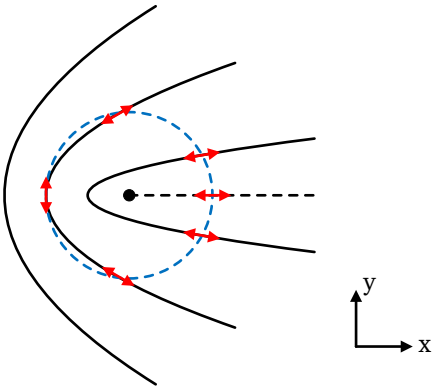

Figure 3.20: Schematic diagram showing the angles of those molecules on the closed circuit around the singular point

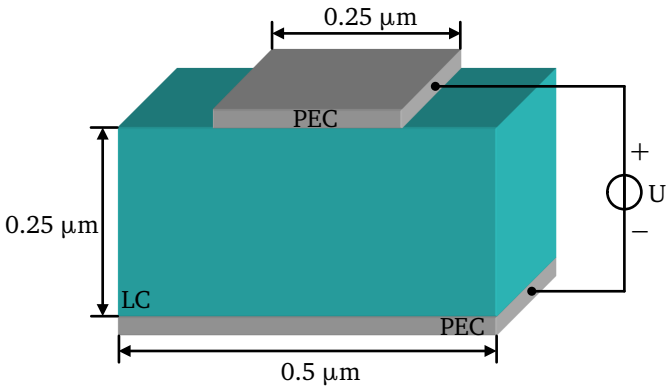

Figure 3.21: Schematic diagram of a microstrip-like structure filled with liquid crystals

observed by R. B. Mayer. It was proved that pincements could also be induced by electric fields [64]. In the following paragraphs, we will simulate this behaviour by the use of the Q-tensor method.

3.5.4 Modeling of Disclinations

For the study of disclinations, we have applied a microstrip-like structure shown in Fig. 3.21. There are two electrodes consisting of perfect electric conductor (PEC), with LC filled between them. The top and bottom layers of the LC are coated with homogeneous alignment layers while the left and right sides of the LC are coated with homeotropic alignment layers. From this configuration, it can be guaranteed that the molecules have a uniform direction of 0° in the absence of any electric field. If an external voltage source is applied to the two electrodes, two distortion pattens will be formed on the left side and right side of the top electrode according to the direction of the electric field strength, as shown in Fig. 3.22. The two distortion patterns will move towards the center of the structure until they finally touch each other and achieve a balance. The border between two domains of different distortions involve a tilted wall. If the electric field strength is strong enough, the tilted wall will transform to a set of two disclinations with index of -1/2 and +1/2.

The LC material chosen in this simulation is 5CB with the coefficients mentioned before at a temperature of 29.2°C. The entire model can be simulated using a two-

Figure 3.22: Two distortion patterns of LC orientation arising on the two sides of electrodes

dimensional grid with an non-equidistant mesh of 37×65 nodes which is denser in the center. We apply two different voltages of 1.5 V and 8 V to it and achieve the director field in respective strengths of electric field as shown in Fig. 3.23 and 3.24, respectively. For visualization reasons, all results are sampled using a mesh of 21×11 nodes. It can be seen that there is a tilted wall and the distortion in the center is of bend type for an applied voltage of 1.5 V. (Due to the tiny asymmetry caused by simulation error, the state shown in Fig. 3.23 is unstable, therefore the tilted wall will move to either left side or right side of the whole structure.) When the voltage increases to 8 V, the tilted wall disappears and two disclinations with index -1/2 and +1/2 emerge on the top and on the bottom, respectively. An enlarged view of both disclinations is shown in Fig. 3.24 using a denser mesh. The background colour stands for S_1 which ranges from 0.66 to 0.3. The cylinders represent the director $\hat{n}$ multiplied by S_1. It can be observed that the value of S_1 is small in the center of disclinations, across which the distortion of molecules transforms from bend to splay or from splay to bend.

3.5.5 Conclusions

It has been demonstrated by these simulations that the Q-tensor method can be applied to more extensive simulations provided a fine mesh is given. The vector method is confined to the simulation of cases which are not involved with discli-

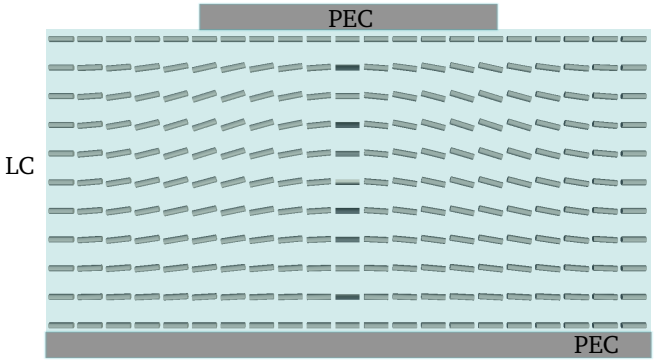

Figure 3.23: Director field of the microstrip-like structure in an applied voltage of 1.5 V, calculated by the Q-tensor method

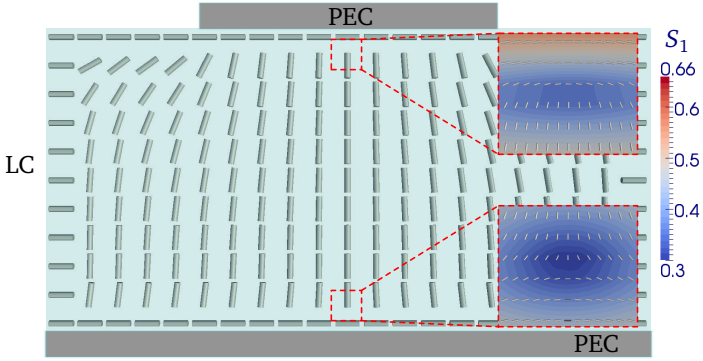

Figure 3.24: Director field of the microstrip-like structure in an applied voltage of 8 V, calculated by the Q-tensor method, with the enlarged view of the dislinations

nations or topological transitions between distinct states. We also need to notice the computational cost of the Q-tensor method. This method is more complex to implement and sometimes requires a denser mesh than the vector method.

According to these findings, we suggest to use the Q-tensor method when there are disclinations present in the simulations or the external forces (for example, electric field or magnetic field) applied are large enough to induce topological transitions between inequivalent states or apparent biaxial arrangement of molecules. Otherwise, the vector method would be the proper choice since it has a less computational cost.

4 Propagation of Electromagnetic Fields in Liquid-Crystal Materials

The simulation of electromagnetic wave propagation in tunable LC based RF devices can be formulated as a two-step process. In the first step, the LC director field orientation in a static electric field has to be determined and was already investigated in the last chapter. The current chapter will concentrate on the second step which describes the simulation of high-frequency electromagnetic wave propagating in LC.

Usually, the orientations of LC molecules are spatially distributed in such devices. So they can be considered to be described as a continuously varying tensor dielectric material. Since LC can flow like liquid, there are often copper, plastic or other materials containing it. This means we need to handle the interface between tensor dielectric material and PEC, isotropic material, or sometimes another tensor dielectric material in the numerical simulation, besides continuously varying tensor dielectric material.

In this chapter, the effective dielectric method is applied to deal with the tensor dielectric boundary. With the help of the simplified FEM, we construct an inverse permittivity matrix which can guarantee the space stability. Then, a small modification is introduced to the traditional update scheme in order to make sure that the tangential electric fields on the PEC boundary vanish. In the last section of this chapter, this algorithm is applied to the simulation of a representative test example to demonstrate its capabilities.

4.1 Material Modeling

According to (2.41), the inverse permittivity matrix is required to setup the time-domain simulation of high-frequency problems. The common way to obtain this matrix is given by the inverse of the permittivity matrix $\mathbf{M}_\varepsilon$. This procedure works fine for isotropic and diagonal tensor dielectric materials because $\mathbf{M}_\varepsilon$ forms a diagonal matrix for these materials. The inverse will be obtained by simply inverting the diagonal elements such that the inverted matrix will remain to be diagonal. But for tensor dielectric materials, it is shown in the previous chapter that $\mathbf{M}_\varepsilon$ results in a non-diagonal sparse matrix. We know that the inverse of sparse matrices could

be fully populated which is accompanied by huge computational costs. Thus, it is necessary to rebuild the inverse permittivity matrix $\mathbf{M}_{\xi}$ instead of achieving it by direct inverse of $\mathbf{M}_{\varepsilon}$.

For the construction of $\mathbf{M}_{\xi}$, the discontinuities of the electric field strength and the electric flux density presented at the boundaries of the tensor dielectric materials attract special attention because of their relevance to the numerical accuracy. In the scope of FDM, there are mainly two ways to handle the dielectric boundary: those modifying the standard differential operators of Maxwell's equations at the boundary, and those based on standard FDM but altering the constitutive material matrices [65]. A representative method in the category of the first method is proposed by [32]. In this work, the unknown components of the electric field strength and electric flux density are multiply defined on the edges of the primary grid, according to the number of different permittivities presented in the adjacent grid cells. Non-standard differential operators are applied in order to assure the tangential continuity of the electric field strength at the interface. Yet this reference is constrained to the staircase model where a curved object is approximated as a set of individual cubes.

The second method deduces the constitutive material matrices according to the information of dielectric boundaries while preserving the standard differential operators. The triangular filling technique [24], the tetrahedral filling technique[66] or the perfect boundary approximation (PBA) technique [67] in FIT all fall into this category [68]. It is stated in [67] that PBA can achieve second-order accuracy for arbitrary shaped boundaries of isotropic materials.

For the tensor dielectric boundaries, the authors in [65] propose a frequency-domain electromagnetics algorithm which ensures second-order convergence. But the inverse permittivity matrix achieved in this algorithm is asymmetric, thus this method is not preferred for time-domain simulations. The authors in [69] utilize the effective dielectric method proposed by [70] and build a symmetric inverse permittivity matrix by choosing a proper interpolation method. But this inverse permittivity matrix can't be guaranteed to be positive definite, which means this algorithm might be unstable. It is proved in [26] that it is unstable for high dielectric contrast which means that the ratio between permittivities of different materials which are adjacent to each other is high. However, in the examined cases where the dielectric contrast is smaller than 10, this algorithm seems to be stable even in long-time simulations and shows the expected high accuracy though it is a first-order algorithm [69] for the tensor dielectric boundaries. Based on the interpolating method of [69], the authors in [71] improve the effective dielectric method by the use of perturbation theory from [72]. It remains to be a first-order algorithm, but with a better accuracy compared to the original variant.

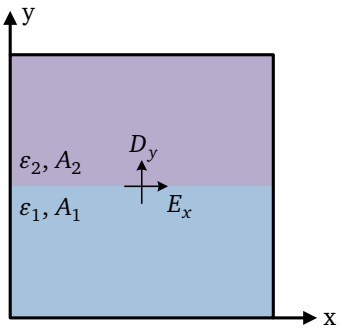

Figure 4.1: A two-dimensional cell filled with two isotropic materials with permittivities of ε_1 and ε_2, and with areas of A_1 and A_2

It is shown in [26] that a small alteration to the interpolating method of [69] can render the permittivity matrix symmetric and positive definite, therefore guarantee the stability of the algorithm.

In this section, discontinuities of the electric field strength and the electric flux density in tensor dielectric boundaries are investigated. An effective dielectric method is deduced by defining a pseudo-field [72] which is continuous at dielectric boundaries. Then, we apply the simplified FEM, which has been introduced in the previous chapter, to achieve the inverse permittivity matrix for a non-equidistant mesh. Furthermore, both the effective permittivity and the inverse permittivity matrix obtained here are proven to be symmetric and positive definite even for a non-equidistant mesh.

4.1.1 Effective Dielectric Method

In order to increase the numerical accuracy in achieving the inverse permittivity matrix $\mathbf{M}_{\varepsilon}^{-1}$, we apply an effective dielectric method in which the dielectric permittivity is averaged in each cell. The main idea of the applied effective dielectric method can be introduced by a simple case specified in Fig. 4.1.

As shown in this figure, a two-dimensional cell is divided on two isotropic materials with the different permittivities ε_1 and ε_2, and with the different areas A_1 and A_2. Our goal is to find the effective permittivity of this cell. It is known that the tangential component of the electric field strength and the normal component of electric flux density, which are respectively denoted as E_x and D_y in this case, are continuous across the interface of two materials. Thus, they can be approximated

to the respective field value on the center point: $E_x|_{r_0}$ and $D_y|_{r_0}$ by a first-order approximation using the Taylor expansion. Since the normal component of electric field E_y and the tangential component of electric flux density D_x are both discontinuous across the interface of the two materials, we can discuss the Taylor approximation of each discontinuous part. Take D_x for example: Both discontinuous parts can be related to the continuous field E_x by the expressions $\varepsilon_1 E_x$ and $\varepsilon_2 E_x$ respectively. Thus, they can be approximated to $\varepsilon_1 E_x|_{r_0}$ and $\varepsilon_2 E_x|_{r_0}$ based on the Taylor expansion of E_x. Applying area weighted average to them, the approximate value of D_x can be composed

$$D_x \approx \frac{(\varepsilon_1 A_1 + \varepsilon_2 A_2)}{A_1 + A_2} E_x|_{r_0}. \tag{4.1}$$

The similar deduction can be applied to E_y and it leads to

$$E_y \approx \frac{1}{A_1 + A_2} \left(\frac{A_1}{\varepsilon_1} + \frac{A_2}{\varepsilon_2} \right) D_y|_{r_0}. \tag{4.2}$$

It is in this way that the discontinuous field components D_x, E_y and the continuous field components E_x, D_y are related to each other by approximate coefficients. Hence the effective permittivity of this cell can be composed:

$$\bar{\boldsymbol{\varepsilon}} = \begin{bmatrix} \frac{(\varepsilon_1 A_1 + \varepsilon_2 A_2)}{A_1 + A_2} & 0 \\ 0 & \frac{\varepsilon_1 \varepsilon_2 (A_1 + A_2)}{A_1 \varepsilon_2 + A_2 \varepsilon_1} \end{bmatrix}. \tag{4.3}$$

It can be concluded from this case that the main idea for deducing effective inverse permittivity is describing the discontinuous field components by continuous field components since the discontinuous field components can't be approximated by Taylor expansion. This idea can be applied to the three-dimensional case shown in Fig. 3.2(a). By approximating D_x with the continuous filed component E_x in the region shown in Fig. 4.2, it is obvious to get the same result as already given in (3.19).

Actually, this idea can be extended to more general case, for example the grid cell shown in Fig. 4.3. It is assumed that each grid cell is small enough compared to the curvature of the structure and that at most two kinds of materials are presented in each cell. Thus, the interface can be approximated by planar surface with the normal vector $\hat{n}$ in each cell. Representing the interface with S_e, the tangential

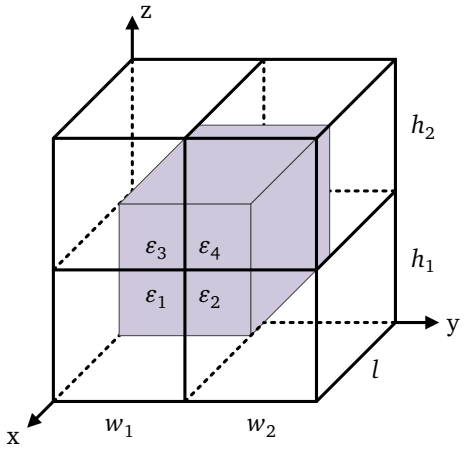

Figure 4.2: A 4-cell system showing the region where the approximation of D_x based on E_x is performed

component of the electric field strength and the normal component of electric flux density are continuous across the interface S_e according to

$$\hat{n} \times \vec{E}|_{S_e^+} = \hat{n} \times \vec{E}|_{S_e^-}, \tag{4.4}$$

$$\hat{n} \cdot \vec{D}|_{S_e^+} = \hat{n} \cdot \vec{D}|_{S_e^-}. \tag{4.5}$$

Additionally, we define $\hat{\tau}$ to be the unit vector parallel to $\hat{n} \times \vec{E}$ and $\hat{t}$ to be the direction both tangent to the surface and orthogonal to $\hat{\tau}$. It can be known that E_t and D_n are continuous while E_n, D_t and D_τ are discontinuous across the interface (It should be noticed that E_τ is zero).

According to [65] [72], we define a pseudo-field $\vec{F} = [D_n; E_t; 0]$ with

$$D_n = \hat{n} \cdot \vec{D},\ E_t = |\hat{n} \times \vec{E}| \tag{4.6}$$

in the $(\hat{n}, \hat{t}, \hat{\tau})$ coordinate system. This field can be transformed to the Cartesian coordinate system according to

$$\vec{F} = (\hat{n} \cdot \vec{D})\hat{n} + (\hat{n} \times \vec{E}) \times \hat{n} = (\hat{n} \otimes \hat{n})\vec{D} + (\mathbf{I} - \hat{n} \otimes \hat{n})\vec{E}, \tag{4.7}$$

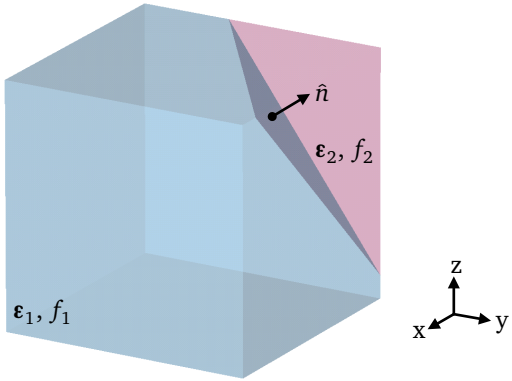

Figure 4.3: A grid cell filled with two anisotropic materials with permittivities of $\boldsymbol{\varepsilon}_1$ and $\boldsymbol{\varepsilon}_2$

where $\mathbf{I}$ represents the identity matrix. From this equation the electric field strength and the electric flux density can be written as [65]:

$$\vec{E} = \boldsymbol{\Gamma}\vec{F} = \left[(\hat{n}\otimes\hat{n})\boldsymbol{\varepsilon} + (\mathbf{I} - \hat{n}\otimes\hat{n})\right]^{-1}\vec{F}, \tag{4.8}$$

$$\vec{D} = \boldsymbol{\Pi}\vec{F} = \boldsymbol{\varepsilon}\left[(\hat{n}\otimes\hat{n})\boldsymbol{\varepsilon} + (\mathbf{I} - \hat{n}\otimes\hat{n})\right]^{-1}\vec{F}. \tag{4.9}$$

So far, the deduction is similar to that of [65]. After this step, the authors in [65] perform approximations in triplet subdomains and obtain an algorithm which has second-order convergence in frequency domain but suffers space instability in time domain. Yet in this dissertation, another approximation method is applied to assure space stability.

This approximation method is based on the idea that the discontinuous field, which has trouble in approximation by Taylor expansion, can be described by the continuous field. According to the Taylor expansion of $\vec{F}$: $\vec{F} = \vec{F}|_{r_0} + O(\Delta r)$, we approximate $\vec{F}$ with $\vec{F}|_{r_0}$. Therefore, in the two parts separated by the interface, both $\vec{E}$ and $\vec{D}$ can be approximated as functions of $\vec{F}|_{r_0}$. Performing the volume weighted average in the two parts leads to

$$\vec{E} \approx \left[f_1\boldsymbol{\Gamma}(\boldsymbol{\varepsilon}_1) + f_2\boldsymbol{\Gamma}(\boldsymbol{\varepsilon}_2)\right]\vec{F}|_{r_0} = \bar{\boldsymbol{\Gamma}}\vec{F}|_{r_0}, \tag{4.10}$$

$$\vec{D} \approx \left[f_1\boldsymbol{\Pi}(\boldsymbol{\varepsilon}_1) + f_2\boldsymbol{\Pi}(\boldsymbol{\varepsilon}_2)\right]\vec{F}|_{r_0} = \bar{\boldsymbol{\Pi}}\vec{F}|_{r_0}, \tag{4.11}$$

where $\boldsymbol{\varepsilon}_1$ and $\boldsymbol{\varepsilon}_2$ are the dielectric tensors of two materials coexisting in the examined cell, f_1 and f_2 are the ratios between the occupied volume of each material and the total volume. Based on the two equations, the effective permittivity $\bar{\boldsymbol{\varepsilon}}$ and the effective inverse permittivity $\bar{\boldsymbol{\xi}}$ can be both obtained as: $\bar{\boldsymbol{\Pi}}\bar{\boldsymbol{\Gamma}}^{-1}$ and $\bar{\boldsymbol{\Gamma}}\bar{\boldsymbol{\Pi}}^{-1}$.

Actually, the effective permittivity achieved here is identical to the one in [72]. It can be proven by transforming the effective permittivity from the global coordinate system to the coordinate system of $(\hat{n}, \hat{t}, \hat{\tau})$:

$$\begin{aligned}\mathbf{T}\bar{\boldsymbol{\varepsilon}}\mathbf{T}^T =& \mathbf{T}\left[f_1\boldsymbol{\varepsilon}_1\boldsymbol{\Gamma}(\boldsymbol{\varepsilon}_1)+f_2\boldsymbol{\varepsilon}_1\boldsymbol{\Gamma}(\boldsymbol{\varepsilon}_2)\right]\left[f_1\boldsymbol{\Gamma}(\boldsymbol{\varepsilon}_1)+f_2\boldsymbol{\Gamma}(\boldsymbol{\varepsilon}_2)\right]^{-1}\mathbf{T}^T \\ =& \left[f_1\boldsymbol{\varepsilon}_1'\boldsymbol{\Gamma}'(\boldsymbol{\varepsilon}_1')+f_2\boldsymbol{\varepsilon}_1'\boldsymbol{\Gamma}'(\boldsymbol{\varepsilon}_2')\right]\left[f_1\boldsymbol{\Gamma}'(\boldsymbol{\varepsilon}_1')+f_2\boldsymbol{\Gamma}'(\boldsymbol{\varepsilon}_2')\right]^{-1}. \end{aligned} \tag{4.12}$$

In this expression, $\mathbf{T}$ represents the transformation matrix mapping the Cartesian coordinate system to the coordinate system of $(\hat{n}, \hat{t}, \hat{\tau})$. The modified $\boldsymbol{\varepsilon}_1'$ and $\boldsymbol{\varepsilon}_2'$ are coordinate transformation of tensor $\boldsymbol{\varepsilon}_1$ and $\boldsymbol{\varepsilon}_1$, respectively. The function $\boldsymbol{\Gamma}'$ can be formulated as

$$\boldsymbol{\Gamma}(\boldsymbol{\varepsilon}) = \left[\mathbf{P}'\boldsymbol{\varepsilon} + (\mathbf{I}-\mathbf{P}')\right]^{-1}, \tag{4.13}$$

where

$$\mathbf{P}' = \begin{bmatrix} 1 & 0 & 0 \\ 0 & 0 & 0 \\ 0 & 0 & 0 \end{bmatrix}. \tag{4.14}$$

After expansion, expression (4.12) shows the same result as the effective permittivity of the coordinate system $(\hat{n}, \hat{t}, \hat{\tau})$ as achieved in [72].

4.1.2 Inverse Permittivity Matrix

It is shown in [32] how to deduce the inverse permittivity matrix for a staircase mesh filling from a FEM point of view. In the last chapter, we also succeed in obtaining the permittivity matrix with the help of the simplified FEM. Therefore, in this section, the simplified FEM is applied again to deduce the inverse permittivity matrix in combination with the effective dielectric method.

In contrast to [32] which applies the staircase material approximation for the primary grid, the effective dielectric method is applied for the dielectric approximation based on the dual grid. Thus, each dual cell is represented by an individual

dielectric material so that the inverse permittivity ξ can be expressed as Whitney volume elements on the dual grid:

$$\xi = \sum_j \bar{\xi}_j \widetilde{V}_j \widetilde{w}_{vj} = \sum_j \begin{bmatrix} (\bar{\xi}_{xx})_j \widetilde{V}_j \widetilde{w}_{vj} & (\bar{\xi}_{xy})_j \widetilde{V}_j \widetilde{w}_{vj} & (\bar{\xi}_{xz})_j \widetilde{V}_j \widetilde{w}_{vj} \\ (\bar{\xi}_{xy})_j \widetilde{V}_j \widetilde{w}_{vj} & (\bar{\xi}_{yy})_j \widetilde{V}_j \widetilde{w}_{vj} & (\bar{\xi}_{yz})_j \widetilde{V}_j \widetilde{w}_{vj} \\ (\bar{\xi}_{xz})_j \widetilde{V}_j \widetilde{w}_{vj} & (\bar{\xi}_{yz})_j \widetilde{V}_j \widetilde{w}_{vj} & (\bar{\xi}_{zz})_j \widetilde{V}_j \widetilde{w}_{vj} \end{bmatrix}, \tag{4.15}$$

where $\widetilde{V}_j$ is the volume of the dual grid cell filled with the effective inverse permittivity $\bar{\xi}_j$. The definition of $\vec{E}$ and $\vec{D}$ will follow those in expression (3.8), (3.9). By substituting them into $\vec{E} = \xi \vec{D}$ and applying the weighted residual method with testing function $\vec{w}_{ei}$, it results in

$$\sum_j e_j \int_V \vec{w}_{ei} \cdot \vec{w}_{ej} \mathrm{d}V = \sum_j d_j \int_V \xi \vec{w}_{ei} \cdot \vec{w}_{ej} \mathrm{d}V. \tag{4.16}$$

After a similar deduction, the inverse permittivity matrix can be revealed

$$\mathbf{M}_\xi = \mathbf{M}_e^{-1} \mathbf{T}_\xi \mathbf{M}_L. \tag{4.17}$$

Here, $\left(\mathbf{M}_L\right)_{ij} = \delta_{ij} \mathbf{L}(i) / \widetilde{\mathbf{A}}(i)$ (vector $\mathbf{L}$ and $\widetilde{\mathbf{A}}$ represent the lengths of edges in the primary grid G and the areas of facets in the dual grid $\widetilde{G}$, respectively), and $\mathbf{M}_e$, $\mathbf{T}_\xi$ are given by

$$\left(\mathbf{M}_e\right)_{ij} = \int_V \vec{w}_{ei} \cdot \vec{w}_{ej} \mathrm{d}V, \tag{4.18}$$

$$\left(\mathbf{T}_\xi\right)_{ij} = \int_V \xi \vec{w}_{ei} \cdot \vec{w}_{ej} \mathrm{d}V, \tag{4.19}$$

where trapezoidal integration is applied. It should be mentioned that a fundamental property of (4.17) is the continuity of tangential $\vec{D}$ since $\vec{D}$ is expanded as Whitney edge elements [32]. Indeed, this continuity can be guaranteed because each dual grid is approximated with one effective dielectric material.

According to this method, we can generate the constitutive relation for the electric field strength E_x in the 4-cell system of Fig. 4.4. All the relevant components of the electric flux density D are labelled in Fig. 4.4(a), and the effective inverse

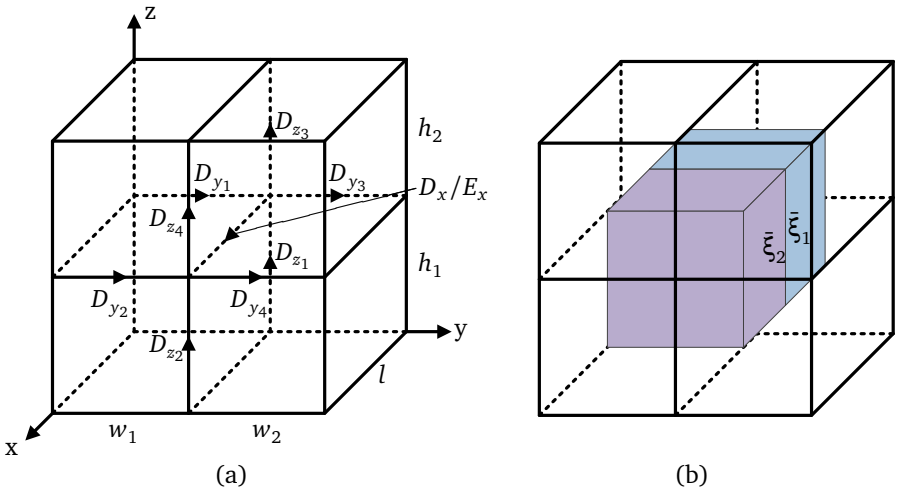

Figure 4.4: (a) Field components in a 4-cell system, (b) Material assignment in this 4-cell system: The two marked dual grid cells have effective inverse permittivity of $\bar{\xi}_1$ and $\bar{\xi}_2$

permittivity of the two dual grids involved are $\bar{\xi}_1$ and $\bar{\xi}_2$, respectively, as shown in Fig. 4.4(b). Thus, the constitutive relation can be given by

$$\begin{aligned} E_x = &\frac{1}{2}\frac{w_1}{w_1+w_2}(\bar{\xi}_{xy_1}D_{y_1}+\bar{\xi}_{xy_2}D_{y_2})+\frac{1}{2}\frac{w_2}{w_1+w_2}(\bar{\xi}_{xy_1}D_{y_3}+\bar{\xi}_{xy_2}D_{y_4}) \\ &+\frac{1}{2}\frac{h_1}{h_1+h_2}(\bar{\xi}_{xz_1}D_{z_1}+\bar{\xi}_{xz_2}D_{z_2})+\frac{1}{2}\frac{h_2}{h_1+h_2}(\bar{\xi}_{xz_1}D_{z_3}+\bar{\xi}_{xz_2}D_{z_4}) \\ &+\frac{\bar{\xi}_{xx_1}+\bar{\xi}_{xx_2}}{2}D_x. \end{aligned} \tag{4.20}$$

In this equation, the coefficient of D_x can be interpreted as the volume weighted average of $\bar{\xi}_{xx}$ in the region shown in Fig. 4.4(b). The coefficients of D_y can be explained in Fig. 4.5 which shows the XY cutting plane of Fig. 4.4: Firstly, interpolate D_{y_1} and D_{y_3}, D_{y_2} and D_{y_4}, respectively, to the two marked points. Secondly, multiply the interpolated values of the two points by the respective permittivity $\bar{\xi}_{xy_1}$ and $\bar{\xi}_{xy_2}$, then interpolate the multiplied values to the center of the edge labelled with E_x. It should be noticed that the interpolation method used in the first step isn't linear. It is the average of piecewise constant field (of which the value is D_{y_1},

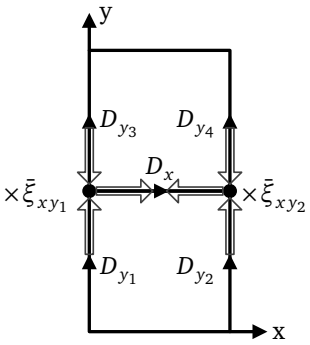

Figure 4.5: Construction of E_x from interpolating the components of D_y

D_{y_2}, D_{y_3} or D_{y_4} on the respective line segments) on the line segments from the center of the edges labelled with D_{y_1}, D_{y_2} to the center of the edges labelled with D_{y_3}, D_{y_4}, respectively. Actually, it is important to keep it in this way especially in non-equidistant mesh configurations because it is responsible for the symmetry of the inverse permittivity matrix.

This scheme of constructing the inverse permittivity matrix has the advantage that the inverse permittivity matrix can be guaranteed to be SPD. However, we find in the simulation that this scheme leads to a bad accuracy, which will be shown later in the test example. To increase the accuracy, an alternative scheme can be applied.

In this alternative scheme, each dual grid cell is divided into eight parts by the facets of its neighbouring primary grids, which is shown in Fig. 4.6(a). Each part of dual grid has 1/8 volume of its allocated primary gird and is assigned with a combined inverse permittivity $\hat{\boldsymbol{\xi}}$. In this combined inverse permittivity matrix, the off-diagonal elements come from the corresponding elements in the effective inverse permittivity of this dual grid. While the three diagonal elements $\hat{\xi}_{xx}$, $\hat{\xi}_{yy}$ and $\hat{\xi}_{zz}$, are taken from those in the effective inverse permittivity of the cells, which are centered at the edges of the neighbouring primary grids and marked as x^+, x^-, y^+, y^-, z^+ and z^- in Fig. 4.6(b)(c)(d). For example, the combined inverse permittivity of the part marked as $x^+y^+z^+$ in Fig. 4.6(a) can be formulated as

$$\hat{\boldsymbol{\xi}}_{x^+y^+z^+} = \begin{bmatrix} (\bar{\xi}_{xx})_{x^+} & (\bar{\xi}_{xy})_{\tilde{G}} & (\bar{\xi}_{xz})_{\tilde{G}} \\ (\bar{\xi}_{xy})_{\tilde{G}} & (\bar{\xi}_{yy})_{y^+} & (\bar{\xi}_{yz})_{\tilde{G}} \\ (\bar{\xi}_{xz})_{\tilde{G}} & (\bar{\xi}_{yz})_{\tilde{G}} & (\bar{\xi}_{zz})_{z^+} \end{bmatrix}, \tag{4.21}$$

where $(\bar{\xi}_{xx})_{x^+}$, $(\bar{\xi}_{yy})_{y^+}$, $(\bar{\xi}_{zz})_{z^+}$ are taken from the effective inverse permittivity of the cells marked as x^+, y^+ and z^+ in Fig. 4.6(b)(c)(d), and the other elements come from the effective inverse permittivity of the dual grid.

It will be proven in the next section that the effective inverse permittivity can be guaranteed to be SPD, as the sufficient condition of space stability for the former scheme. Yet in this scheme, the combined inverse permittivity of each 1/8 primary grid is constructed by the combination of the effective inverse permittivities from the neighbouring dual grid and edge-centered cells, so that we can't guarantee the SPD property of this combined tensor. Nevertheless, we can run a diagnostic program to check the SPD property of this combined inverse permittivity in each 1/8 primary grid and replace those, which are not SPD, with the effective inverse permittivities of the corresponding dual grids. Therefore, the finally chosen inverse permittivities in this scheme are the mixture of the combined inverse permittivities and the effective inverse permittivities and are guaranteed to be SPD.

From the FEM point of view, the spatial function of the inverse permittivity can be expressed as Whitney volume elements of 1/8 primary grid in this scheme. By the use of the simplified FEM, the inverse permittivity matrix $\mathbf{M}_{\xi}$ can be generated for this scheme. While applying this scheme for the 4-cell system of Fig. 4.4, we can obtain the same constitutive relation with equation (4.20) except the difference in the coefficient of D_x. Denoting the effective inverse permittivity of the cell centered at the location of E_x as $\bar{\xi}_3$, the coefficient of D_x is $\bar{\xi}_{xx_3}$ when all the combined inverse permittivities in the relevant 1/8 primary grids are SPD. In this occasion, this scheme is exactly the same compared to that presented in [71]. If there are some combined inverse permittivities which are not SPD, the coefficient of D_x represents the volume average of $\bar{\xi}_{xx_1}$, $\bar{\xi}_{xx_2}$ and $\bar{\xi}_{xx_3}$. Of course, when all the combined inverse permittivities involved are not SPD, the coefficient of D_x is $(\bar{\xi}_{xx_1} + \bar{\xi}_{xx_2})/2$, which is exactly the same as the one specified in equation (4.20).

In the following paragraphs, we will refer to the former scheme as "S_{eff}", this alternative scheme as "S_{com}" and discuss the space stability of them.

4.2 Space Stability

It is stated in chapter 2, that the space stability can be guaranteed if the material matrices $\mathbf{M}_{\xi}$ (or $\mathbf{M}_{\varepsilon}^{-1}$) and $\mathbf{M}_{\mu}^{-1}$ are both SPD. Because the tensor permeability of LC has much less influence than its tensor permittivity in high-frequency simulation, its tensor permeability is neglected and $\mathbf{M}_{\mu}^{-1}$ represents a diagonal matrix and can be proven to be SPD. Hence, we will focus on the discussion of whether $\mathbf{M}_{\xi}$ is SPD. It is proposed in [26] how to verify whether $\mathbf{M}_{\xi}$ is SPD using an equidistant mesh. In the current work we focus on a non-equidistant mesh and deduce the

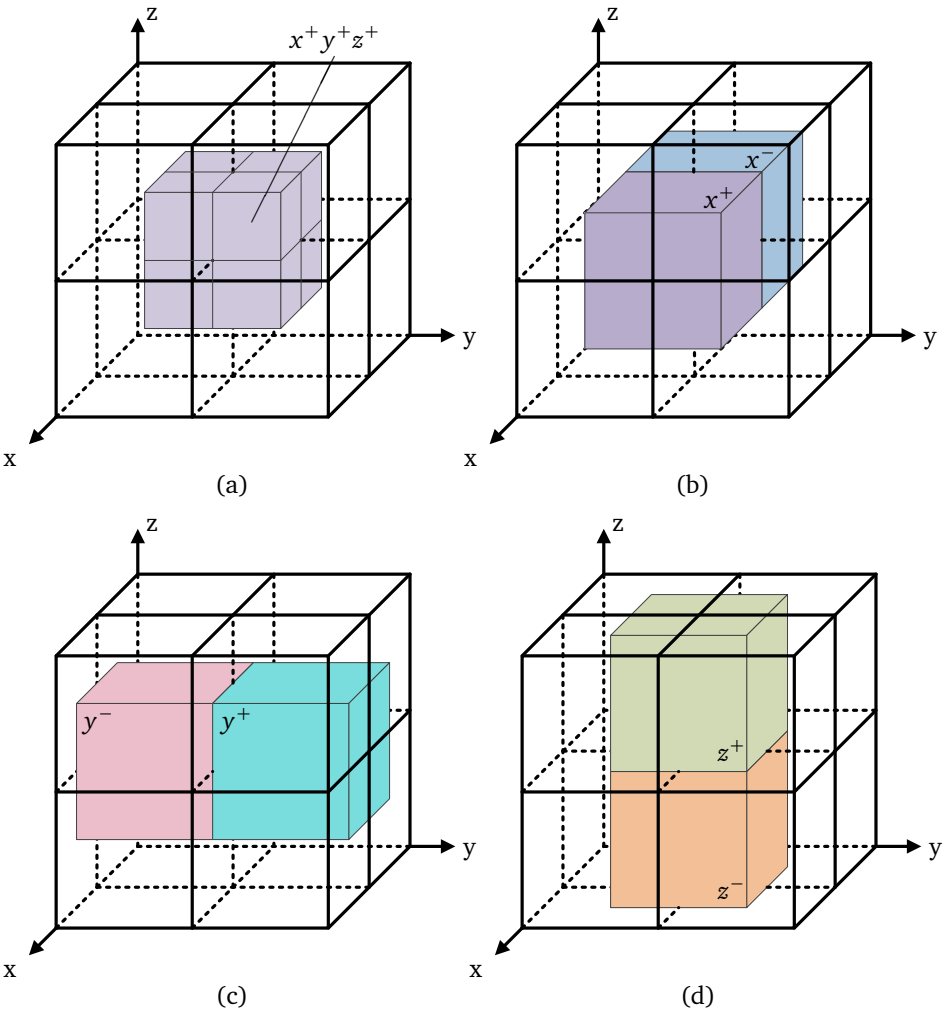

Figure 4.6: An 8-cell system. (a) 8 parts of the dual grid at the center. Each part is 1/8 volume of the allocated primary grid. (b) x^+ and x^- cells centered at the x-direction edges of primary grids. (c) y^+ and y^- cells centered at the y-direction edges of primary grids. (c) z^+ and z^- cells centered at the z-direction edges of primary grids.

SPD property of $\mathbf{M}_\xi$ matrix from the FEM point of view. Before the deduction, let's introduce several lemmas which will be used in the following deduction:

1. The matrix inverse of a positive definite matrix is also positive definite.
2. Let $\mathbf{P}$ be a nonsingular matrix, $\mathbf{A}$ is positive definite if and only if $\mathbf{P}^T\mathbf{A}\mathbf{P}$ is positive definite.
3. If $\mathbf{A}$ and $\mathbf{B}$ are positive definite, then so is $\mathbf{A}+\mathbf{B}$.

4.2.1 Symmetry and Positive Definiteness of the Effective Permittivity

For both the S_{eff} and S_{com} schemes, the SPD property of the effective inverse permittivity or the chosen inverse permittivity is the sufficient condition to the SPD property of the inverse permittivity matrix. However, in the S_{com} scheme, we check the SPD property of every combined inverse permittivity and replace the ones which are not SPD with the effective inverse permittivity. Thus, we just need to prove the SPD property of the effective inverse permittivity $\bar{\boldsymbol{\xi}}$:

According to lemma 1, the SPD property of the effective permittivity $\bar{\boldsymbol{\varepsilon}}$ will be deduced instead of effective inverse permittivity $\bar{\boldsymbol{\xi}}$. For simplicity, we transform $\bar{\boldsymbol{\varepsilon}}$ from Cartesian coordinate system to a local coordinate system using $(\hat{n},\hat{t},\hat{\tau})$ since $\bar{\boldsymbol{\varepsilon}}$ is SPD if $\mathbf{T}\bar{\boldsymbol{\varepsilon}}\mathbf{T}^T$ is SPD on the basis of lemma 2. The expression of $\mathbf{T}\bar{\boldsymbol{\varepsilon}}\mathbf{T}^T$ has already been obtained in equation (4.12). In order to get rid of the included inverse operation, we perform a transformation to $\mathbf{T}\bar{\boldsymbol{\varepsilon}}\mathbf{T}^T$ [26]:

$$\begin{aligned}
&\left[f_1\boldsymbol{\Gamma}'(\boldsymbol{\varepsilon}_1')+f_2\boldsymbol{\Gamma}'(\boldsymbol{\varepsilon}_2')\right]^T\left(\mathbf{T}\bar{\boldsymbol{\varepsilon}}\mathbf{T}^T\right)\left[f_1\boldsymbol{\Gamma}'(\boldsymbol{\varepsilon}_1')+f_2\boldsymbol{\Gamma}'(\boldsymbol{\varepsilon}_2')\right]\\
=&\left[f_1\boldsymbol{\Gamma}'(\boldsymbol{\varepsilon}_1')+f_2\boldsymbol{\Gamma}'(\boldsymbol{\varepsilon}_2')\right]^T\left[f_1\boldsymbol{\varepsilon}_1'\boldsymbol{\Gamma}'(\boldsymbol{\varepsilon}_1')+f_2\boldsymbol{\varepsilon}_1'\boldsymbol{\Gamma}'(\boldsymbol{\varepsilon}_2')\right]\\
=&f_1^2\boldsymbol{\Gamma}'(\boldsymbol{\varepsilon}_1')^T\boldsymbol{\varepsilon}_1'\boldsymbol{\Gamma}'(\boldsymbol{\varepsilon}_1')+f_2^2\boldsymbol{\Gamma}'(\boldsymbol{\varepsilon}_2')^T\boldsymbol{\varepsilon}_2'\boldsymbol{\Gamma}'(\boldsymbol{\varepsilon}_2')\\
&+f_1f_2\boldsymbol{\Gamma}'(\boldsymbol{\varepsilon}_1')^T\boldsymbol{\varepsilon}_2'\boldsymbol{\Gamma}'(\boldsymbol{\varepsilon}_2')+f_1f_2\boldsymbol{\Gamma}'(\boldsymbol{\varepsilon}_2')^T\boldsymbol{\varepsilon}_1'\boldsymbol{\Gamma}'(\boldsymbol{\varepsilon}_1').
\end{aligned}\tag{4.22}$$

It is obvious that the first and second terms are SPD. For the third and fourth terms, it is easy to deduce that

$$\begin{aligned}
&f_1f_2\boldsymbol{\Gamma}'(\boldsymbol{\varepsilon}_1')^T\boldsymbol{\varepsilon}_2'\boldsymbol{\Gamma}'(\boldsymbol{\varepsilon}_2')+f_1f_2\boldsymbol{\Gamma}'(\boldsymbol{\varepsilon}_2')^T\boldsymbol{\varepsilon}_1'\boldsymbol{\Gamma}'(\boldsymbol{\varepsilon}_1')\\
=&f_1f_2\boldsymbol{\Gamma}'(\boldsymbol{\varepsilon}_1')^T\boldsymbol{\varepsilon}_1'\boldsymbol{\Gamma}'(\boldsymbol{\varepsilon}_1')+f_1f_2\boldsymbol{\Gamma}'(\boldsymbol{\varepsilon}_2')^T\boldsymbol{\varepsilon}_2'\boldsymbol{\Gamma}'(\boldsymbol{\varepsilon}_2').
\end{aligned}\tag{4.23}$$

by expansion, so that they formulate also SPD matrices. As the sum of four SPD matrices, expression (4.22) is also SPD. On the basis of lemma 2, $\mathbf{T}\bar{\boldsymbol{\varepsilon}}\mathbf{T}^T$ can then

be guaranteed to be SPD, and both the effective permittivity $\bar{\boldsymbol{\varepsilon}}$ and the effective inverse permittivity $\bar{\boldsymbol{\xi}}$ also guarantee this property.

4.2.2 Symmetry and Positive Definiteness of the Inverse Permittivity Matrix

The construction of the inverse permittivity matrix $\mathbf{M}_\xi$ for both the S_{eff} and S_{com} schemes follows the same procedure except the difference in the Whitney expression of the inverse permittivity. Yet the spatial function of the inverse permittivity in the S_{eff} scheme can also be defined as Whitney volume elements of 1/8 primary grid. So these two schemes can share the same deduction to the SPD property of the inverse permittivity matrix $\mathbf{M}_\xi$.

In (4.17), it would be easy to deduce that $\left(\mathbf{M}_e\right)_{ij} = \delta_{ij}\widetilde{\mathbf{A}}(i)/\mathbf{L}(i)$ (where vector $\mathbf{L}$ and $\widetilde{\mathbf{A}}$ have the same definitions as those in $\mathbf{M}_L$). So the matrix $\mathbf{M}_e^{-1}$ is identical to $\mathbf{M}_L$ and they are both diagonal and nonsigular. Thus, the inverse permittivity matrix can be written as $\mathbf{M}_\xi = \mathbf{M}_L^T\mathbf{T}_\xi\mathbf{M}_L$. Thus, we will prove that $\mathbf{M}_\xi$ is SPD by showing $\mathbf{T}_\xi$ is SPD.

Assumed that $\mathbf{T}_\xi$ is a $N \times N$ matrix and $\mathbf{d}_{\text{FEM}}$ is a column vector with arbitrary variables d_1, d_2,..., d_N, it can be seen that

$$\mathbf{d}_{\text{FEM}}^T\mathbf{T}_\xi\mathbf{d}_{\text{FEM}} = \int_V \left(\xi\sum_i d_i\vec{w}_{ei}\right)\cdot\left(\sum_j d_j\vec{w}_{ej}\right)\mathrm{d}V, \tag{4.24}$$

where V stands for the whole computational domain. This expression can be further discretized to be the sum of the integration in each grid cell (denoted as Ω_1, Ω_2, ...)

$$\begin{aligned}\mathbf{d}_{\text{FEM}}^T\mathbf{T}_\xi\mathbf{d}_{\text{FEM}} = &\int_{\Omega_1}\left(\xi\sum_i d_i\vec{w}_{ei}\right)\cdot\left(\sum_j d_j\vec{w}_{ej}\right)\mathrm{d}\Omega_1 \\ &+\int_{\Omega_2}\left(\xi\sum_i d_i\vec{w}_{ei}\right)\cdot\left(\sum_j d_j\vec{w}_{ej}\right)\mathrm{d}\Omega_2 + ...\end{aligned} \tag{4.25}$$

Select the grid cell Ω_i for example, and denote the lengths of the edges and the relevant components of $\mathbf{d}_{\text{FEM}}$ according to Fig. 4.7. The trapezoidal integration is applied again so that the integration over each grid cell can be regarded as the average of the values in the eight vertices multiplied by the volume. Denoting ξ_p the effective inverse permittivity (in the S_{eff} scheme) or the chosen inverse permittivity

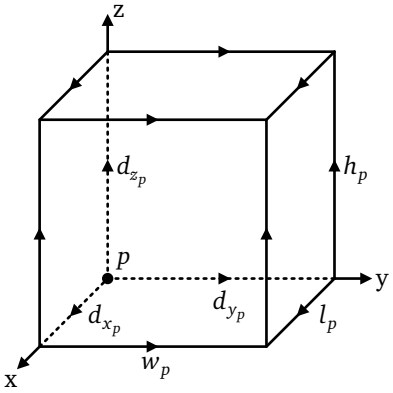

Figure 4.7: Schematic diagram of a grid cell allocated with point p and relevant d components

(in the S_{com} scheme) allocated at the vertex p, the value allocated at the vertex p shown in Fig. 4.7 can be derived as

$$\begin{aligned}
&\left[(\xi \sum_i d_i \vec{w}_{ei}) \cdot \sum_j d_j \vec{w}_{ej}\right]_p \\
&= \begin{bmatrix} d_{x_p} & d_{y_p} & d_{z_p} \end{bmatrix} \begin{bmatrix} 1/l_p & 0 & 0 \\ 0 & 1/w_p & 0 \\ 0 & 0 & 1/h_p \end{bmatrix} \xi_p \begin{bmatrix} 1/l_p & 0 & 0 \\ 0 & 1/w_p & 0 \\ 0 & 0 & 1/h_p \end{bmatrix} \begin{bmatrix} d_{x_p} \\ d_{y_p} \\ d_{z_p} \end{bmatrix} \\
&= \begin{bmatrix} d_{x_p} & d_{y_p} & d_{z_p} \end{bmatrix} \mathbf{A}_p \begin{bmatrix} d_{x_p} \\ d_{y_p} \\ d_{z_p} \end{bmatrix}. \qquad (4.26)
\end{aligned}$$

It has been deduced in the previous paragraphs that both the effective inverse permittivity in the S_{eff} scheme and the chosen inverse permittivity in the S_{com} scheme are SPD, which automatically leads to the SPD property of Matrix $\mathbf{A}_p$ in (4.26). Thus, we know that expression (4.26) is non-negative for arbitrary d_{x_p}, d_{y_p}, and d_{z_p}. Similarly, the values of other vertices in Fig. 4.7 can also be derived to be non-negative and so can the trapezoidal integration over Ω_i, which is the sum of them multiplied by one-eighth of volume. As the sum of the trapezoidal integration over Ω_1, Ω_2, ..., $\mathbf{d}_{FEM}^T \mathbf{T}_\xi \mathbf{d}_{FEM}$ is obvious to be non-negative for all $\mathbf{d}_{FEM}$ and the equality

can only hold when $\mathbf{d}_{\mathrm{FEM}}$ represents a zero vector. Therefore, it can be concluded that both $\mathbf{T}_\xi$ and $\mathbf{M}_\xi$ are SPD. Since $\mathbf{M}_\xi$ is SPD, the space stability of both schemes can be guaranteed.

4.3 Stable Update Scheme

4.3.1 Drawback of the Traditional Update Scheme

The traditional time integration approach applied to FIT or FDM performs a 2-step update scheme based on the electric and magnetic fields. When directly applied to tensor dielectric materials, it faces a problem that the tangential component of the electric field strength can't be guaranteed to vanish on the surface of PEC. In order to illustrate this phenomenon, a two-dimensional example in Fig. 4.8 is applied. If isotropic or diagonal-tensor dielectrics is present on the interface of PEC, the tangential components of the electric field strength and the electric flux density are both zero. According to Ampère's law in (2.2), it can be deduced that the conduction current density $\vec{J}_\kappa$ on the interface equals to $\nabla \times \vec{H}$. If mapping these relations to the discrete space, the tangential electric edge voltages $\widehat{\mathbf{e}}$ on the interface (which are marked by red arrows in Fig. 4.8) can be guaranteed to be zero by forcing the corresponding components in $\mathbf{M}_\varepsilon^{-1}$ in equation (2.40) to be zero. The integrated conduction current densities $\widehat{\widetilde{\mathbf{j}}}_\kappa$ on the interface (which are represented by red arrows in Fig. 4.8) can be determined by the discrete curl operation applied to the magnetic edge voltages $\widehat{\mathbf{h}}$.

The situation changes when full-tensor dielectric material is in the neighbouring of PEC. In this arrangement, the tangential components of the electric field strength is zero but the tangential components of the electric flux density may not be zero. The existing electric flux density means that the conduction current density $\vec{J}_\kappa$ on the interface is not equal to $\nabla \times \vec{H}$. In the corresponding discrete space, if the traditional update scheme is applied, there will be a situation that the integrated conduction current densities $\widehat{\widetilde{\mathbf{j}}}_\kappa$ on the interface are ignored. Actually, these components are responsible for the values of the normal electric edge voltages $\widehat{\mathbf{e}}$ next to the interface (which are marked by blue arrows in Fig. 4.8) and also contribute to the value of the tangential electric edge voltages $\widehat{\mathbf{e}}$ on the interface (which are denoted by red arrows in Fig. 4.8). This can be further clarified if we rewrite (2.41) with emphasis on the integrated current densities:

$$\widehat{\mathbf{e}}^{(m+3/2)} = \widehat{\mathbf{e}}^{(m+1/2)} + \Delta t \mathbf{M}_\varepsilon^{-1}(\widetilde{\mathbf{C}}\widehat{\mathbf{h}}^{(m+1)} - \widehat{\widetilde{\mathbf{j}}}_\kappa^{(m+1)} - \widehat{\widetilde{\mathbf{j}}}_i^{(m+1)}). \tag{4.27}$$

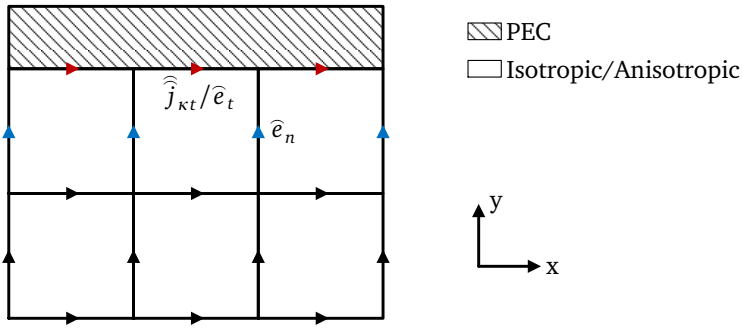

Figure 4.8: A two-dimensional example showing the interface between PEC and isotropic or anisotropic material

Take $\hat{e}_t$ and $\hat{e}_n$ in Fig. 4.8 for example, due to the anisotropic dielectric property, $\hat{e}_t$ and $\hat{e}_n$ are both related to the adjacent $\hat{\tilde{j}}_{\kappa t}$. Of course, $\hat{e}_t$ can be forced to zero by setting the corresponding components in $\mathbf{M}_\varepsilon$ to zero. But due to the unknown $\hat{\tilde{j}}_{\kappa t}$ on the interface, $\hat{e}_n$ is not available in the traditional update scheme. This is the reason, why the traditional update scheme fails in handling the interface between anisotropic materials and PEC.

4.3.2 Alternative Update Scheme

In order to cure this problem, a 3-step update scheme based on the magnetic field strength, the electric field strength and the electric flux density is applied instead [73]:

$$\hat{\mathbf{h}}^{(m+1)} = \hat{\mathbf{h}}^{(m)} - \Delta t \mathbf{M}_\mu^{-1} \mathbf{C} \hat{\mathbf{e}}^{(m+1/2)}, \tag{4.28}$$

$$\hat{\tilde{\mathbf{d}}}^{(m+3/2)} = \hat{\tilde{\mathbf{d}}}^{(m+1/2)} + \Delta t (\tilde{\mathbf{C}} \hat{\mathbf{h}}^{(m+1)} - \hat{\tilde{\mathbf{j}}}_i^{(m+1)}), \tag{4.29}$$

$$\hat{\mathbf{e}}^{(m+3/2)} = \mathbf{M}_\xi \hat{\tilde{\mathbf{d}}}^{(m+3/2)}. \tag{4.30}$$

After the time update of the magnetic edge voltages $\hat{\mathbf{h}}$ in the first equation, all electric facet fluxes $\hat{\tilde{\mathbf{d}}}$ can be calculated according to the second equation except the ones which are located on the interface between PEC and anisotropic dielectrics. They remain unknown due to the unknown $\hat{\tilde{\mathbf{j}}}_\kappa$ on this interface, but can be cal-

culated given that the electric edge voltages $\widehat{\mathbf{e}}$ on this interface are all zero. The complete procedure to obtain the electric facet fluxes $\widehat{\widehat{\mathbf{d}}}$ on this interface is shown below:

Assumed that $\mathbf{s}_i$ represents the index list which selects a subset of the components of $\widehat{\widehat{\mathbf{d}}}$ on the interface between PEC and the anisotropic dielectrics, and $\mathbf{s}_j$ represents the index list of the components not located on this interface, it can be deduced that

$$\widehat{\mathbf{e}}(\mathbf{s}_i) = \mathbf{M}_\xi(\mathbf{s}_i, \mathbf{s}_i)\widehat{\widehat{\mathbf{d}}}(\mathbf{s}_i) + \mathbf{M}_\xi(\mathbf{s}_i, \mathbf{s}_j)\widehat{\widehat{\mathbf{d}}}(\mathbf{s}_j). \tag{4.31}$$

Since $\widehat{\widehat{\mathbf{d}}}(\mathbf{s}_j)$ has already been calculated in the second step of the update scheme and $\widehat{\mathbf{e}}(\mathbf{s}_i)$ are known to be zero, $\widehat{\widehat{\mathbf{d}}}(\mathbf{s}_i)$, which denotes the electric flux densities on the PEC interface, can be obtained according to (4.31). Hence, all the components in $\widehat{\widehat{\mathbf{d}}}$ are known. Substituting $\widehat{\widehat{\mathbf{d}}}$ into the third equation, the electric edge voltages $\widehat{\mathbf{e}}$ can be calculated.

There is also a formulation which can maintain the traditional update scheme by applying a compensation to the inverse permittivity matrix $\mathbf{M}_\xi$. According to (4.31), the electric facet fluxes on the PEC interface can be expressed as a function of neighbouring components:

$$\widehat{\widehat{\mathbf{d}}}(\mathbf{s}_i) = -\mathbf{M}_\xi(\mathbf{s}_i, \mathbf{s}_i)^{-1}\mathbf{M}_\xi(\mathbf{s}_i, \mathbf{s}_j)\widehat{\widehat{\mathbf{d}}}(\mathbf{s}_j). \tag{4.32}$$

Similar to (4.31), the electric edge voltages $\widehat{\mathbf{e}}$ which are not located on the PEC interface can be determined by the relation

$$\widehat{\mathbf{e}}(\mathbf{s}_j) = \mathbf{M}_\xi(\mathbf{s}_j, \mathbf{s}_j)\widehat{\widehat{\mathbf{d}}}(\mathbf{s}_j) + \mathbf{M}_\xi(\mathbf{s}_j, \mathbf{s}_i)\widehat{\widehat{\mathbf{d}}}(\mathbf{s}_i). \tag{4.33}$$

Substituting (4.32) into this equation, the electric edge voltages which are not located on the surface of PEC can be achieved

$$\widehat{\mathbf{e}}(\mathbf{s}_j) = \left[\mathbf{M}_\xi(\mathbf{s}_j, \mathbf{s}_j) - \mathbf{M}_\xi(\mathbf{s}_j, \mathbf{s}_i)\mathbf{M}_\xi(\mathbf{s}_i, \mathbf{s}_i)^{-1}\mathbf{M}_\xi(\mathbf{s}_i, \mathbf{s}_j)\right]\widehat{\widehat{\mathbf{d}}}(\mathbf{s}_j), \tag{4.34}$$

and the ones on the surface of PEC are always equal to zero. Denoting $\mathbf{M}'_\xi$ to be the modified permittivity matrix with

$$\mathbf{M}'_\xi(\mathbf{s}_j, \mathbf{s}_j) = \mathbf{M}_\xi(\mathbf{s}_j, \mathbf{s}_j) - \mathbf{M}_\xi(\mathbf{s}_j, \mathbf{s}_i)\mathbf{M}_\xi(\mathbf{s}_i, \mathbf{s}_i)^{-1}\mathbf{M}_\xi(\mathbf{s}_i, \mathbf{s}_j), \tag{4.35}$$

and the remaining elements to be zero, the traditional update scheme can still be applied using $\mathbf{M}'_\xi$ instead of $\mathbf{M}_\xi$ in equation (2.41). Unfortunately, this formulation

involves the inversion of the non-diagonal matrix $\mathbf{M}_{\xi}(\mathbf{s}_i, \mathbf{s}_i)$. Consequently, it is inefficient if too many electric edge voltages are located on the surface of PEC.

4.4 Error Analysis

Unfortunately, it is difficult to determine the order of convergence for the S_{eff} and S_{com} schemes theoretically. Since the effective dielectric method is proven to be identical to the one presented in [72], we can refer to the conclusions made in [65] [71] [74]. The authors in [71] apply the effective dielectric method derived in [72] and the algorithm presented in [69] for constructing the inverse permittivity matrix. Therefore, it is the same as the S_{com} scheme when all the combined inverse permittivity in 1/8 primary grid are SPD. It is suggested by the simulation results in [71], that the algorithm demonstrates second-order accuracy. Whereas, the authors in [65] believe that the algorithm of [71] indeed has first-order convergence due to the error induced by the discretization. It is also pointed out by [74] that the algorithm of [71] is unstable for high dielectric contrast, which is not a problem for the S_{com} scheme. In the cost of degradation in the accuracy, the authors in [74] introduce a small modification and achieve a new stable algorithm, which is identical to the S_{eff} scheme. As stated in [74], both the algorithms in [71] and the improved stable variant of it in [74] are first-order algorithms.

Here, we perform the simulation based on a simple computational model with low dielectric contrast in order to verify the accuracy of the S_{eff} and S_{com} schemes. As shown in Fig. 4.9, the sphere in the center has a radius of 5 mm and is made of tensor dielectric material with the fixed relative permittivity

$$\boldsymbol{\varepsilon}_{\text{r}} = \begin{bmatrix} 2.49 & 0.35 & 0.3569 \\ 0.35 & 2.25 & 0.255 \\ 0.3569 & 0.255 & 2.26 \end{bmatrix}. \tag{4.36}$$

This sphere is included in a PEC box with the size of $20\times16\times12$ mm^3 and the remaining volume is filled with vacuum. We set up a discrete port besides the sphere and stimulate the resonator using a modulated Gaussian signal in the frequency range from 0 GHz to 20 GHz. Several probes are placed at random positions inside this box in order to monitor the electric field strength at every timestep. Then, we perform a high-frequency time-domain simulation based on FIT with a series of mesh ranging from $21\times17\times13$ to $101\times81\times61$ nodes.

For each simulation, we perform a discrete Fourier transform (DFT) to the time varying electric field components recorded at the probes and extract the eigenfrequencies from their frequency spectra. Since it is difficult to obtain the eigenfre-

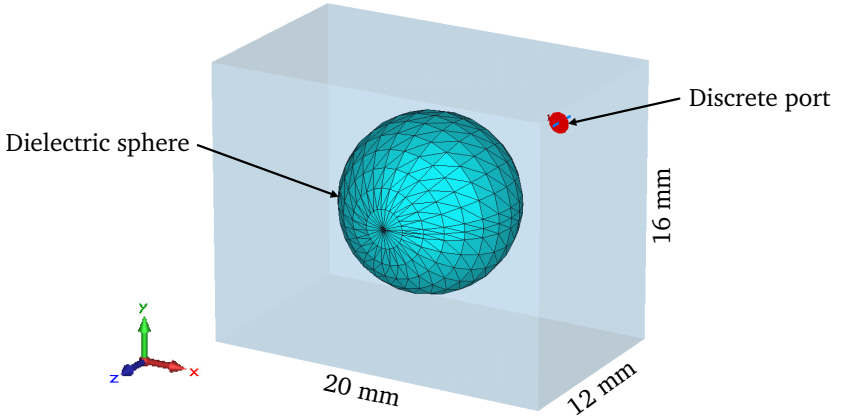

Figure 4.9: Schematic diagram of a tensor dielectric sphere in a PEC box

quencies for this setup in an analytical way, we carry out precise frequency-domain simulations in CST MICROWAVE STUDIO® and obtain the first three eigenfrequencies 10.0840 GHz (TE_{110} mode), 12.4654 GHz (TE_{101} mode) and 13.3985 GHz (TE_{011} mode) as a reference solution. Fig. 4.10 shows the relative error of the obtained eigenfrequencies compared to the reference frequencies, versus the cube root of the total number of grid nodes from 8.8 (referring to the mesh of 21×17×13 nodes) to 79.3 (referring to the mesh of 101×81×61 nodes).

It can be clearly seen from the results that the S_{com} scheme has a better accuracy than the S_{eff} scheme in this test example. It should be addressed that the convergence rate of TE_{110} mode is a little blurred due to the possible error in extracting the eigenfrequencies by the use of DFT. In this series of simulation, all the combined inverse permittivity of 1/8 primary grid are checked to be SPD in the S_{com} scheme. This agrees with the conclusion in [74] that the algorithm of [71] is usually stable in low dielectric contrast.

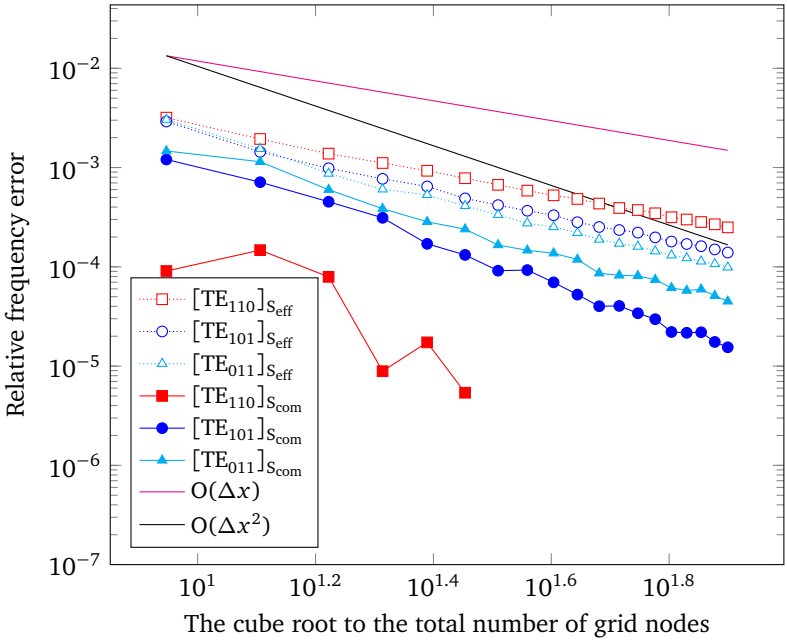

Figure 4.10: Relative error in several selected eigenfrequencies versus the cube root of the total number of grid nodes, where the subscript S_{eff} and S_{com} indicates the scheme used.

5 Applications

The previous chapters focus on the numerical modeling of LC director field orientation in static electric fields and the high-frequency electromagnetic wave propagation in LC media. With the consideration of the electric interaction energy, the orientations of LC molecules are obtained in combination of FIT and the vector method or the Q-tensor method. Given the obtained LC director field, FIT has been extended to be applied in the high-frequency simulation of LC media, which is characterized by tensor dielectric materials. A small modification has been adopted to the traditional leapfrog update scheme to deal with the interface between tensor dielectric materials and PEC.

Based on the schemes discussed, two typical tunable LC-based RF devices in form of a circular waveguide polariser and a rectangular waveguide phase shifter are examined in this chapter. The parameters of the circular waveguide polariser are provided by the Institute of Microwave Engineering and Photonics at Technische Universität Darmstadt. They also manufactured the research components and provided us with their measurement results. With the help of our newly developed simulation tools, the obtained results of this polariser are compared with measured data. In the simulation of the rectangular waveguide phase shifter, a complete simulation procedure is demonstrated, which includes static simulation of LC orientation and high-frequency simulation of LC material. The phase shift caused by the reorientation of LC can be determined by our simulation tools.

5.1 Introduction to the Simulation Tools

Our simulation tools are based on Matlab® and include a parameter definition module, a mesh generation module, the LC orientation simulation module and the time-domain simulation module. The complete workflow used to simulate tunable LC-based RF devices reads as follows:

- Import all the STL files of the components and define the material properties, mesh, boundary conditions, monitors, probes, etc., in the parameter definition module.
- Run the mesh generation module to set up the mesh information and matrices such as permittivity matrix, permeability matrix and discrete operators.

- Determine the LC director field in static electric field by the use of LC orientation simulation module and export them for further simulation.

- According to the obtained LC orientation, run the mesh generation module again to obtain the inverse permittivity matrix and related matrices which are necessary for time-domain simulation.

- Perform the time-domain simulation and record the electric field strength or the magnetic field strength for the probes or monitors. Afterwards, extract the eigenfrequencies or the S-parameters by postprocessing the time-domain simulation data.

5.2 Waveguide Polariser

Traditional ways to enable reconfigurable waveguides polarisation are based on mechanical steering. By physically changing the size of the waveguides, they allow the high-frequency field at a certain working frequency to propagate in one polarisation direction. For example, the circular waveguide polariser shown in [75] can adjust the polarisation of the incident wave by a rotary roller mechanism.

A new way has been proposed in [74] such that waveguide polarisation can now be achieved by electric or magnetic steering of LC. The LC can be modeled as anisotropic materials where their molecules can be oriented by electric or magnetic fields. For a circular waveguide filled with LC, the permittivity distribution can be controlled by electric or magnetic alignment of the LC molecules. Therefore, it leads to a controllable polarisation angle.

The prototype presented in [74] has applied magnetic biasing. A photo and the cutting plane view of this prototype are shown in Fig. 5.1 and 5.2. The circular waveguide section of this prototype has an inner radius of 1.4 mm and a length of 25 mm. It is filled with LC called GT3-23001 and are provided by the Merck company. The relative permittivity of the long axis $\varepsilon_{r,\parallel}$ and that of the perpendicular direction $\varepsilon_{r,\perp}$ are 3.16 and 2.47, respectively. Compared to other LC, it has lower dielectric losses at 30 GHz: $\tan\delta_{\parallel} = 0.0033$ and $\tan\delta_{\perp} = 0.0151$. As shown in Fig. 5.2, LC are contained in PTFE with a relative permittivity $\varepsilon_r = 3$ and dielectric losses characterized by $\tan\delta = 0.0011$.

It can be seen that there are three ring magnets placed around the waveguide. Each magnet has a thickness of 6 mm and the distances between two neighbouring magnets are both 3.5 mm. Those magnets excite magnetic fields from their north poles to their respective south poles so that the LC molecules in the waveguide section will be oriented. If the three magnets are placed with smoothly changed

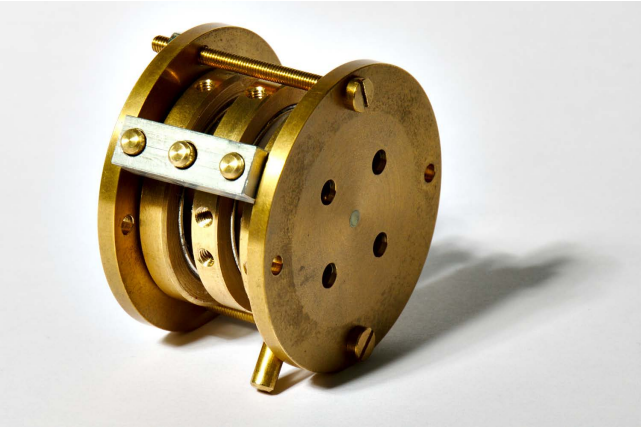

Figure 5.1: A photo of the waveguide polariser with magnetic biasing [76]*

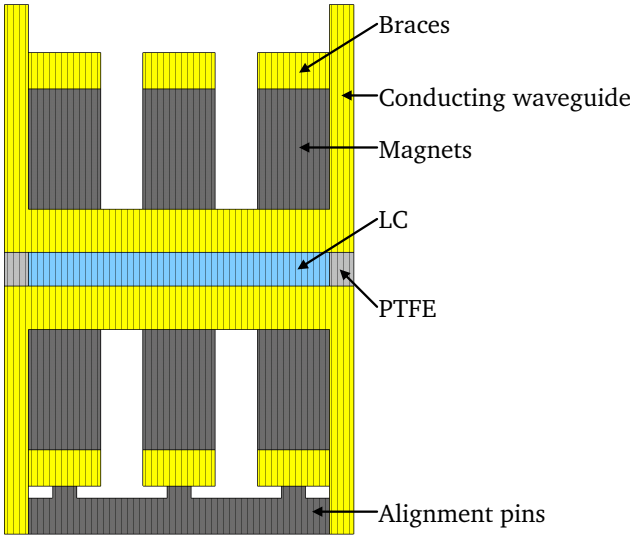

Figure 5.2: Cut view of the waveguide polariser based on magnetic biasing [76]*

* The photo and diagram are kindly provided by Sebastian Strunck from the Institute of Microwave Engineering and Photonics at Technische Universität Darmstadt

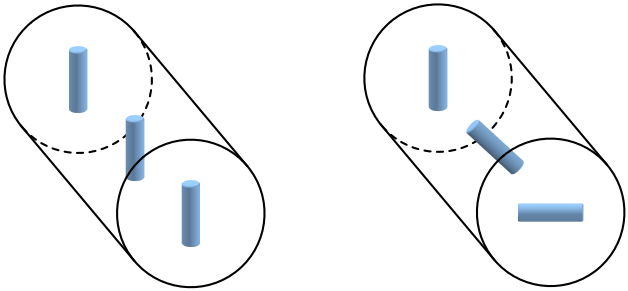

Figure 5.3: Schematic display of the molecular orientations in two polarisers with different rotation angles from input side in back to output side in front, (a) 0°, (b) 90°

rotation angles, the external magnetic field can align the LC molecules continuously from the front to end. If exciting a TE_{11} mode on one side of the waveguide with the electric field strength oriented in the same direction as the LC director field, the high-frequency field will be led along with the orientation of LC while passing the polariser. At the end of the polariser, the TE_{11} mode has been rotated according to the mechanical settings of the three magnets. Supposed that the rotation angle of the first magnet is 0° and the left two magnets are rotated by 0°, 0° or 45°, 90°, respectively. As shown in Fig. 5.3, the LC molecules will remain 0° or be continuously turned to 90° for these two pattens. Thus, polarisation angles of 0° and 90° are achieved, respectively. Of course, other polarisation angles are also available by rotating the magnets mechanically to the desired values.

5.2.1 Model Description

In order to simulate this waveguide polariser, a two-step procedure has been proposed. In the first step, the orientation of the LC molecules in the external magnetic field has to be determined. Since magnetic effects are not considered in our simulation tools, the orientation of LC molecules will be approximated according to the direction of the magnetic field. The commercial software CST EM STUDIO® is used here to calculate the magnetic field. Ignoring the magnetic susceptibility of LC, it can be modeled as vacuum, together with other materials in this waveguide polariser such as PTFE and conductors. Therefore, for the calculation of the magnetic field, the whole waveguide polariser can be simplified to the three magnets

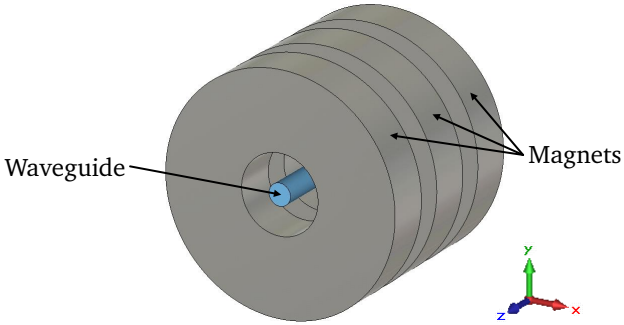

Figure 5.4: The simplified model of the waveguide polariser for the calculation of magnetic field

shown in Fig. 5.4. The specified circular waveguide section is modeled but not considered in the simulation. After a magnetostatic simulation run, the magnetic field strength can be exported from CST EM STUDIO®. By normalizing the vectors of the magnetic field, the approximated orientations of LC molecules can be extracted in the grid nodes of circular waveguide section. Then, we can achieve the dielectric tensor of the LC for each grid node.

The high-frequency simulation of the specified LC media can then be performed in our simulation tools. Because the required waveguide ports are not implemented in our codes, a substitute excitation method is applied. Inserting a proper discrete port inside the circular waveguide enables to excite the desired TE_{11} mode because the remaining modes are below the cutoff-frequency of the waveguide and will vanish after some distances. If applying this circular waveguide with convolutional perfectly matched layer (CPML) [77] on the one side, the electromagnetic field of the other side will be the required TE_{11} mode.

The generated TE_{11} mode will then pass through the circular waveguide section to simulate the polarisation process. In order to prevent the reflection of electromagnetic fields at the end of the circular waveguide, a CPML is added. Thus, we can obtain the simplified model for high-frequency simulation shown in Fig. 5.5. The magnets and alignment pins have no influence to high-frequency simulations and have been omitted. The conductor is simplified as PEC in the background.

As shown in Fig. 5.5, two monitors are placed on the two sides of the circular waveguide to monitor the electric field and magnetic field in time. For circular waveguides, the mode patterns can be easily calculated in an analytical way. However, we apply CST MICROWAVE STUDIO® to perform the 2D mode calculation

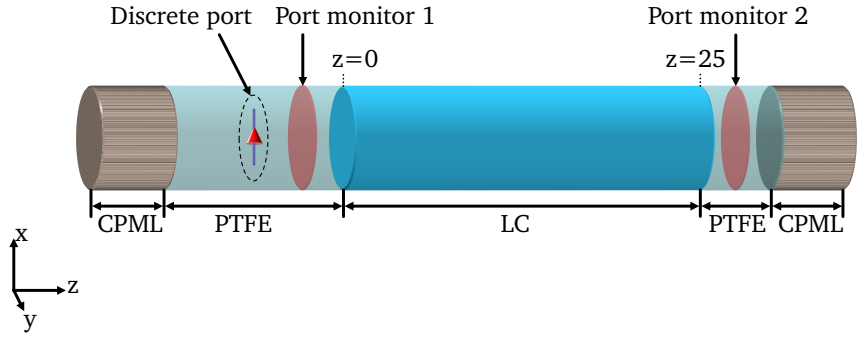

Figure 5.5: The simplified model of the waveguide polariser for high-frequency simulation of LC media

so that the mode patterns of more complex geometries can also be considered in the implemented evaluation process. As shown in Fig. 5.6, two orthonormal TE_{11} modes can be identified. Based on these two orthonormal modes, the input signals and output signals can be extracted from the monitored electric and magnetic fields [78]. The S-parameters can be obtained after DFT of these signals.

5.2.2 Simulation Results and Discussion

By performing the magnetostatic simulations in CST EM STUDIO®, the magnetic flux density on the 2D cutting planes which are placed at the beginning (z=0 mm according to the coordinate system defined in Fig. 5.5), the center (z=12.5 mm in Fig. 5.5) and the end (z=25 mm in Fig. 5.5) of the circular waveguide section are shown in Fig. 5.7 for both the 0°-polarisation and 90°-polarisation cases. It can be seen that for the 90°-polarisation case the magnetic flux density at the beginning and the end are not exactly oriented along the x axis or y axis, respectively. We think it is caused by the field coupling between the first magnet and the third magnet. The magnetic flux density of the 0°-polarisation case is nearly ideal though a small tilt towards the z axis can be observed.

The LC director field can be oriented approximately according to the magnetic flux density. Following equation (3.29), the spatial distribution of tensor permittivity in the LC region can also be deduced. Then, we excite the discrete port shown in Fig. 5.5 by a modulated Gaussian signal and perform the high-frequency time-domain simulation using a mesh of 61×61×181 nodes. Based on the mode

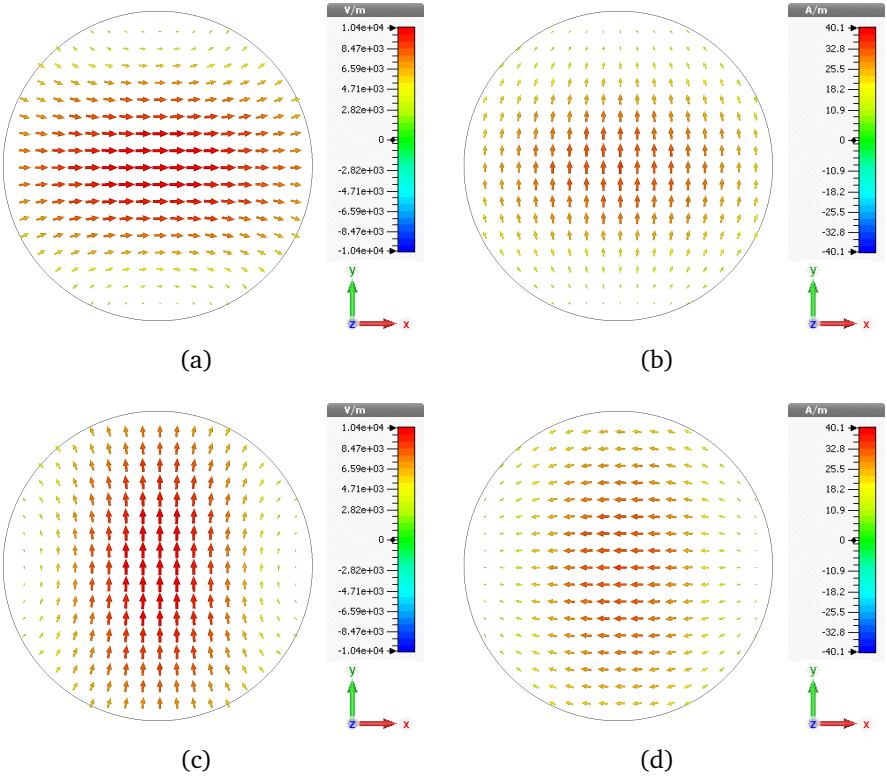

Figure 5.6: Two orthonormal TE_{11} modes of the circular waveguide, specified as mode 1 and mode 2, (a) electric field of mode 1, (b) tangential part of the magnetic field of mode 1 (c) electric field of mode 2, (d) tangential part of the magnetic field of mode 2

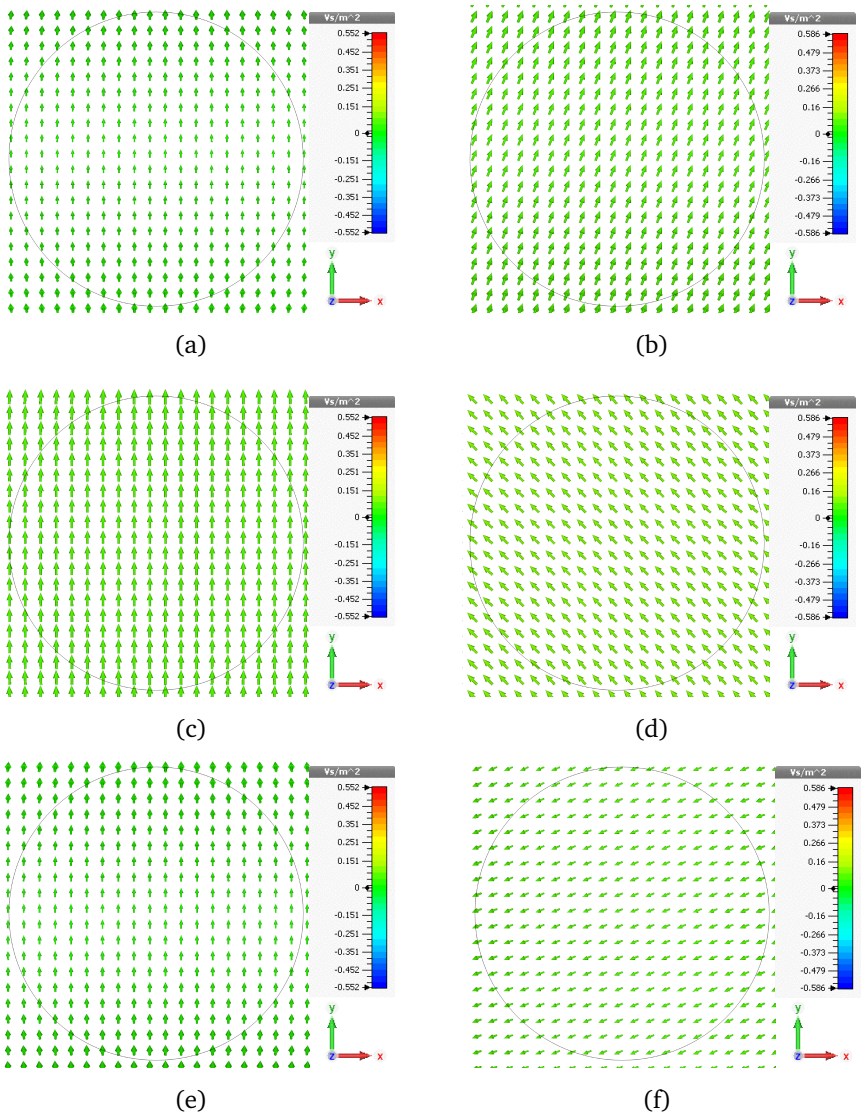

Figure 5.7: Magnetic flux density on XY cutting plane, (a) at z=0 mm for 0°-polarisation, (b) at z=0 mm for 90°-polarisation, (c) at z=12.5 mm for 0°-polarisation, (d) at z=12.5 mm for 90°-polarisation, (e)at z=25 mm for 0°-polarisation, (f) at z=25 mm for 90°-polarisation

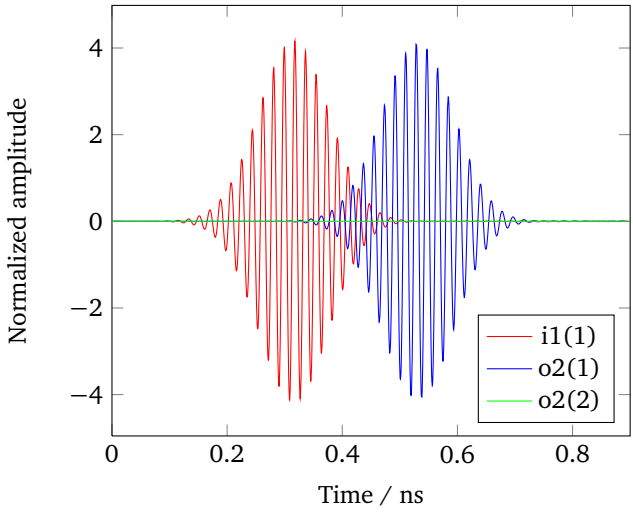

Figure 5.8: Time signals at two ports for the 0°-polarisation waveguide polariser

patterns calculated in CST MICROWAVE STUDIO®, the input signals and output signals of the two orthonormal TE_{11} modes can be extracted from the time varying electric field and magnetic field monitored at the positions shown in Fig. 5.5. These time signals are shown in Fig. 5.8 and 5.9 for the 0°-polarisation and 90°-polarisation cases. In these figures, i1(1) denotes the input signals of mode 1 at the monitor 1, and o2(1), o2(2) denotes the output signals of mode 1 and mode 2 at the monitor 2, respectively.

After performing a DFT of all the signals, the forward transmission coefficient denoted as S_{21} can be obtained for each mode in the 0°-polarisation and 90°-polarisation cases. In Fig. 5.10 and 5.11, $S_{2(1),1(1)}$ denotes the quotient between the frequency spectra of o2(1) and i1(1), and $S_{2(2),1(1)}$ is the quotient between the frequency spectra of o2(2) and i1(1). Since the dielectric and metallic RF losses are not considered in our simulation, we can see that $S_{2(1),1(1)}$ in the 0°-polarisation case and $S_{2(2),1(1)}$ in the 90°-polarisation case indicate good transmission for these two cases. In order to compare the simulation data to the measured results [74], we subtract 3.6 dB and 3.75 dB from S_{21} for the two cases, respectively, so that $S_{2(1),1(1)}$ in the 0°-polarisation case and $S_{2(2),1(1)}$ in the 90°-polarisation case are near to measured results as shown in Fig. 5.12 and 5.13. It can be seen that for the 90°-polarisation case, the trends of the simulated and measured $S_{2(1),1(1)}$ are similar. However, there are some oscillations in the measured result. We think they

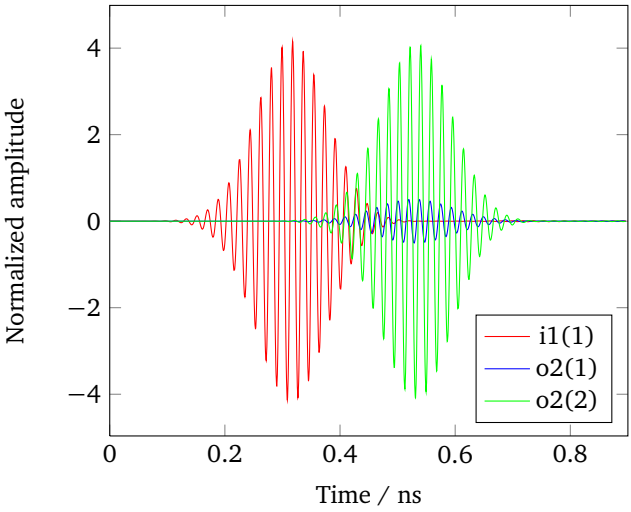

Figure 5.9: Time signals at two ports for the 90°-polarisation waveguide polariser

are caused by the gaps between components or port mismatching. Whereas, the simulated result of $S_{2(2),1(1)}$ is much smaller than the measured data for the 0°-polarisation case, which suggests a much better transmission in simulation. After discussions with the authors of [74], we believe that it might be caused by rotation errors of magnets while assembling the waveguides. It is impossible to place all the magnets with exact rotation angles as requested in the measurement. Additionally, the magnets might have ± 5° error in their rotational angle. Yet the 0°-polarisation case is very sensitive to this error, so that we see the large difference between the simulated and measured results. However, for the 90°-polarisation case, since the magnetic field is not ideal in aligning the molecules from 0° to 90°, it would be less sensitive to the error occurred to the rotational angles of magnets.

In order to verify our anticipation, an additional simulation is performed by placing the three magnets with rotational angles of 0°, 2.5°, 5°. After subtracting 3.4 dB from the simulated S_{21}, we compare the simulated results and measured results in Fig. 5.14. It can be seen that the trend of the simulated $S_{2(2),1(1)}$ shows a good agreement with that of the measured result.

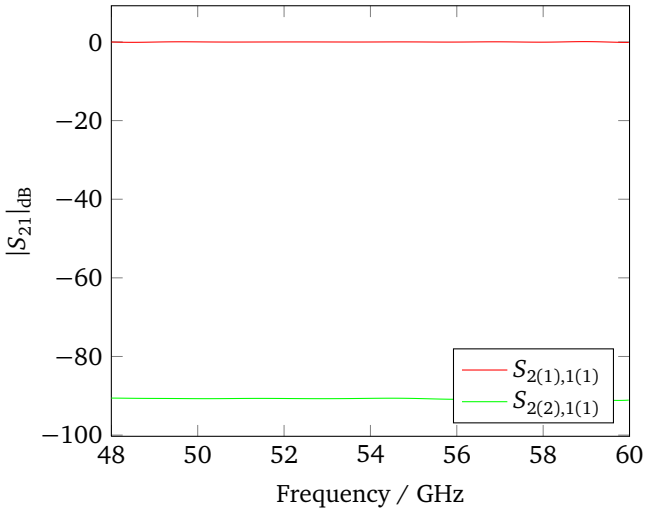

Figure 5.10: S-parameters of the 0°-polarisation waveguide polariser

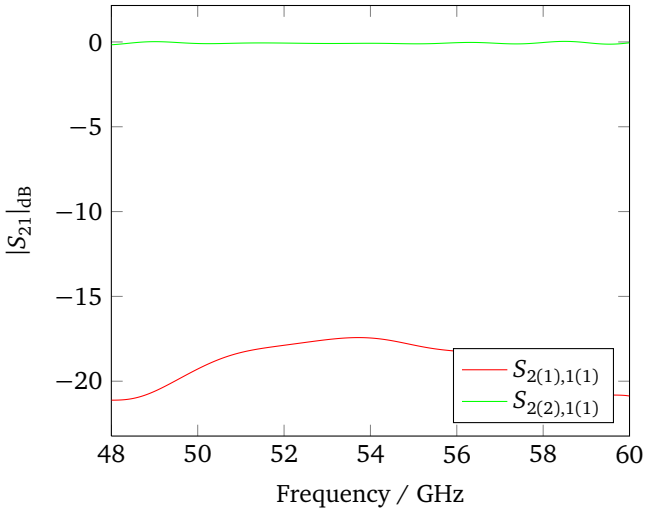

Figure 5.11: S-parameters of the 90°-polarisation waveguide polariser

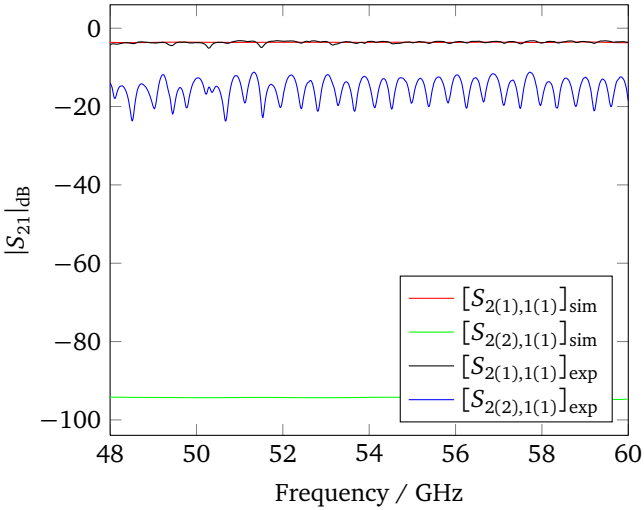

Figure 5.12: Comparison of simulated and measured S-parameters [74] for the 0°-polarisation waveguide polariser

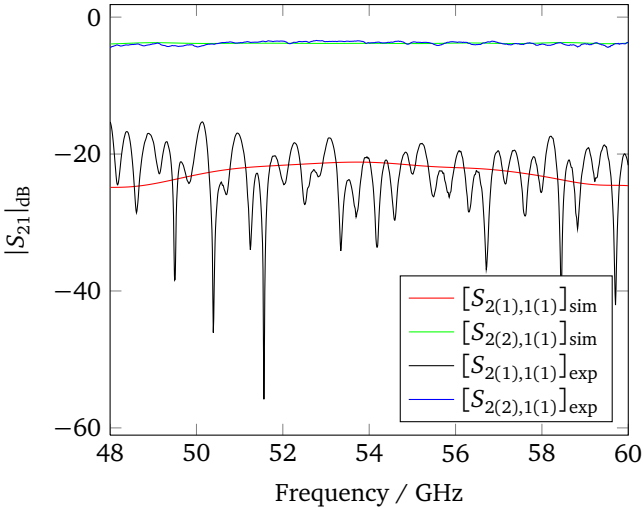

Figure 5.13: Comparison of simulated and measured S-parameters [74] for the 90°-polarisation waveguide polariser

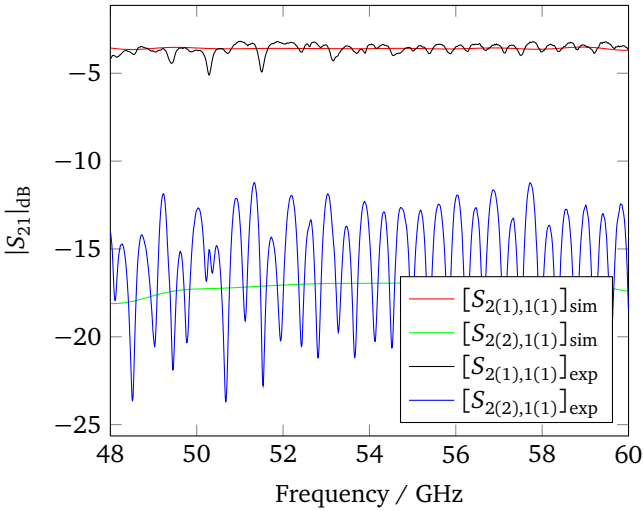

Figure 5.14: Comparison of simulated and measured S-parameters [74] for the 5°-polarisation waveguide polariser

5.3 Phase Shifter

Phase shifters are often used in phased-array antennas, especially for millimeter applications. For the commercial usage, cheaply integrated, compact devices with a sufficient figure-of-merit are required [10]. Currently used technologies of microelectromechanical systems (MEMS) and semiconductor devices have their respective limitations, especially for millimeter applications. A promising approach is explored in [8] [10] [12] [79] [80] which is given by the use of LC materials. Applying an external electric biasing, the LC can be reoriented so that the permittivity distribution is altered. This leads to a modified propagation constant and therefore to the phase shift. In this section, a rectangular waveguide phase shifter is taken as an example and a complete simulation run for static simulation of LC orientation and high-frequency simulation of LC material is performed.

5.3.1 Model Description

The simulation model of the rectangular waveguide phase shifter with the inner dimensions of 3.2×2.8 mm^2 is shown in Fig. 5.15. There is a dedicated segment

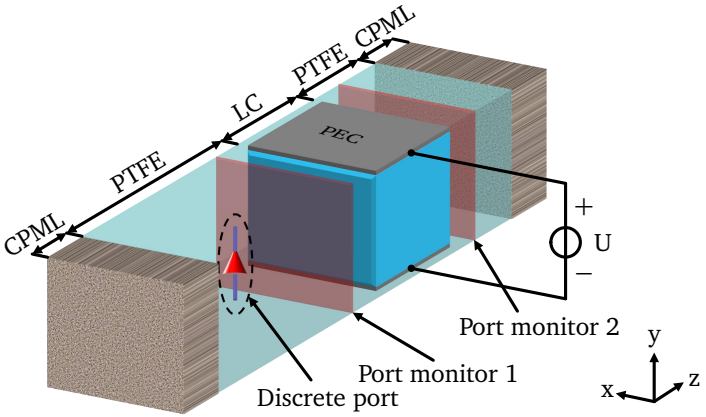

Figure 5.15: The simulated model of the waveguide phase shifter

with the length of 3 mm which is filled with LC named GT3-23001, while the rest of this waveguide phase shifter is filled with PTFE. There are two PEC electrodes inserted into the LC and the interfaces between the PEC electrodes and the LC are coated with homogeneous alignment layers. An external voltage source is applied to set up a static electric field.

The simulation of this waveguide phase shifter is carried out in two steps. We start with the static simulation to achieve the orientation of LC molecules with the voltage source switched on and off. The dielectric tensor of LC in each grid node can be obtained according to the spatial orientation of them. By stimulating a modulated Gaussian signal with frequency range from 32 GHz to 50 GHz, an excitation of TE_{10} mode can be assured. As shown in Fig. 5.15, there are two monitors placed on the two sides of LC segment, which record the electric field and magnetic field varying with time. The input signals and output signals on two monitors can be extracted based on the TE_{10} mode pattern in Fig. 5.16, which is calculated by CST MICROWAVE STUDIO®. Then, the phase shift can be obtained by the DFT of these signals.

5.3.2 Simulation Results and Discussion

By performing the calculations with our simulation tools, we plot the YZ cutting plane of the LC director field in Fig. 5.17. As shown in Fig. 5.17(a), when the voltage source is switched off, the orientation of LC is defined by the alignment

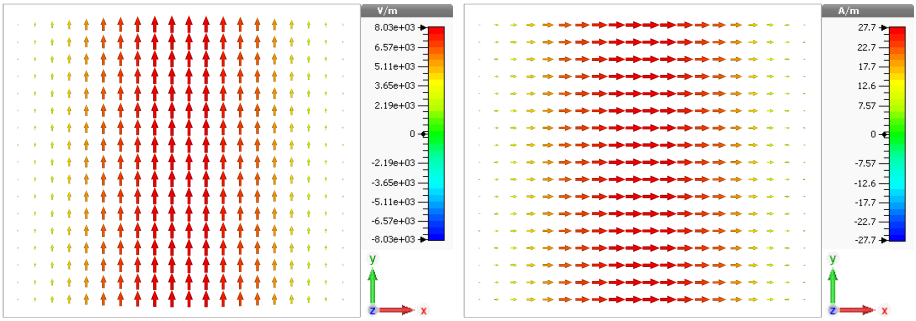

(a) (b)

Figure 5.16: TE_{10} mode of the rectangular waveguide, (a) electric field, (b) magnetic field

layers therefore all the molecules are aligned with z axis. In Fig. 5.17(b), when the upper electrode and lower electrode are applied with 10 V and -10 V, respectively, the molecules inside can be oriented while the molecules on the boundary are constrained by the alignment layers.

Then, high-frequency simulation of LC material is carried out in a mesh of 32×31×114 nodes, according to the determined director field. After postprocessing the recorded electric field and magnetic field on the two monitors, the input signals on the monitor 1 and the output signals on the monitor 2, which are denoted as i1 and o2, respectively, are displayed in Fig. 5.18 and 5.19 for the cases with voltage source switched on and off. Furthermore, we can obtain the forward transmission coefficient S_{21} by the DFT of these time signals. In Fig. 5.20, the phases of S_{21} in the cases with voltage source switched on and off are both plotted for the frequency range from 40 GHz to 50 GHz. It can be seen that phase shifts approximately from 32° to 37° can be obtained by the use of the external voltage source.

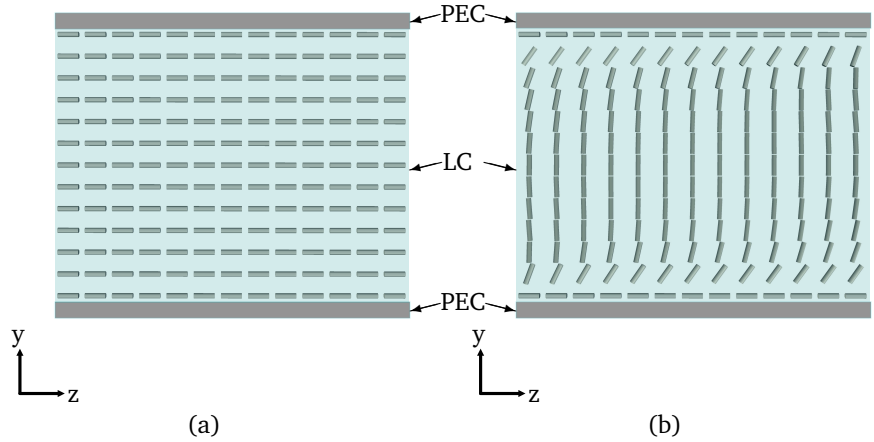

Figure 5.17: YZ cutting plane view of LC director field, (a) with voltage source switched off (b) with voltage source switched on

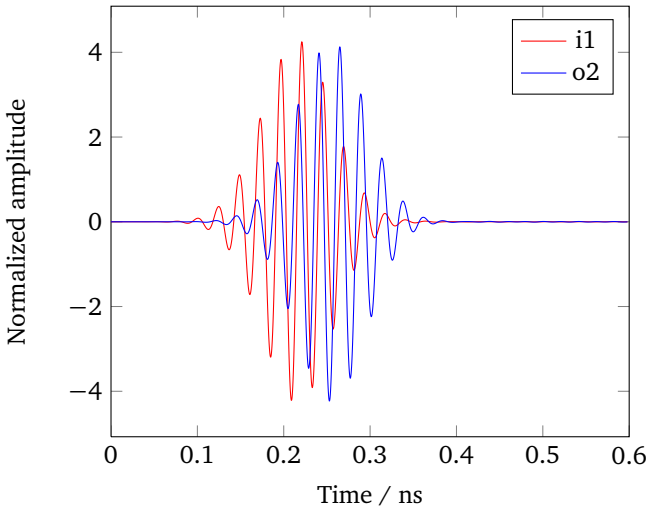

Figure 5.18: Time signals at two ports for the case with voltage source switched off

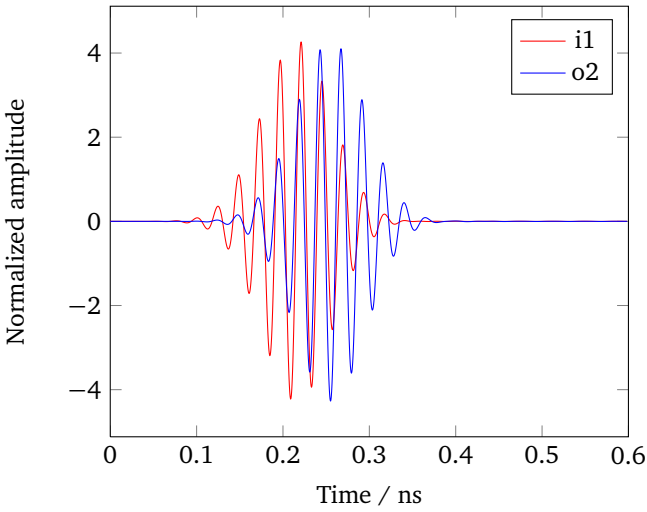

Figure 5.19: Time signals at two ports for the case with voltage source switched on

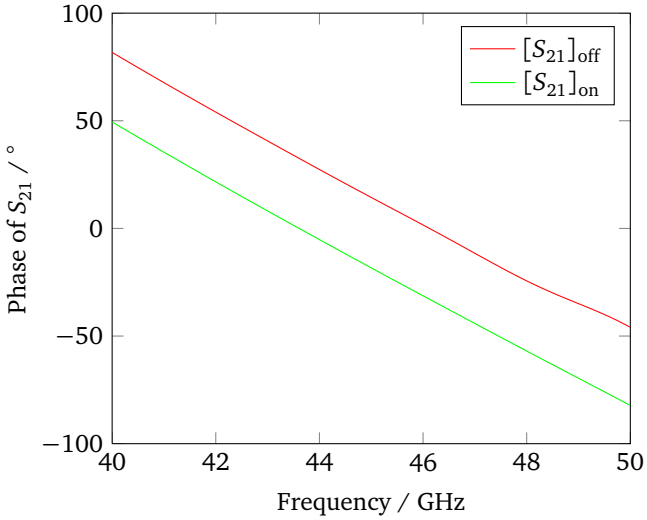

Figure 5.20: Phases of S_{21} for the cases with voltage source switched on and off. They are denoted as $[S_{21}]_{\text{on}}$ and $[S_{21}]_{\text{off}}$, respectively.

6 Summary and Outlook

In this dissertation, the numerical simulation of tunable LC-based RF devices is carried out by static simulation of LC orientation and high-frequency simulation of LC media. The vector method based on the Oseen-Frank theory, the Q-tensor method based on the Landau-de Gennes theory, and the extended FIT for solving electrostatic and time-domain problems of tensor dielectric materials are implemented and applied to realistic cases. The current chapter gives a brief summary of the essential points and offers an outlook for future works.

Finite Integration Technique

The finite integration technique is introduced in Chapter 2 as the basic theory for electrostatic and time-domain simulations which are involved in the numerical simulation of tunable LC-based RF devices. The necessity of space stability is discussed for time-domain simulation, which is symmetric and positive definite of inverse permittivity matrix for tensor dielectric material. Then, the traditional leap-frog update scheme is introduced as well as a generalized Courant-criterion.

Liquid-Crystal Orientation in Static Electric Fields

In order to achieve the LC director fields, the vector method and the Q-tensor method in combination with the electrostatic formulation of FIT are discussed in Chapter 3. The vector method applies the vector representation of the Oseen-Frank energy without thermotropic energy term, therefore it is a kind of constant order parameter method. While the Q-tensor method employs Q-tensor representation of the Landau-de Gennes energy with an additional thermotropic energy term, so that it belongs to variable order parameter method which can be used for the simulation of more general case, such as disclinations.

Both static and dynamic solvers are developed and implemented for these two methods. For the static solver, the direct and iterative methods are proposed. In the direct way, the minimization of the free energy with respect to the vector or Q tensor and the maximization of the free energy with respect to the potential are solved simultaneously. For the iterative way, two optimization problems are solved individually and a global iteration is performed. While for the dynamic solver, the dynamic equilibrium equation is achieved according to the dissipation principle.

On the basis of scientific publications, the spatial discretization is performed in the view of FEM. It is in this way that FIT is extended for solving electrostatic

problems of tensor dielectric material. Furthermore, based on the FEM disretization of the free energy, the derivatives and Hessian matrix are deduced according to the knowledge of matrix calculus.

Then, the vector method and the Q-tensor method are applied in the numerical simulation of a π-cell and a microstrip-like device. It is suggested by the simulation results that the Q-tensor method can be used in the simulation of the cases involved with disclinations or topological transitions between distinct states. The Q-tensor method demands a finer mesh and suffers larger computational cost than the vector method. Therefore, for the simulation of the cases without disclinations or topological transitions between distinct states, the vector method would be more appropriate.

Propagation of Electromagnetic Fields in Liquid-Crystal Materials

In Chapter 4, the oriented LC are thought to be continuously varying tensor dielectric materials and high-frequency simulation of these materials is developed based on FIT. By employing a pseudo-field on the dielectric boundary, the effective dielectric tensor is deduced for a cell which contains two kinds of tensor dielectric materials.

After the average of dielectric tensor per cell, the inverse permittivity matrix is constructed in the view of FEM for tensor dielectric materials. Then the space stability is established by proving the symmetric and positive definite property of the inverse permittivity matrix.

In order to guarantee vanishing tangential electric fields on the boundary between tensor dielectric material and PEC, a small modification is done to the traditional update scheme. It is also proposed a way to maintain the traditional update scheme by a compensation to the inverse permittivity matrix.

A three-dimensional test model is presented in a numerical simulation for error analysis of the effective dielectric method. The simulated results are given, which show the expected convergence rate.

Applications

In Chapter 5 the numerical simulation of a magnetic biasing circular waveguide polariser and a rectangular waveguide phase shifter has been presented. For the simulation of the polariser, a magnetostatic simulation is performed by the use of CST EM STUDIO® and the achieved magnetic field achieved is used to define the orientation of LC. Whereas in the simulation of phase shifter, the director field of LC is obtained by static simulation of LC orientation. Then, high-frequency simulation is implemented to determine the S-parameters for these two applications. In

particular, the simulated results of the polariser are compared with measurements and the comparisons show a good agreement.

Outlook

There are several ideas or remarks for future works with regard to the two parts of simulations.

For Liquid-Crystal Orientation in Static Electric Fields,

- Use a better approximation instead of staircase meshing
  In the current simulations, we apply a staircase approximation on regular hexahedron mesh which may not be accurate enough for complex structures. It is expected to explore a better approximation, which is similar to material approximation in FIT, or apply another kind of mesh, which have a better fitting with the structure.

- Apply adaptive meshing for the Q-tensor method
  It is indicated in the previous chapter that the Q-tensor method needs a fine mesh for correct results. But it would be a huge computational cost by defining the dense mesh in the complete computational domain. Therefore, it is required to apply adaptive meshing which can determine the motion of the disclinations accurately, even in a larger computational domain.

For Propagation of Electromagnetic Fields in Liquid-Crystal Materials

- Explore a true second-order algorithm for discontinuous tensor dielectrics
  Though the algorithm in this dissertation shows the expected accuracy in the numerical simulation of the test example, it is indeed a first-order algorithm for discontinuous tensor dielectrics. Moreover, this algorithm is used for the approximation of field discontinuities, but not singularities at the dielectric corners. Additionally, the interface between the PEC cell and the cell filled with tensor dielectric material is handled by a small modification in traditional update scheme, but it remains to be a problem how to handle the curved interface between tensor dielectric material and PEC. Thus, we expect a true second-order algorithm for discontinuous tensor dielectrics which could solve all these problems.

- Consider tensor permeability of LC materials
  Though the tensor permeability is not considered in this dissertation, we could anticipate the way to construct the inverse permeability matrix which can be guaranteed to be symmetric and positive definite. It would be similar to the construction of the inverse permittivity matrix, except that the

effective tensor permeability is obtained per primary grid instead of dual grid.

Acronyms and Symbols

General mathematical symbols

f	frequency	Hz
t	time	s
Δt	time step	s
$\vec{r}$	spatial vector	
O	Landau symbol for the order of the truncation error	
$\mathrm{d}\vec{s}$	element of edge	m
$\mathrm{d}\vec{A}$	element of area	m^2
$\mathrm{d}V$	element of volume	m^3
∂A	boundary of the area A	
∂V	boundary of the volume V	

Continuous Field Theory

$\vec{E}$	electric field strength	V/m
$\vec{H}$	magnetic field strength	A/m
$\vec{D}$	electric flux density	$\mathrm{C/m}^2$
$\vec{B}$	magnetic flux density	T
$\vec{J}$	total current density	$\mathrm{A/m}^2$
$\vec{J}_i$	imposed current density	$\mathrm{A/m}^2$
$\vec{J}_\kappa$	current density due to finite conductivity	$\mathrm{A/m}^2$
$\vec{J}_q$	current density due to moving charges	$\mathrm{A/m}^2$
$\varepsilon_\parallel$	permittivity parallel to the long axis	F/m
$\varepsilon_\perp$	permittivity perpendicular to the long axis	F/m
$\varepsilon_{\mathrm{r},\parallel}$	relative permittivity parallel to the long axis	
$\varepsilon_{\mathrm{r},\perp}$	relative permittivity perpendicular to the long axis	

ε, $\boldsymbol{\varepsilon}$	scalar and tensor permittivity	F/m
ε_r	relative permittivity	
μ, $\boldsymbol{\mu}$	scalar and tensor permeability	H/m
ρ	charge density	C/m^3
$\tan\delta$	dielectric loss of isotropic dielectrics	
$\tan\delta_\parallel$, $\tan\delta_\perp$	dielectric loss of anisotropic dielectrics	

Finite Integration Technique

G	primary grid	
$\widetilde{G}$	dual grid	
P	primary grid nodes	
L, $\mathbf{L}$	primary grid edges (elements and vector)	m
$\widetilde{L}$	dual grid edges	m
A	primary grid facets	m^2
$\widetilde{A}$, $\widetilde{\mathbf{A}}$	dual grid facets (elements and vector)	m^2
V	primary grid cells	m^3
$\widetilde{V}$	dual grid cell	m^3
$\widehat{e}$, $\widehat{\mathbf{e}}$	electric grid voltages (elements and vector)	V
$\widehat{h}$, $\widehat{\mathbf{h}}$	magnetic grid voltages (elements and vector)	A
$\widehat{\widehat{d}}$, $\widehat{\widehat{\mathbf{d}}}$	electric facet fluxes (elements and vector)	C
$\widehat{\widehat{b}}$, $\widehat{\widehat{\mathbf{b}}}$	magnetic facet fluxes (elements and vector)	Wb
$\widehat{\widehat{\mathbf{j}}}$	vector of grid currents	A
$\boldsymbol{\phi}$	vector of electrical scalar nodal potential	V
$\boldsymbol{\psi}$	vector of magnetic scalar nodal potential	A
$\mathbf{C}$, $\widetilde{\mathbf{C}}$	curl discrete operator on the primary/dual grid	
$\mathbf{S}$, $\widetilde{\mathbf{S}}$	divergence discrete operator on the primary/dual grid	
$\mathbf{G}$, $\widetilde{\mathbf{G}}$	gradient discrete operator on the primary/dual grid	
$\mathbf{M}_\varepsilon$	material matrix of permittivity	
$\mathbf{M}_\mu$	material matrix of permeability	
$\mathbf{M}_\kappa$	material matrix of conductivity	

γ_1	rotational viscosity	Pa·s
γ	viscosity	Pa·s
A, B, C	thermotropic parameters	J/m^3
α	linear coefficient in A	J/Km^3
K_{11}, K_{22}, K_{33}	Frank elastic constants associated with splay, twist and bend distortions	N
K_{24}	saddle-splay elastic constant	N
L_1, L_2, L_3	elastic parameters	N
q_0	chiral parameter	
S_0	uniaxial order parameter	
T	temperature	°C
T^*	supercooling temperature	°C
T_c	temperature where both the isotropic phase and nematic phase are stable	°C
T^+	temperature above which only the isotropic phase is stable	°C
E_{free}	free energy	J
E_{elastic}	elastic energy	J
E_{surface}	surface energy	J
E_{electric}	electric interaction energy	J
$E_{\text{thermotropic}}$	thermotropic energy	J
E_{sum}	summation of elastic, surface and thermotropic energy	J
D	energy dissipation	W
θ, φ, ψ	Euler angles	
λ, $\boldsymbol{\lambda}$	Lagrange multipliers (elements and vector)	
$\hat{a}$	long molecular axis	
$\vec{n}$	vector representation of LC molecules	
n_x, n_y, n_z	Cartesian components in $\vec{n}$	
$\mathbf{n}$	vector of nodal values of n_x, n_y and n_z	
$\hat{n}$	average direction of the long molecular axes	
$\hat{m}$	average direction of the molecular projections on the plane perpendicular to $\hat{n}$	
$\mathbf{Q}$	tensor representation of LC molecules	
q_i	coefficients of basis tensors	

$\mathbf{q}$	vector of nodal values of q_i	
χ	elements in vector $\vec{n}$ or tensor $\mathbf{Q}$	
$\lambda_1, \lambda_2, \lambda_3$	eigenvalues of tensor $\mathbf{Q}$	
S_1, S_2	orientational order parameters	
$\mathbf{T}_i$	basis tensors	
w_{pj}	Whitney nodal elements	1
$\vec{w}_{ei}, \vec{w}_{ej}$	Whitney edge elements	m^{-1}
w_{vj}	Whitney volume elements	m^{-3}
$\widetilde{w}_{vj}$	Whitney volume elements on the dual grid	m^{-3}
α_{rk}	coefficient of Butcher-scheme	
$\mathbf{I}$	identity matrix	
m	index of disclination	

Inverse Permittivity Matrix

$\vec{F}$	pseudo-field
$\hat{n}, \hat{t}, \hat{\tau}$	three axes of the coordinate systems defined by the material interface
$\mathbf{\Gamma}, \mathbf{\Pi}, \bar{\mathbf{\Gamma}}, \bar{\mathbf{\Pi}}$	tensor functions of permittivity
$\mathbf{M}_\xi$	material matrix of inverse permittivity
$\mathbf{T}$	transformation matrix

Acronyms

1D	one dimensional
DFT	discrete Fourier transform
FDM	finite difference method
FDTD	finite difference in time domain
FEM	finite element method
FIT	finite integration technique
FVM	finite volume method
LC	liquid crystal(s)
MEMS	microelectromechanical systems
MGE	Maxwell's grid equations

PBA	perfect boundary approximation
PEC	perfect electric conductor
RF	radio frequency
SDIRK	singly diagonally implicit Runge-Kutta method
SPD	symmetric and positive definite
STL	stereolithography

Bibliography

[1] P. G. de Gennes and J. Prost. *The Physics of Liquid Crystals*. International Series of Monographs on Physics. Clarendon Press, 1995.

[2] P. J. Collings. *Liquid Crystals: Nature's Delicate Phase of Matter*. Princeton University Press, 2002.

[3] G. Rai and D. Jain. Recent characterization and applicability of polymorphism: Liquid crystal. *International Journal of Pharmaceutical Sciences Review and Research*, 4(2):129–134, 2010.

[4] I. C. Khoo. *Liquid Crystals*. Wiley Series in Pure and Applied Optics. Wiley, 2007.

[5] P. J. Collings and M. Hird. *Introduction to Liquid Crystals: Chemistry and Physics*. Liquid Crystals Book Series. Taylor & Francis, 1997.

[6] S. T. Wu and D. K. Yang. *Fundamentals of Liquid Crystal Devices*. Wiley Series in Display Technology. Wiley, 2006.

[7] S. V. Pasechnik, V. G. Chigrinov, and D. V. Shmeliova. *Liquid Crystals: Viscous and Elastic Properties in Theory and Applications*. John Wiley & Sons, 2009.

[8] A. Gaebler, F. Goelden, S. Müller, and R. Jakoby. Multiphysics simulations for tunability efficiency evaluation of liquid crystal based RF devices. *Frequenz*, 62:240–245, October 2008.

[9] IMP. IMP web page, August 2013. http://www.imp.tu-darmstadt.de.

[10] S. Müller, P. Scheele, C. Weil, M. Wittek, C. Hock, and R. Jakoby. Tunable passive phase shifter for microwave applications using highly anisotropic liquid crystals. In *Microwave Symposium Digest, 2004 IEEE MTT-S International*, volume 2, pages 1153–1156 Vol.2, 2004.

[11] F. Goelden, A. Gaebler, S. Müller, A. Lapanik, W. Haase, and R. Jakoby. Liquid-crystal varactors with fast switching times for microwave applications. *Electronics Letters*, 44(7):480–481, 2008.

[12] F. Goelden, A. Gaebler, M. Goebel, A. Manabe, S. Müller, and R. Jakoby. Tunable liquid crystal phase shifter for microwave frequencies. *Electronics Letters*, 45(13):686–687, 2009.

[13] A. Gaebler, A. Moessinger, F. Goelden, A. Manabe, M. Goebel, R. Follmann, D. Koether, C. Modes, A. Kipka, M. Deckelmann, T. Rabe, B. Schulz, P. Kuchenbecker, A. Lapanik, S. Müller, W. Haase, and R. Jakoby. Liquid crystal-reconfigurable antenna concepts for space applications at microwave and millimeter waves. *International Journal of Antennas and Propagation*, 2009, March 2009.

[14] M. Hoefle, M. Koeberle, A. Penirschke, and R. Jakoby. Improved millimeter wave vivaldi antenna array element with high performance liquid crystals. In *2011 36th International Conference on Infrared, Millimeter and Terahertz Waves (IRMMW-THz)*, pages 1–2, 2011.

[15] O. H. Karabey, S. Bildik, S. Strunck, A. Gaebler, and R. Jakoby. Continuously polarisation reconfigurable antenna element by using liquid crystal based tunable coupled line. *Electronics Letters*, 48(3):141–143, 2012.

[16] C. M. Care and D. J. Cleaver. Computer simulation of liquid crystals. *Reports on Progress in Physics*, 68(11):2665, November 2005.

[17] M. R. Wilson. Molecular simulation of liquid crystals: progress towards a better understanding of bulk structure and the prediction of material properties. *Chemical Society reviews*, 36(12):1881–1888, December 2007.

[18] F. C. Frank. On the theory of liquid crystals. *Discussions of the Faraday Society*, 25(0):19–28, January 1958.

[19] H. Zocher. The effect of a magnetic field on the nematic state. *Transactions of the Faraday Society*, 29(140):945–957, January 1933.

[20] C. W. Oseen. The theory of liquid crystals. *Transactions of the Faraday Society*, 29(140):883–899, January 1933.

[21] R. James, E. Willman, A. Fernandez, and S. E. Day. Computer modeling of liquid crystal hydrodynamics. *IEEE Transactions on Magnetics*, 44(6):814–817, 2008.

[22] T. Weiland. A discretization model for the solution of Maxwell's equations for six-component fields. *Archiv Elektronik und Uebertragungstechnik*, 31:116–120, March 1977.

[23] T. Weiland. On the unique numerical solution of Maxwellian eigenvalue problems in three dimensions. *Particle Accelerators*, 17:227–242, 1985.

[24] T. Weiland. Lossy waveguides with arbitrary boundary contour and material distribution. *Archiv Elektronik und Uebertragungstechnik*, 33:170–174, April 1979.

[25] T. Weiland. Time domain electromagnetic field computation with finite difference methods. *International Journal of Numerical Modelling: Electronic Networks, Devices and Fields*, 9(4):295–319, 1996.

[26] G. R. Werner, C. A. Bauer, and J. R. Cary. A more accurate, stable, FDTD algorithm for electromagnetics in anisotropic dielectrics. *ArXiv e-prints*, 1212:4857, December 2012.

[27] I. A. Zagorodnov, R. Schuhmann, and T. Weiland. A uniformly stable conformal FDTD-method in Cartesian grids. *International Journal of Numerical Modelling: Electronic Networks, Devices and Fields*, 16(2):127–141, 2003.

[28] I. Zagorodnov, R. Schuhmann, and T. Weiland. Conformal FDTD-methods to avoid time step reduction with and without cell enlargement. *Journal of Computational Physics*, 225:1493–1507, August 2007.

[29] M. Panizo, A. Castellanos, and J. Rivas. Finite-difference operators in inhomogeneous anisotropic media. *Journal of Applied Physics*, 48:1054–1057, March 1977.

[30] F. J. Asencor and M. Panizo. Finite-difference operators in anisotropic inhomogeneous dielectrics: General case. *Journal of Computational Physics*, 95:387, August 1991.

[31] H. I. Saleheen and K. T. Ng. New finite difference formulations for general inhomogeneous anisotropic bioelectric problems. *IEEE Transactions on Biomedical Engineering*, 44(9):800–809, 1997.

[32] C. Kung and R. Lee. Alternative FDTD updating schemes for anisotropic materials. *IEEE Transactions on Antennas and Propagation*, 57:3903–3910, December 2009.

[33] R. Lee. A note on mass lumping in the finite element time domain method. *IEEE Transactions on Antennas and Propagation*, 54:760–762, February 2006.

[34] G. Kelly. *An Analytical and Numerical Investigation of Liquid Crystal Defects*. Ph.D. thesis, University of Strathclyde, 2006.

[35] R. James. *Modelling of High Resolution Liquid Crystal Devices*. Ph.D. thesis, University College London, October 2006.

[36] J. E. Anderson, P. Watson, and P. J. Bos. Shortcomings of the Q tensor method for modeling liquid crystal devices. *SID Symposium Digest of Technical Papers*, 30(1):198–201, 1999.

[37] K. Ito and K. Kunisch. *Lagrange Multiplier Approach to Variational Problems and Applications*. Advances in design and control. Society for Industrial and Applied Mathematics, 2008.

[38] C. Fox. *An Introduction to the Calculus of Variations*. Dover Books on Mathematics. Dover Publications, 1987.

[39] Wikipedia. Matrix calculus — Wikipedia, the free encyclopedia, August 2013. http://en.wikipedia.org/wiki/Matrix_calculus.

[40] A. R. Conn, N. I. M. Gould, and P. L. Toint. *Trust Region Methods*. MPS-SIAM Series on Optimization. Society for Industrial and Applied Mathematics, 2000.

[41] J. Nocedal and S. J. Wright. *Numerical Optimization*. Springer series in operations research and financial engineering. Springer, 2006.

[42] M. J. D. Powell. *A Fortran Subroutine for Solving Systems of Nonlinear Algebraic Equations*. Atomic Energy Res. Estab. Report ; AERE R 5947. H.M. Stationery Office, 1968.

[43] R. H. Byrd, J. C. Gilbert, and J. Nocedal. A trust region method based on interior point techniques for nonlinear programming. *Mathematical Programming*, 89(1):149–185, November 2000.

[44] R. A. Waltz, J. L. Morales, J. Nocedal, and D. Orban. An interior algorithm for nonlinear optimization that combines line search and trust region steps. *Mathematical Programming*, 107(3):391–408, July 2006.

[45] R. H. Byrd, M. E. Hribar, and J. Nocedal. An interior point algorithm for large-scale nonlinear programming. *SIAM Journal on Optimization*, 9(4):877–900, January 1999.

[46] N. Schopohl and T. J. Sluckin. Defect core structure in nematic liquid crystals. *Physical Review Letters*, 59(22):2582–2584, November 1987.

[47] N. Mottram and C. Newton. Introduction to Q-tensor theory. *University of Strathclyde, Department of Mathematics research report*, 2004:10, 2004.

[48] D. Miroshnychenko, N. A. Hill, N. J. Mottram, and J. E. Lydon. Evolution from a +2 defect to +1/2 defects in a cylindrical geometry. *Molecular Crystals and Liquid Crystals*, 437(1):251[1495]–267[1511], June 2005.

[49] A. Sonnet, A. Kilian, and S. Hess. Alignment tensor versus director: Description of defects in nematic liquid crystals. *Physical Review E*, 52(1):718–722, July 1995.

[50] H. Mori, E. C. Gartland, J. R. Kelly, and P. Bos. Multidimensional director modeling using the Q tensor representation in a liquid crystal cell and its application to the π cell with patterned electrodes. *Japanese Journal of Applied Physics*, 38:135, January 1999.

[51] R. James, E. Willman, F. A. Fernandez, and S. E. Day. Finite-element modeling of liquid-crystal hydrodynamics with a variable degree of order. *IEEE Transactions on Electron Devices*, 53(7):1575–1582, 2006.

[52] R. Barberi, F. Ciuchi, G. E. Durand, M. Iovane, D. Sikharulidze, A. M. Sonnet, and E. G. Virga. Electric field induced order reconstruction in a nematic cell. *The European Physical Journal E*, 13(1):61–71, 2004.

[53] T. F. Coleman and Y. Li. An interior trust region approach for nonlinear minimization subject to bounds. *SIAM Journal on Optimization*, 6(2):418–445, May 1996.

[54] T. F. Coleman and Y. Li. On the convergence of reflective newton methods for large-scale nonlinear minimization subject to bounds. *Mathematical Programming*, 67(2):189–224, 1994.

[55] E. Hairer and G. Wanner. *Solving Ordinary Differential Equations II: Stiff and Differential-Algebraic Problems*. Lecture Notes in Economic and Mathematical Systems. Springer, 1996.

[56] J. Yuan. *Numerical Simulation of Hysteresis Effects in Ferromagnetic Material with the Finite Integration Technique*. Cuvillier Verlag, 2005.

[57] J. E. Anderson, P. Watson, and P. J. Bos. Comparisons of the vector method and tensor method for simulating liquid crystal devices. *Liquid Crystals*, 28(1):109–115, 2001.

[58] G. D. Boyd, J. Cheng, and P. D. T. Ngo. Liquid-crystal orientational bistability and nematic storage effects. *Applied Physics Letters*, 36(7):556–558, April 1980.

[59] B. R. Ratna and R. Shashidhar. Dielectric studies on liquid crystals of strong positive dielectric anisotropy. *Molecular Crystals and Liquid Crystals*, 42(1):113–125, 1977.

[60] N. V. Madhusudana and R. Pratibha. Elasticity and orientational order in some cyanobiphenyls: Part IV. reanalysis of the data. *Molecular Crystals and Liquid Crystals*, 89(1-4):249–257, 1982.

[61] E. J. Willman. *Three Dimensional Finite Element Modelling of Liquid Crystal Electro-Hydrodynamics*. Ph.D. thesis, University College London, May 2009.

[62] J. P. Straley. Ordered phases of a liquid of biaxial particles. *Physical Review A*, 10(5):1881–1887, November 1974.

[63] D. Svenšek and S. Žumer. Instability modes of high-strength disclinations in nematics. *Phys. Rev. E*, 70:061707, Dec 2004.

[64] A. Stieb, G. Baur, and G. Meier. Alignment inversion walls in nematic liquid crystal layers deformed by an electric field. *Le Journal de Physique Colloques*, 36(C1):C1–185–C1–188, March 1975.

[65] C. A. Bauer, G. R. Werner, and J. R. Cary. A second-order 3D electromagnetics algorithm for curved interfaces between anisotropic dielectrics on a Yee mesh. *Journal of Computational Physics*, 230:2060–2075, March 2011.

[66] W. Müller, J. Krueger, A. Jacobus, R. Winz, T. Weiland, H. Euler, U. Hamm, and W. R. Novender. Numerical solution of 2- or 3-dimensional nonlinear field problems by means of the computer program PROFI. *Archiv für Elektrotechnik*, 65(4-5):299–307, July 1982.

[67] B. Krietenstein, P. Thoma, T. Weiland, and R. Schuhmann. The perfect boundary approximation technique facing the big challenge of high precision field computation, 1998.

[68] M. Clemens and T. Weiland. Discrete electromagnetism with the finite integration technique. *Journal of Electromagnetic Waves and Applications*, 15(1):79–80, 2001.

[69] G. R. Werner and J. R. Cary. A stable FDTD algorithm for non-diagonal, anisotropic dielectrics. *Journal of Computational Physics*, 226:1085–1101, September 2007.

[70] S. G. Johnson and J. D. Joannopoulos. Block-iterative frequency-domain methods for Maxwell's equations in a planewave basis. *Optics Express*, 8:173, January 2001.

[71] A. F. Oskooi, C. Kottke, and S. G. Johnson. Accurate finite-difference time-domain simulation of anisotropic media by subpixel smoothing. *Optics Letters*, 34:2778, September 2009.

[72] C. Kottke, A. Farjadpour, and S. G. Johnson. Perturbation theory for anisotropic dielectric interfaces, and application to subpixel smoothing of discretized numerical methods. *Physical Review E*, 77:36611, March 2008.

[73] A. P. Zhao, J. Juntunen, and A. V. Raisanen. An efficient FDTD algorithm for the analysis of microstrip patch antennas printed on a general anisotropic dielectric substrate. *IEEE Transactions on Microwave Theory and Techniques*, 47(7):1142–1146, 1999.

[74] S. Strunck, O. H. Karabey, A. Gaebler, and R. Jakoby. Reconfigurable waveguide polariser based on liquid crystal for continuous tuning of linear polarisation. *Electronics Letters*, 48(8):441–443, 2012.

[75] K. Sarabandi. A waveguide polarization controller. *IEEE Transactions on Microwave Theory and Techniques*, 42(11):2171–2174, 1994.

[76] D. Davies. A twist in the tail. *Electronics Letters*, 48(8):415, 2012.

[77] A. Taflove and S. C. Hagness. *Computational Electrodynamics: The Finite-Difference Time-Domain Method*. The Artech House antenna and propagation library. Artech House, Incorporated, 2005.

[78] J. D. Jackson. *Classical Electrodynamics, 3rd ed*. Wiley India Pvt. Limited, January 2007.

[79] S. Müller, A. Penirschke, C. Damm, P. Scheele, M. Wittek, C. Weil, and R. Jakoby. Broad-band microwave characterization of liquid crystals using a temperature-controlled coaxial transmission line. *Microwave Theory and Techniques, IEEE Transactions on*, 53(6):1937–1945, 2005.

[80] Y. Garbovskiy, V. Zagorodnii, P. Krivosik, J. Lovejoy, R. E. Camley, Z. Celinski, A. Glushchenko, J. Dziaduszek, and R. Dabrowski. Liquid crystal phase shifters at millimeter wave frequencies. *Journal of Applied Physics*, 111(5):054504–054504, 2012.

Acknowledgements

At this point of completing this dissertation, I would like to express my gratitude to all the people, who directly or indirectly helped me throughout the whole time of this Ph.D. work.

Firstly, I would like to thank Prof. Dr.-Ing. Thomas Weiland for the scientific supervision and giving me this great opportunity to work in his group TEMF and Graduate School of Computational Engineering.

I would also like to thank Prof. Dr.-Ing. Rolf Jakoby for kindly contributing in the reviewing of this dissertation as co-referee.

Special thanks to Dr.-Ing. Wolfgang Ackermann for his scientific guidance and for his carefully reviewing and correcting this dissertation until the last version. His patience and diligent work spirit impressed me and inspires me into the future career.

Other special thanks to M. Sc. Sebastian Strunck at the Institute of Microwave Engineering and Photonics of TU Darmstadt for generously providing the parameters and measured results of the circular waveguide polariser.

During the research activities at TEMF and Graduate School of Computational Engineering, my present and former colleagues provided the pleasant and friendly atmosphere. I thank them for that.

Additionally, I would like to thank my former Master degree supervisor Prof. Min Zhang, who guided me into the present research region. I have learned a lot from him, not only the careful and diligent work attitude.

Last but not least, I want to express my deep thanks to my parents for their supporting throughout all of my life. Especially thank my wife Mrs. Lina Wang for her continual support and encouragement.

Thanks to all of you!

Curriculum Vitae

Xiao Wang
born on 06th July 1986 in Rongcheng city, Shandong province, China

1991–1996	Lanjia primary school in Rongcheng city, Shandong province
1996–2000	Rongcheng no.39 junior middle school in Rongcheng city, Shandong province
2000–2003	Rongcheng no.1 senior middle school in Rongcheng city, Shandong province
2003–2007	Bachelor degree study at Department of Electronics and Information Engineering of Tongji University in Shanghai city
2007–2010	Master degree study at Department of Electronics and Information Engineering of Tongji University in Shanghai city
2010–2013	PhD student at Department of Electrical Engineering and Information Technology of Darmstadt University of Technology in Darmstadt